



UNIVERSITÀ  
DI PAVIA

PHD IN BIOMEDICAL SCIENCES

DEPARTMENT OF BRAIN AND BEHAVIORAL SCIENCES

UNIT OF NEUROPHYSIOLOGY

**Investigating brain structure and function with  
advanced MRI in health and disease**

PhD Tutor: Claudia Gandini

PhD dissertation of  
Nicolò Rolandi

**a.a. 2021/2022**

---

---



---

# Introduction

Temporal lobe epilepsy (TLE) is the most common form of drug-resistant focal epilepsy, characterized by seizures that originate in the temporal lobe. There are several causes that can lead to temporal lobe epilepsy, including damage to the brain as a result of trauma or infection, or as a consequence of developmental abnormalities. Surgery is an excellent treatment option for drug-resistant epilepsy with focal symptoms; in fact, it has been shown that two-thirds of operated TLE patients get rid of seizures permanently. Currently, the scientific community agrees that the balance between seizure control and the extent of any cognitive deficits following temporal lobectomy in TLE patients, is of fundamental importance in determining the criteria for the operation itself. Therefore, it becomes essential to devise and develop methodologies of investigation in the preoperative phase, which allow to obtain the most predictions of the surgical outcome as close as possible to the actual outcome of the operation. Having available such information would allow to propose a priori a planning of the rehabilitation path, so as to offer the patient an overview of the path to follow, helping him considerably in his pre and postoperative practice.

The principal aim of this work was to use MRI to investigate brain microstructure and macrostructural connectivity in health and pathology. Tractography allows the three-dimensional reconstruction of axonal fiber bundles through the use of new and innovative mathematical algorithms, while multi-compartmental diffusion techniques use the modelling of diffusion in various brain tissues to allow a characterization at the microstructural level by evaluating, for example, the density and dispersion of axon orientation.

This thesis has three main contributions. It starts with a clinical study of white matter alterations in TLE, highlighting the importance of taking in account features as epileptogenic zone side and its aetiology; then evaluate and quantify the variability that arises from different protocols for bundle segmentation; finally, an application of tractography in a clinical study for a deeper investigation of the white matter microstructural alteration.

---

In detail, in Chap. 1 and 2 will be provided basics information to understand, respectively, MRI functioning and TLE pathology. In Chap. 3 will be describe the application of MRI to study of TLE. This part of this work was selected for an oral presentation at the ISMRM 29th Annual Meeting & Exhibition 2020 and a paper is in preparation. In Chap. 4, after a brief insight into tractography, will be presented a work born from a multicenter collaboration and our personal contribution. The work is pubblicated on Neuroimage (Schilling et al. 2021). In Chap. 5 will be describe the application of tractography reconstruction to characterize specific white matter bundle. This work was selected for an oral presentation at the ISMRM 30th Annual Meeting & Exhibition 2021, at the moment we are improving the numerosity of dataset and a paper is in preparation. Finally in Chap. 6 will be presented final conclusion.

---

# Index

Introduction	1
Chapter 1 Magnetic Resonance Imaging	7
1.1 Interaction of nuclear Magnetization with Magnetic Field	8
1.2 Relaxation and Signal Detection	9
1.3 Magnetic Field Gradient and Image Reconstruction	10
1.4 Pulse Sequences	11
1.4.1 Spin Echoes pulse sequence	11
1.4.2 SE Inversion Recovery sequence	12
1.4.3 Gradient Echoes pulse sequence	12
1.4.4 Fast Scanning Techniques and Eco Planar Imaging	13
1.5 Image Contrast	14
1.6 MRI TECHNIQUES	15
1.6.1 Structural T1-weighted MRI	15
1.6.2 Diffusion MRI	16
Chapter 2 Temporal Lobe Epilepsy: 3TLE multicentre study	19
2.1 Epilepsy	19
2.1.1 Pathophysiology	19
2.1.2 Epileptic seizure	20
2.1.3 Diagnosis	21
2.1.4 Classification	21
2.1.5 Epidemiology	22
2.1.6 Neuroimaging in Epilepsy	23
2.2 3TLE project	23
2.2.1 Background and motivation	23

---

2.2.3 Aim	24
Chapter 3 White matter microstructure characterisation in Temporal Lobe Epilepsy	26
3.1 Background and motivation	27
3.2 Protocol Design	29
3.2.1 Subjects	29
3.2.2 MRI acquisition	31
3.2.3 MRI processing	31
3.3 Study I: Pre-surgery whole-brain analysis	32
3.3.1 Tract-based spatial statistic (TBSS)	32
3.3.2 Results	33
3.4 Study II: Histological group analysis	38
3.4.1 Temporal lobe analysis - methods	38
3.4.2 Results	39
3.6 Discussion	41
3.6.1 Study I: Pre-surgery whole-brain analysis	41
3.6.2 Study II: Histological group analysis	44
3.6.3 Limitation	45
3.7 Conclusion	46
Chapter 4 Tractography dissection of the human brain: challenges and perspectives	47
4.1 Tractography	47
4.1.1 Diffusion tensor based tractography	47
4.1.2 Constrain Spherical Deconvolution based tractography	48
4.2 Tractography dissection variability	49
4.3 Methods	50
4.3.1 Data	50

---

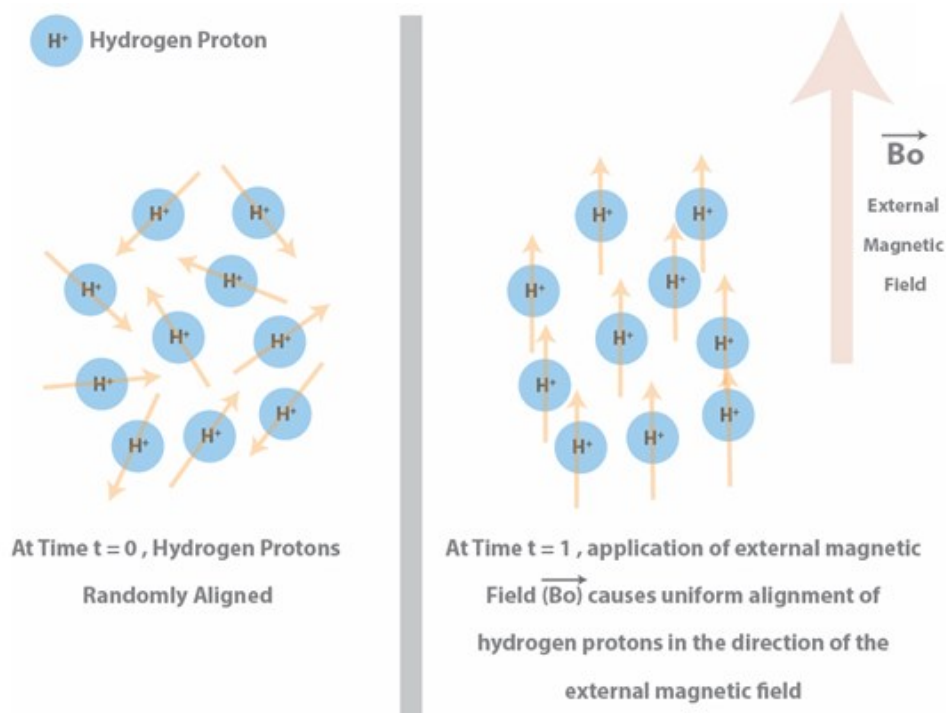
4.3.2 Pathway-specific analysis	51
4.3.3 Bundle dissection variability across protocols	52
4.4 Tract segmentation - my contribution	53
4.5 Results	60
4.5.1 Qualitative results	61
4.5.2 Pathway-specific results	62
4.5.3 Inter-protocol variability	64
4.5.4 Variability within and across pathways	66
4.6 Discussion	67
4.7 Conclusion	70
Chapter 5 Impact of cerebro-cerebellar and long association fibers in TLE	71
5.1 Background and motivation	71
5.2 Protocol	73
5.2.1 Subjects	73
5.2.2 MRI acquisition	73
5.2.3 MRI processing	73
5.2.4 Whole-brain tractography and TDI maps	74
5.2.5 Tract extraction and characterization	74
5.3 Results	76
5.4 Discussion	77
Chapter 6 Conclusion	79
Appendices	80
References	88

---

# Chapter 1

## Magnetic Resonance Imaging

Magnetic resonance imaging (MRI) is an imaging technique used primarily in medical settings to produce high quality images of the human body. The physical principles of MRI are the same of the nuclear magnetic resonance (NMR). Moreover MRI allows for the spatial localization of the NMR signal, hence producing an image. In the standard clinical practice, MRI investigations use *hydrogen nuclei* ( ${}^1\text{H}$ ) as probes both because of their high natural abundance in the human body and because their intrinsic nuclear properties. Indeed, the human body is primarily constituted by fat and water, which makes the body composed approximately 63% by hydrogen atoms. For these reasons MRI primarily images the NMR signal from the hydrogen nuclei. Each voxel of an image of the human body contains one or more tissues. Zooming in a voxel reveals that water molecules compose cells. Each water molecule has one oxygen atom and two hydrogen atoms. The hydrogen nucleus (one single proton) has an intrinsic property called spin, which is the responsible for the NMR signal production (Figure 1.1).



---

Figure 1.1: Hydrogen proton has a north-south pole. It behaves like a small bar magnet. Under normal circumstances, these hydrogen proton “bar magnets” spin in the body with their axes randomly aligned (figure on the left). When the body is placed in a strong magnetic field, such as an MRI scanner, the protons’ axes all line up (figure on the right). This uniform alignment creates a magnetic vector oriented along the axis of the MRI scanner.

From this starting point, a basic introduction to the physical principles of NMR and MRI will be given, as a necessary prerequisite for the understanding of the present thesis.

## 1.1 Interaction of nuclear Magnetization with Magnetic Field

The NMR phenomenon is produced by the interaction between a system of atomic nuclei with non-zero magnetic moment, due to a presence of non-null nuclear spins, a static magnetic field, and an oscillating magnetic field.

Briefly, when nuclei with non-null magnetic moments are affected by a static magnetic field their spins will align with the field direction and the system will be at the equilibrium with a macroscopic non-null magnetization. If a second oscillating magnetic field is applied the nuclear magnetization precesses along field’s direction until it is completely tilted into the plane and the equilibrium is broken. The resonance condition, which is at the basis of NMR and MRI signal, is reached when the frequency of the oscillating field is the same of the nuclear spins.

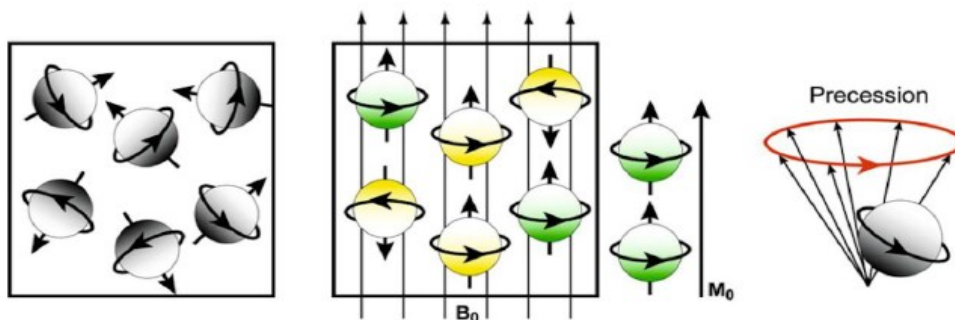


Figure 1.2: Magnetic field effect and precession.

## 1.2 Relaxation and Signal Detection

Here will be described what happens after turning off the oscillating magnetic field, usually referred to as the radio frequency (RF) field, in order to explain the mechanisms that lead to the detection of a measurable signal.

When the RF field is switched off the relaxation occurs and the nuclear magnetization, initially tilted into the plane, dynamically evolves with time until it's fully aligned with the external static field and back to equilibrium. This phenomenon is characterized by the two relaxation time constants, called longitudinal or spin-lattice ( $T_1$ ) and transverse or spin-spin ( $T_2$ ) respectively (Kuperman, 2000) which are strongly correlated to the biochemical properties of the sample. Different human brain tissues (fat, grey matter – GM, white matter – WM and cerebrospinal fluid – CSF) have different relaxation times.  $T_1$  and  $T_2$  are measured in milliseconds and depend on the static magnetic field and the used MRI sequence (Bojorquex, 2017), Table 1.1 reports an example at 3T.

Tissue	$T_1$ [ms]	$T_2$ [ms]
Gray matter	950	100
White matter	600	80
Muscle	900	50
Cerebrospinal fluid	4500	2200
Fat	350	60
Blood (arterial)	1200	200
Blood (venous)	1200	100

Table 1.1: Relaxation times  $T_1$  and  $T_2$  for all principal tissues of the human brain at 3T.

---

## 1.3 Magnetic Field Gradient and Image Reconstruction

The signal in MRI allows creating detailed images of the sample by encoding the spatial information into resonance signal. In order to achieve the spatial localization of the resonant nuclei, the dependence of the spin dynamics on the local macroscopic magnetic field is exploited. By adding a controlled inhomogeneity across the sample, in fact, it is possible to encode into the resonance signal the information on the spatial localization. MRI systems, therefore, include one further magnetic field, called gradient field, which introduces a linear variation of the field across the sample and, consequently, generates a distribution of the resonance frequencies of the nuclei along three orthogonal directions. The combined action of the three gradients, called slice selection, phase encoding and frequency encoding (Figure 1.3), allows for unambiguous identification (spatial localization) of each spin within the sample and, after a proper Fourier based reconstruction, for the generation of an image.

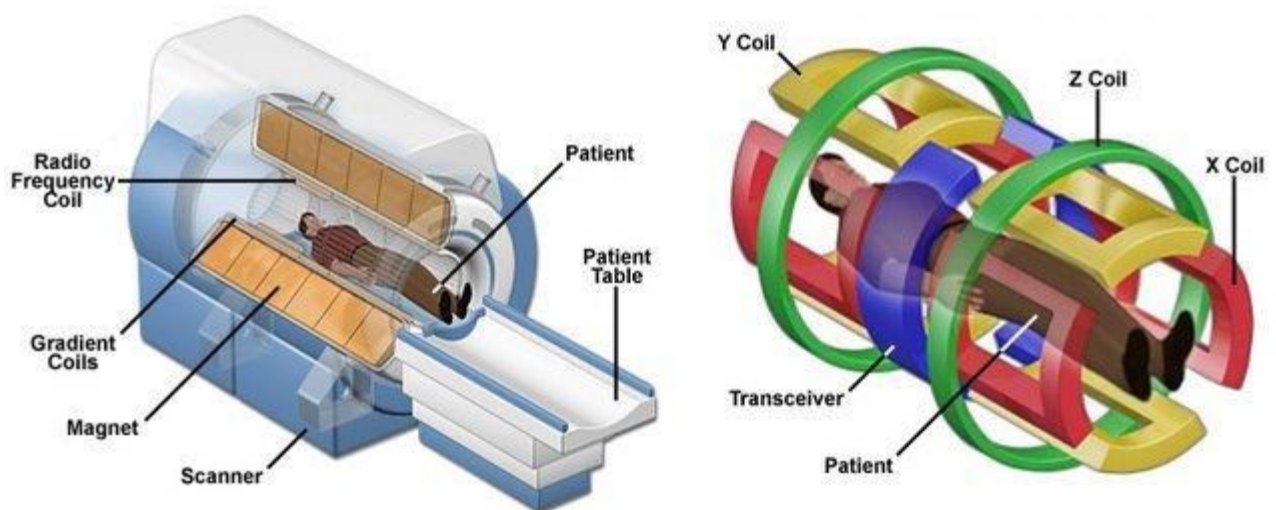


Figure 1.3: MRI scanner gradient magnets, RF transmitter and head coil as RF receiver. Each gradient is oriented along a different plane ( $x$ ,  $y$  and  $z$ ) and alters the magnetic field operating with the RF pulses to produce the scanner's image by encoding the spatial distribution of water protons in the body. Acoustic noise during MRI scan is primarily caused by Lorentz forces induced in the scanner while electric currents are switched in the gradient coils within the static magnetic field. The axial plane ( $xy$ ) slice the subject from top to bottom; the coronal plane ( $xz$ ) slice the subject from front to back; and the sagittal plane ( $yz$ ) slice the subject from left to right.

## 1.4 Pulse Sequences

An MRI scanner generates an image by executing a pulse sequence, which is a preselected set of defined RF and gradient pulses, usually repeated many times during a scan, able to control the NMR signal reception and to affect the features of the MR images. Pulse sequences are differentiated by the use of gradient pulses and therefore are specific for different acquisitions and aims. Essentially pulse sequences are computer programs that control all hardware aspects of the MRI measurement process.

The most common pulse sequences currently in use are briefly presented here.

### 1.4.1 Spin Echoes pulse sequence

Spin Echoes (SE) pulse sequence is one of the most widely used sequences in clinical images. Its popularity is both justified by its flexibility, as it can be adjusted to produce  $T_1$ -,  $T_2$ - and proton density (PD)-weighted images, and its lower sensitivity to image artefacts and field inhomogeneity with respect to other common sequences. SE sequence, in its conventional implementation, is composed by  $\pi/2$  excitation pulse followed by a  $\pi$  refocusing pulse (Figure 1.4). To acquire the image of the entire sample it is necessary to apply iteratively the combination of pulses several times. The time interval between each repetition is referred to as the Repetition Time (TR) of the sequence.

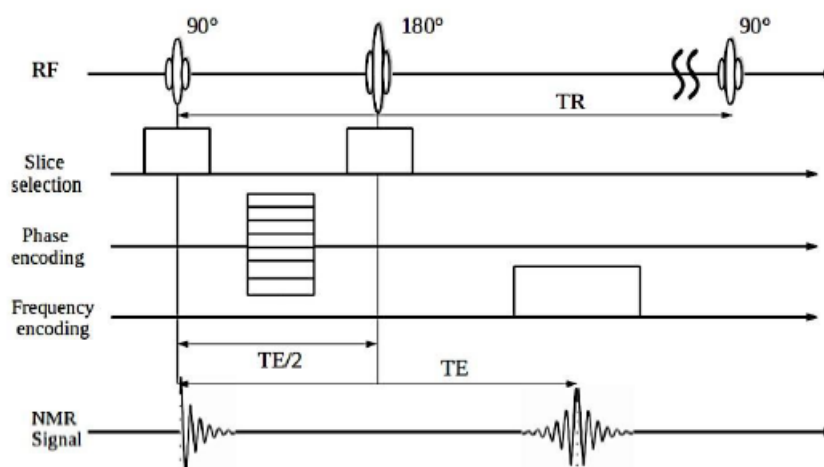


Figure 1.4: Sketch of a pulse sequence for a single-echo RF Spin-Echo.

---

## 1.4.2 SE Inversion Recovery sequence

A popular variant of the conventional SE pulse sequence described above is the SE Inversion Recovery (IR). As in the former case, this sequence is used to produce  $T_1$ -,  $T_2$ - and PD-weighted images, carefully tuning the timing of the inversion pulse with the purpose of either suppressing the signal from a specific tissue, or enhancing the contrast between two or more tissue. The Fluid Attenuation Inversion Recovery (FLAIR) represents the first most popular application of the SE-IR. In this case the IR pulse is timed to achieve a cancellation of the signal from the CSF, allowing a more accurate delineation of the edges of hyper-intense lesions in the periventricular region. IR sequence, in general, is constituted by a  $\pi$  inversion pulse followed by the conventional SE sequence of pulse described above (Figure 1.5). The time delay between the first  $\pi$  pulse and the following SE  $\pi/2$  pulse is called Inversion Time (TI).

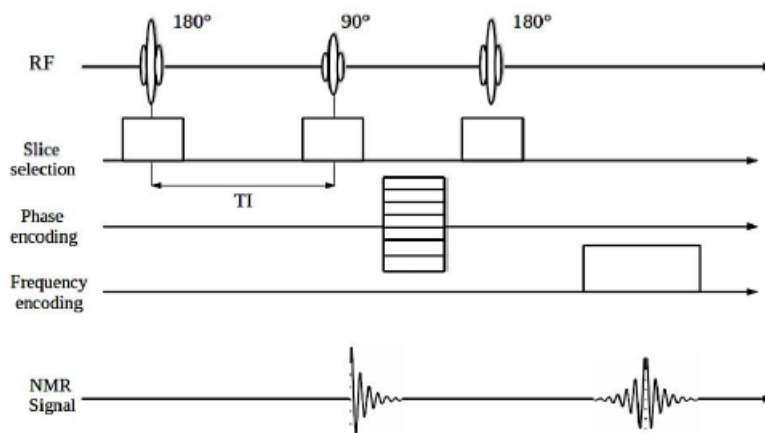


Figure 1.5: Sketch of a timing diagram for a generic Inversion Recovery pulse sequence.

## 1.4.3 Gradient Echoes pulse sequence

The Gradient Echoes (GE) pulse sequence accounts, together with the SE, for a large majority of the clinical imaging applications. This was the first class of sequences used to produce fast MRI. Particularly, by using GE pulse sequences it is possible to reduce the acquisition time allowing for the adoption of 3D acquisition schemes in a clinically acceptable time. The application of a pair of bipolar gradient pulses generates a gradient echo. In the pulse sequence-timing diagram reported 10/03/2022 in Figure 1.6, the basic GE sequence is

reported. For this family of sequences, the TR is usually short and the magnetization is not completely recovered at the TE, so an excitation pulse with flip angle lower than  $\pi/2$  is used.

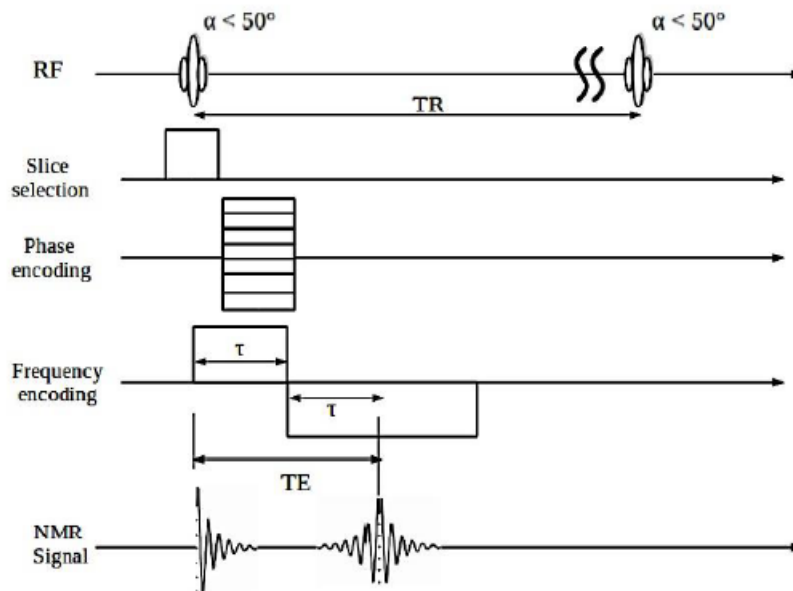


Figure 1.6: Sketch of a pulse sequence for a simple Gradient Echo.

#### 1.4.4 Fast Scanning Techniques and Echo Planar Imaging

Once the theoretical underpinnings of the MRI technique were understood, researchers focused on the development of new pulse sequences that decreased scanning time while increasing signal-to-noise ratio. A classical spin-echo sequence, where a  $\pi$  refocusing pulse is used to create a train of echoes, gave way to more efficient scanning techniques referred to as fast spin echo (FSE) or turbo spin echo (TSE) technique. FSE techniques are characterized by a changing phase-encoding gradient for each echo. While TSE techniques significantly decreased scanning time, the true game changer was the development of the gradient echo (GE) sequence and its combination with multi-shot echo planar imaging (EPI). The two main features that set GE sequences apart from all the others is the absence of a  $\pi$  re-phasing pulse and a flip angle that is lower than  $\pi/2$ . After the RF pulse, a dephasing gradient is applied and then subsequently reversely applied in order to create the echo. This drastically decreases the echo time. On the other hand, a lower flip angle decreases the time between each TR as the longitudinal magnetization recovers faster from a 30-degree nutation than a 90-degree

---

nutration. Thus the combination of a short TE and a short TR echo means an acquisition time of 100 ms per slice.

The compromise between low spatial resolution images with a high temporal resolution enabled researchers to look at the dynamic changes of the brain signal during a time series. Once the measured brain signal was attributed to a specific feature, be it water molecule movement or ratio of oxygenated to de-oxygenated haemoglobin, a new prolific field of research populated by *functional magnetic resonance images, diffusion weighted images, and resting-state functional magnetic resonance images*, was born.

## 1.5 Image Contrast

The contrast in MR images is determined by a combination of several factors (Figure 1.7); this fact explains the great success of MRI in medical imaging. A careful choice of pulse timing, shapes and combinations allows highlighting multiple components and properties of the tissue and the clinical information associated with pathological conditions.

The primary source of contrast is the spin density within the observed sample. An image displaying a spin density-weighted contrast, usually referred to as proton density (PD) weighted contrast, can be obtained using TR “much longer” than the T1 and TE as short as possible, in order to minimize T1 and T2 effects respectively. Since within many organs, such as the brain, the variation of spin density among different tissues is small, PD-weighted images do not display high contrasts between tissues and are weakly sensible to pathology. This situation suggests how exploiting other contrast mechanism is necessary in clinical imaging.

The most intuitive applications exploit the contrast arising from the local variation in the values of the spin-lattice relaxation time T1 and the spin-spin relaxation time T2. When an accurate definition of the timing parameters is performed these images display a contrast determined by either of the relaxation processes and are referred to as relaxation time weighted images. A T1-weighted image can be obtained in its simplest form by choosing a TR smaller or comparable to the T1 of the scanned tissues and a TE as short as possible. Similarly, a T2-weighted image can be obtained by adopting a TR longer than the T1 of the scanned tissues and a TE similar or longer than the shortest T2 of observed tissues.

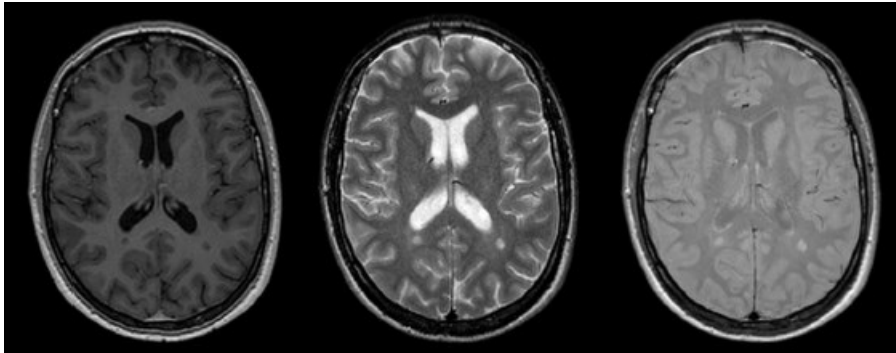


Figure 1.7: weighted image in  $T_1$ ,  $T_2$  and proton density  $p$  (from left to right).

## 1.6 MRI TECHNIQUES

In the previous section fundamental pulse sequences and image contrasts have been presented. Here are reported main features of the MRI techniques used in the present thesis. In particular, it is worth notice that the combination of different MRI techniques, such as structural, functional, and diffusion, could elucidate the structural and functional features of the investigated neurological disease.

### 1.6.1 Structural T1-weighted MRI

Structural MR imaging (sMRI) is usually performed using sequences belonging to the family of IR sequences with a 3D acquisition scheme and it is classically referred to as 3DT1. This choice is done in order to provide images with a high spatial resolution and a very good tissues contrast.

Structural MRI is the most widely used neuroimaging technique for diagnosing and evaluating progression of neurological disorders, such as Alzheimer's disease, in clinical and research settings. Post mortem studies have confirmed the anatomical validity of structural MRI volume measurements by establishing correlations between neuronal loss in histological slices and atrophy level observed with MRI.

A widely used method in morphological studies is the Voxel-based morphometry (VBM) analysis (Ashburner & Friston, 2000). It involves a voxel-wise comparison of the local concentration of grey matter between groups thus allowing to compare density and volumetric values. The procedure involves spatially normalizing high-resolution images from

---

all the subjects into the same stereotactic space. This is followed by grey matter segmentation from the spatially normalized images and smoothing. The last process is the voxel-wise parametric statistical tests to compare the smoothed grey-matter images. Corrections for multiple comparisons are made using the theory of Gaussian random fields.

## 1.6.2 Diffusion MRI

The diffusion imaging sequence, in its conventional implementation, belongs to the family of the SE sequence with an echo-planar acquisition scheme. Compared to the spin-echo sequence introduced previously, the diffusion sequence has an additional set of gradient pulses referred to as Gd. This is a key feature, because allows diffusion imaging to generate images sensible to the motion of the water molecules within the sample.

The Gd pulse is applied along the x, y, or z direction to obtain images dependent upon the water diffusion in x, y, or z directions respectively. The two Gd pulses reported in figure (Figure 1.8) are identical in amplitude and width ( $\delta$ ), separated by a time  $\Delta$ , and placed symmetrically about the  $180^\circ$  pulse. The function of the Gd pulses is to dephase magnetization of those spins that have diffused to a new location during the  $\Delta$  period of time. These pulses have no effect on stationary spins.

Diffusion imaging was initially used for assessing vascular neurological diseases, such as stroke. It has found additional application in studying the microstructural architecture and the structural connectivity of the brain, i.e. for identifying the most important axonal bundles of the brain. In order to provide anatomically accurate reconstructions of the axonal bundles of the brain, a diffusion technique called diffusion tensor imaging (DTI) has been developed. In this case Gd pulses, and so diffusion images, are acquired along at least six different directions and it is possible to infer diffusion properties and to reconstruct the diffusion tensor for each voxel of the image.

DTI is employed to measure the WM structural integrity. The basic DTI principle is that the water molecules' diffusion is greater along the WM fibre tracts than perpendicular to them (Basser et al., 2000). Fractional anisotropy (FA) and mean diffusivity (MD) are the most frequently used parameters derived from DTI data. FA is a measure of the degree of

anisotropy, i.e. directionality of water diffusion in the tissue (FA=0 corresponds to isotropy / FA=1 corresponds to maximum directionality), and represents the directionality of the WM fibres (a low FA value corresponds to little directional fibres and then to damaged fibres). MD is calculated as the mean of the diffusion along the three principal axes and represents the measure of total diffusion in a voxel (a high MD value is associated with an alteration) (Concha, 2014).

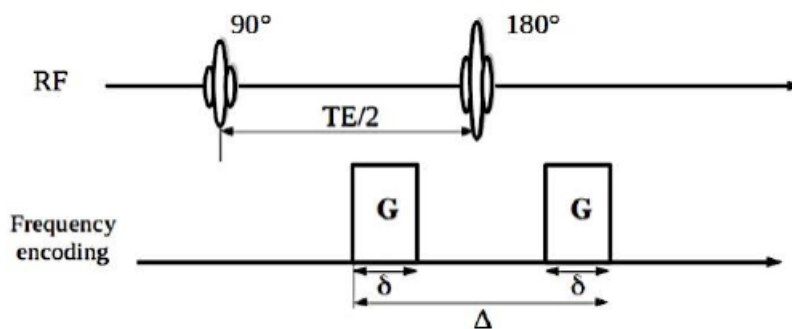


Figure 1.8: Example of SE pulse sequence with the addition of two gradients.

Different methods for analysing DTI data, i.e. “regions of interest” (ROI) and voxel-wise approaches, exist and it makes difficult to compare different studies. Furthermore, the results reported in different works seem to be strongly dependent on the chosen methodology. The main difference between ROI-based and voxel-wise approaches is that the former investigates pathological alterations only in a region defined on the basis of a priori information, while the latter could detect and localize alterations in the whole brain. The usage of either these techniques is very useful in the study of microstructural alterations due to neurological disorders, nevertheless they are affected by non-negligible limitations, such as registration errors. To overcome some of these limitations the tract-based spatial statistics (TBSS) technique has been recently developed (Ashburner & Friston, 2001). Moreover, this method seems to provide more consistent results than the others (Smith et al., 2006).



## ***Chapter 2***

# **Temporal Lobe Epilepsy: 3TLE multicentre study**

In this chapter, the necessary notions will be provided to have an adequate overview to understand the pathology that will be treated in the following chapters. Moreover, will be introduced the Network project that provided all the data used for the analysis. NET-2013-02355313 entitled: “Magnetic resonance imaging in drug-refractory temporal lobe epilepsy: standardization of advanced structural and functional protocols at 3T, to identify hippocampal and extrahippocampal abnormalities” (3TLE).

## **2.1 Epilepsy**

Epilepsy is a chronic neurological disorder characterized by the occurrence of epileptic seizures, defined as clinical manifestations with paroxysmal occurrence, characterized by signs and / or symptoms due to neuronal activity resulting from an abnormal hypersynchronous discharge of a population of brain neurons. It is a sudden and transient manifestation, the symptoms of which depend on the brain area affected by the discharge. the crisis, therefore, can be characterized by a wide variety of motor, psychic and sensory phenomena, with or without compromise of consciousness and the ability to interact with the environment, the dysfunctions of which will result from the neuronal populations involved and the pathways of diffusion of the discharge.

### **2.1.1 Pathophysiology**

From a neurobiological point of view, decades of experimental studies have identified the disruption of the normal balance between neuronal activity and inhibition as the pivotal

---

mechanism for the genesis of seizures in an otherwise healthy brain (Scharfman, 2007). It is clear that if this argument can be valid for healthy tissue exposed, for example, to toxic factors or acute insults leading to isolated secondary seizures (i.e. in acute trauma, dysmetabolic conditions, or febrile seizures), it cannot be as straightforward for epilepsy proper, a pathological conditions leading to repeated seizures, which implies a profound modification of the normal neuronal structure both from a structural and functional point of view.

The alteration of the excitation/inhibition balance, in fact, can occur at different levels of brain function, at the level of genes and subcellular signal but also at the level of diffuse neuronal circuits. Genetic pathologies that condition the occurrence of epilepsy may be linked to alterations both at the level of networks (abnormal synaptic connectivity in cortical dysplasia), at the receptor level (alterations of GABA receptor subunits in Angelman syndrome), and at the level of ion channel functioning (potassium channel mutations in benign familial neonatal seizures) (Stafstrom & Carmant, 2015). Such alterations are responsible for the recurrence of seizures. It is not surprising, therefore, that the molecular mechanisms underlying epilepsy are still being studied and that the evolution of research in genetics continuously opens new perspectives for a better understanding (Staley 2015).

### 2.1.2 Epileptic seizure

It is important to distinguish "provoked" and "unprovoked" seizures as they are an integral part of the clinical-practical definition of epilepsy and are associated with very different prognoses. The provoked seizure is the result of the action of a transient insult on an otherwise normal brain, which temporarily alters the neuronal excitability. This insult can be represented by any brain pathology that does not determine in the person a lasting predisposition to develop epileptic seizures: a cranial trauma or a neurosurgical intervention could cause a single seizure as a transient epiphenomenon of a temporary impairment of brain networks (provoked seizure) while a cortical dysplasia or a neoplasm could permanently alter specific neuronal networks predisposing a particular brain area to develop seizures (unprovoked seizures).

Regarding the type of seizure, as known, we distinguish generalized seizures and focal seizures (Scheffer et al. 2017). Generalized crises are characterized by the immediate, extensive

cortical and subcortical involvement of both hemispheres, but not necessarily of the whole cortex. Because of common involvement of the motor cortex, they can be of tonic-clonic, tonic, clonic, atonic, myoclonic. In other cases, with a prevalent consciousness impairment and minimal motor manifestation, generalized seizures present as absence type, often benign in children. Focal seizures, on the other hand, originate in a precise area, mostly of a single hemisphere; for each type of focal seizure the area (cortical or subcortical) that is activated is the same in different ictal episodes and is called Epileptogenic Zone (EZ). Starting from this zone of origin, the discharge can then spread, following patterns of preferential propagation, to involve other regions of the same hemisphere or of the contralateral hemisphere. Among partial seizures, we distinguish simple partial seizures, i.e. without alteration of consciousness, and complex partial seizures, in which consciousness is compromised or lost.

### 2.1.3 Diagnosis

The expanded and recently confirmed diagnosis of epilepsy is defined as follows (Fisher et al., 2016):

1. At least two unprovoked, or reflex, seizures, i.e. seizures not sustained by an obvious and immediate preceding cause or acute brain event, occurring separately in a time period greater than 24 hours;
2. One unprovoked, or reflex, seizure and a probability of further seizures similar to the overall risk of recurrence (at least 60%) after two unprovoked seizures within the next 10 years;
3. Diagnosis of epilepsy syndrome, that is, an epilepsy characterized by symptoms and signs, clinical and electroencephalographic, such that they constitute a special clinical condition.

### 2.1.4 Classification

The classification of epilepsies is, even today, a continuously evolving process whose ultimate goal is to establish a clinically useful classification based on scientific evidence. Over time, the information resulting from the continuous progress in science, in particular genetic and molecular biology but also technological, for example in the field of neuroimaging, have

allowed and necessary the revision and updating of classifications. The International League Against Epilepsy (ILAE), published an update to its epilepsy classification system (Scheffer et al., 2017) that presents three levels of diagnostic intervention (Figure 2.1). The first step is the diagnosis of the seizure type, after which the epilepsy type is selected from focal epilepsy, generalized epilepsy, combined generalized and focal epilepsy, and a group of epilepsies about which little is still known. The third level is that of diagnosis regarding the specific epilepsy syndrome.

The etiology is subdivided into six subgroups, based on potential therapeutic consequences, and its importance is emphasized at every step of the diagnosis. The purpose, expressed by the authors, is to facilitate classification and communication about the type of seizures among clinicians, the nonmedical community, and researchers.

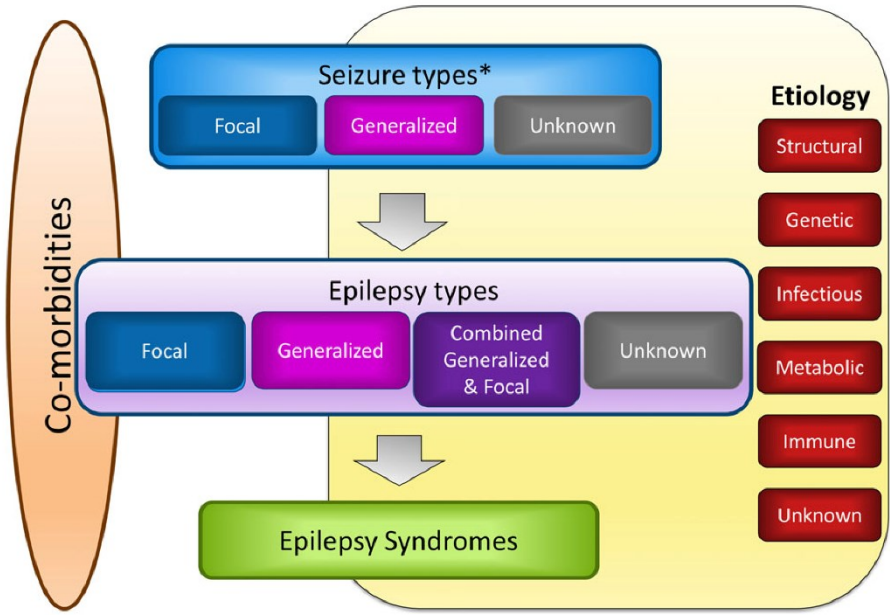


Figure 2.1: Framework for classification of the epilepsies. \*Denotes onset of seizure. Epilepsia ILAE (Scheffer et al., 2017)

### 2.1.5 Epidemiology

From the set of published data, it appears that the annual incidence rate of epilepsy is 61.4 per 100,000 inhabitants (Fiest et al, 2017). The incidence of epilepsy is slightly higher in the male gender than in the female gender (Fiest et al, 2017), regardless of country of origin. This

gender difference could be due to genotype, a different prevalence of risk factors in the two sexes, or concealment of the disease in women for sociocultural reasons (Fiest et al, 2017).

### 2.1.6 Neuroimaging in Epilepsy

Over the years, MRI of the brain has become increasingly important for the diagnosis, prognosis and treatment of epilepsy. In addition to providing precise information on the anatomical location of any lesions causing epilepsy, it allows a fundamental characterization for the etiological diagnosis (neoplastic, infectious, ischemic lesions, cortical malformations, etc.). In addition, the detailed study of certain brain regions with appropriate sequences allows to highlight specific structural abnormalities (e.g. detail of temporal regions for hippocampal sclerosis), to distinguish between various epileptogenic lesions (e.g. low-grade tumors, malformation of cortical development, vascular malformations, post-traumatic scars) and to identify any functional or structural consequences of intense and sustained epileptic activity. Temporary abnormalities in certain sequences (cortical gyral hyperintensity in the diffusion study) when present, can be a useful diagnostic confirmation of ongoing or recent epileptiform activity. Functional MRI studies of eloquent areas are useful for the evaluation of patients with drug-resistant focal epilepsy who are candidates for neurosurgical treatment. A normal MRI picture may be the preserve of presumably genetic (idiopathic) epilepsies as well as forms of unknown aetiology.

## 2.2 3TLE project

### 2.2.1 Background and motivation

Approximately 30-40% of patients with epilepsy show drug-resistant epilepsy (Kalilani et al., 2018), meaning that seizures persist despite the administration of an adequate and well-tolerated antiseizures pharmacological treatment. Surgical intervention in drug-resistant epilepsy has a positive outcome in around 70% of cases (Jayalakshmi et al., 2016; Salanova et al., 2002), (Yıldırım Capraz et al., 2015). Amongst all different types of epilepsy, temporal lobe epilepsy (TLE) is the most common form of focal epilepsy (Blair, 2012; Jallon et al., 2001). The aetiology of TLE presents a wide variety of possible causes as shown by histopathological

---

analysis, revealing combinations of focal acquired lesions, cortical malformations, and hippocampal sclerosis (Blumcke et al., 2017). In some cases, referred to as cryptogenic, there is no associated histopathological alteration of tissue properties unless than diffuse aspecific gliosis due to secondary neurodegeneration.

In addition to seizures, subjects with epilepsy often suffer alterations in cognitive performance that depend on the side of the epileptogenic zone; in particular, verbal memory dysfunctions, is more evident in subjects with lesions in the left hippocampus (Alessio et al., 2004). A marked association between cognitive abilities and white matter abnormalities (Rodríguez-Cruces et al., 2018) has also been found in TLE patients with the epileptogenic zone in the left hemisphere, whereas TLE patients with the epileptogenic zone in the right hemisphere have shown deficits in the recognition of emotional categories (Sedda et al., 2013).

In TLE, even in the presence of isolated hippocampal sclerosis on MRI, histological analysis after temporal lobectomy can reveal a second lesion which should be included in the resection. 3T MRI, multichannel head coils, and new sequences are promising tools to improve detection of subtle lesions (Madan et al., 2009). In TLE, among advanced sequences, DTI can detect microstructural abnormalities in the temporal pole (Widjaja et al., 2011).

### 2.2.3 Aim

This Network Project of the Neuroimaging Commission of the Lega Italiana Contro Epilessia (LICE) aims to define advanced structural/functional 3T MRI protocols to be applied in epilepsy centers affiliated with the *Sistema Sanitario Nazionale* for the diagnostic workup of patients with temporal lobe epilepsy (TLE). Italy has an estimated 140,000 patients with drug-refractory epilepsy, most TLE. Temporal lobectomy suppresses seizures in ~60-80% of case.

The protocols of 3T MRI acquisition developed in this study provides enhanced visualization of hippocampal substructures and of cortico-subcortical demarcation in the temporal lobe, ultimately allowing to improve detection of subtle abnormalities.

The quantitative analysis of advanced structural and functional 3T-MRI could detect extrahippocampal abnormalities not identifiable on visual assessment, but correlated with ex-vivo 7T-MRI histopathological abnormalities within the surgical resected temporal pole and,

postsurgical outcome on seizure remission. Overall, compared to 1.5T MRI, 3T MRI with advanced quantitative techniques is expected to show increased sensitivity to detect hippocampal and extrahippocampal abnormalities in TLE patients.

---

## *Chapter 3*

# **White matter microstructure characterisation in Temporal Lobe Epilepsy**

Temporal lobe epilepsy (TLE) is the most common form of focal epilepsy. Determination of the side and site of the epileptogenic zone currently relies on anatomo-electro-clinical testing. Similarly, aetiology of epilepsy is currently based on tissue histology. Preoperative confirmation of this information would be an important contribution to surgical planning and outcome prediction. Microstructural abnormalities from diffusion tensor imaging (DTI) have differentiated Left and Right TLE (L-TLE and R-TLE) with few reported voxelwise comparisons of advanced metrics (Scanlon 2013, Liu 2014, Tsuda 2018) .

The purposes of this work were (i) to identify patterns of white matter alterations using diffusion metrics across the whole white matter to assess pre-operatively differences between L-TLE and R-TLE groups; (ii) to test sensitivity of temporal lobe microstructure parameters to tissue histology and surgical outcomes; (iii) to assess whether diffusion kurtosis imaging (DKI), and NODDI metrics added to DTI provide complementary and more sensitive information.

MRI data were acquired on fifty-two TLE patients (23 L-TLE, 33.1±11.2 years, 13 females; and 29 R-TLE, 38.0±9.9 years, 16 females) and 36 healthy controls (32.9±8.4 years, 17 females).

All MRI data was acquired pre-surgery. In order to achieve the three aims above, we performed two analysis: one focusing on classification of patients pre-surgery, using DTI, DKI and NODDI tract-based spatial statistics, and one correlating MRI with known surgical outcomes performing and temporal lobe ROIs analysis and general linear model to assess differences in microstructural metrics between groups. Briefly, were performed, was performed .

We found extensive WM damage in L-TLE, both in cerebral and cerebellar regions; more localised WM alteration in R-TLE. Neurite density index was altered in patients with hippocampal sclerosis but not in cryptogenic patients.

Our results support the potential role of diffusion indices to characterise patients preoperatively, including their ability to confirm the side and extent of pathological damage. The use of DKI and NODDI metrics, added to DTI, can help characterise TLE pathology, potentially aiding surgical planning.

## 3.1 Background and motivation

As introduced in Chapter 2, amongst all different types of epilepsy, temporal lobe epilepsy (TLE) is the most common form of focal epilepsy (Blair, 2012; Jallon et al., 2001). The aetiology of TLE presents a wide variety of possible causes as shown by histopathological analysis. In some cases, referred to as cryptogenic, there is no associated histopathological alteration of tissue properties.

Magnetic resonance imaging (MRI) is routinely used to improve diagnosis and prognosis of neurodegenerative pathologies and neurological diseases and can assume a crucial role for characterizing pathological conditions. In vivo MRI studies in epilepsy patients, have revealed structural abnormalities both in grey and white matter (Liu et al., 2016). While WM abnormalities are generally considered secondary to the primary grey matter disease, scans of resected tissue from the temporal pole performed on a 7T MRI scanner have demonstrated chronic degeneration in TLE patients with hippocampal sclerosis (Garbelli et al., 2012). Another study using DTI showed that white-matter alterations are mainly ipsilateral to the seizure focus, but are more spread in TLE patients with the epileptogenic zone in the left than in the right hemisphere (Ahmadi et al., 2009), although the opposite has also been reported (Lemkaddem et al., 2014; Sone et al., 2018).

DW-MRI is widely used to study the microstructural architecture of the brain and its abnormalities. This characterization can be achieved because diffusion MRI is based on the investigation of the Brownian motion of the water molecules, which is hindered and restricted

---

by the microstructural brain architecture, hence providing useful, though indirect, information about anisotropic properties of myelinated fiber bundles.

DTI, the most basic application of DW-MRI, provide directionally invariant quantitative metrics, like the fractional anisotropy (FA), which are reproducible among subjects, sessions and scanners. More advanced diffusion models proposed over the years have been demonstrated to be more sensitive and specific to microstructural alterations. Metrics defined using DKI (Jensen et al., 2005), which investigates diffusion properties beyond the gaussian behaviour captured by the DTI, have shown greater sensitivity than DTI metrics in detecting and localizing changes in several diseases (Guglielmetti et al., 2016; Winston, 2015), including TLE (Del Gaizo et al., 2017). Efforts have also been dedicated to study the diffusion behaviour of water in brain tissue using computational models that depend on microstructural organisation assumptions. Among multi-compartment approaches, neurite orientation dispersion and density imaging (NODDI) is currently the most used, because it can be run on clinical scanners in relatively short acquisition times, is conceptually simple, and there are tools available for the analysis; indeed, NODDI is able to provide multiple parameters that can disentangle the different microstructural contributions to FA changes, such as the neurite density index (NDI) and the orientation dispersion (ODI) of dendrites and axons (Xiong et al., 2019; H. Zhang et al., 2012). It has been proposed that this microstructural information may be useful in epilepsy because it can identify lesions such as cortical dysplasia that are often not recognized on conventional MRI or other quantitative diffusion maps such as FA (Winston et al., 2014).

Global information about WM alterations can be provided by tract-based spatial statistics (TBSS), a fully automated data analysis technique that uses a voxel-wise approach to detect abnormalities in diffusion metrics, while minimizing the effects of misalignment introduced by registration in conventional voxel-based analysis methods (Smith et al., 2006). Few TBSS studies in TLE patients have focused on DKI or NODDI-derived metrics, while commonly only DTI metrics have been used. To the best of our knowledge, none of these studies investigated differences between TLE patients having the epileptogenic zone clinically defined as in the left (L-TLE) or right hemisphere (R-TLE). Moreover, it remains unclear whether microstructural

alterations detected with in vivo diffusion MRI distinguish different aetiologies of the disease, and whether they could be used to predict surgical outcome.

This work therefore, combines DTI, DKI, and NODDI-derived metrics on a large cohort of subjects, equally distributed pre-operatively in 3 groups: healthy controls (HC), and clinically defined L-TLE or R-TLE. TBSS was applied to DTI, DKI and NODDI-derived metrics in order to assess whether (i) specific patterns of WM alterations exist in L-TLE and R-TLE groups that could support pre-operative clinical diagnosis, and whether (ii) DKI and NODDI-derived metrics provide information that is complementary to standard DTI-derived metrics. Moreover, with a post-hoc analysis we aimed to (iii) associate microstructural alterations in groups of patients with histological outcomes, and (iv) assess whether we could identify metrics that are predictive of surgical outcome.

## **3.2 Protocol Design**

### **3.2.1 Subjects**

The study was carried out in accordance with the Declaration of Helsinki with written informed consent from all subjects according to an ethical committee approved protocol.

The inclusion criteria were diagnosis of TLE and potential candidate for surgery; resistance to antiepileptic drugs according to International League Against Epilepsy (ILAE) criteria (Kwan et al., 2010) and age between 14 and 55 years. The exclusion criteria were large gliotic-malacic brain lesions and severe encephalic lesions; impossibility to perform MRI protocol due to physical or mental limitations, or contraindications to MRI.

TLE was diagnosed according to criteria defined by the ILAE (Scheffer et al., 2018). All patients underwent a comprehensive neurological evaluation. Seizures were lateralized according to medical history, neurological examination, interictal electroencephalography (EEG), video-EEG, and in some cases, invasive recordings (Stereo-EEG) or positron emission tomography (PET).

After surgery, histopathological of the resected tissue and Engel classification (Engel, 1993) were evaluated, and patients were clinically assessed at least at 2 years from surgery.

Age and gender matched healthy controls (HC) were recruited from university students and hospital staff. The inclusion criteria were age 19-55 years. The exclusion criteria were presence of current or previous neurological or psychiatric pathology, and the presence of two or more cardiovascular risk factor.

*Patient Characteristics:*

Fifty-two TLE patients (35.8±10.7 years, 29 females) and 36 HC (32.9±8.4 years, 17 females) were analysed. According to the criteria defined previously, 23 patients were clinically classified as L-TLE (33.1±11.2 years, 13 females) while 29 as R-TLE (38.0±9.9 years, 16 females).

Table 3.1 reports demographic and clinical features of all subjects while Table 3.2 reports the classification according to the outcome of the histological analysis of the resected specimens and the Engel classification per patient group. It can be seen that the two major histological groups were cryptogenic epilepsy (Crypto) (19 subjects) and hippocampal sclerosis Epilepsy (HS) (11 subjects); 38 out of 52 patients (73%) were classified as seizure-free after surgery (Engel Ia). Of those with worse surgical outcomes (Engel > Ia), 8 belonged to the cryptogenic patient group.

	HC (n=36)	L-TLE (n=23)	R-TLE (n=29)	p-value
Age (years)	32.9 ± 8.4	33.1 ± 11.2	38.0 ± 9.9	<0.033
Gender (F/M)	17 / 19	13 / 10	16 / 13	n.s.
Age at onset (years)	-	19.1 ± 11.8	23.8 ± 12.6	n.s.
Duration (years)	-	14.0 ± 11.2	14.5 ± 11.6	n.s.
Frequency (seizures/month)	-	4.9 ± 6.2	6.6 ± 8.6	n.s.

Table 3.1: Demographic table for healthy controls and TLE patients. All values are reported as mean ± standard deviation. "n.s." = not significant.

Histopathology	L-TLE (n=23)			R-TLE (n=29)		
	Tot	Engel - Ia	Engel other	Tot	Engel - Ia	Engel other
Cryptogenic	4	2	2	15	9	6
Hippocampal Sclerosis	6	6	-	5	4	1
Lesion	9	7	2	6	6	-
Encephalitis	1	1	-	1	-	1
Polymicrogyria	1	-	1	-	-	-
Focal cortical dysplasia	2	1	1	2	2	-

Table 3.2: Distribution of patients according to histopathology and Engel classification. Lesion = patients with tumor or cavernoma; Tot = total number of patients. Engel classification was obtained between 25-40 months after surgery. "Other" includes classification higher than Ia.

### 3.2.2 MRI acquisition

MRI data were acquired with a 3T Siemens Skyra scanner (Siemens Healthineers, Erlangen, Germany). In addition to routine clinical sequences, DW images were acquired with a two-shell twice refocused SE-EPI sequence using the following parameters: TR=8400 ms, TE=93 ms, 70 axial slices with no gap, 2.2 mm<sup>3</sup> isotropic voxel resolution, 48 volumes with non-collinear diffusion directions with b=1000/2000 s/mm<sup>2</sup> and 13 non-DW volumes (b=0 s/mm<sup>2</sup>). A 3DT1-weighted (T1) image was acquired with a multi-echo FLASH sequence: TR/TE=19/2.46 ms, flip angle 23°, 176 sagittal slices, 1mm<sup>3</sup> isotropic voxel).

### 3.2.3 MRI processing

Standard pre-processing steps comprising of correction for Gibbs-ringing artifacts, noise-floor, eddy-current induced geometrical distortions, and motion were performed on the DW-images

---

combining commands from the MRtrix3 (<https://www.mrtrix.org/>) (Tournier et al., 2019) and FSL (<https://fsl.fmrib.ox.ac.uk/fsl/fslwiki/FSL>) (Jenkinson et al., 2012) toolboxes.

Pre-processed data were used to derive diffusion metrics under several models. DESIGNER (<https://github.com/NYU-DiffusionMRI/DESIGNER>) (Ades-Aron et al., 2018) was used to fit the gaussian (DTI) and non-gaussian (DKI) part of the signal, more linked to the complexity of the microstructural environment (Steven et al., 2014), and to calculate maps of FA, mean, axial and radial diffusivities (MD, AD and RD), and mean, axial and radial kurtosis (MK, AK and RK). Three-compartment NODDI model (H. Zhang et al., 2012) provided ODI and NDI maps, which can explain the source of diffusion anisotropy, and was fitted to the signal using the Matlab toolbox ([https://www.nitrc.org/projects/noddi\\_toolbox](https://www.nitrc.org/projects/noddi_toolbox)).

## **3.3 Study I: Pre-surgery whole-brain analysis**

### **3.3.1 Tract-based spatial statistic (TBSS)**

Whole-brain voxel-wise analysis was performed on the entire cohort using TBSS (FMRIB, <https://fsl.fmrib.ox.ac.uk/fsl/fslwiki/TBSS/UserGuide>) (Smith et al., 2006). FA maps from each subject were non-linearly registered to each other for identifying the “most representative” subject, which was then used as the target to non-linearly align, namely to normalize, all FA images to the MNI152 (1x1x1 mm<sup>3</sup>) template. All normalized FA maps were averaged, and the mean FA image was thinned to create a mean FA skeleton of core WM voxels by imposing a threshold at 0.2. The normalized FA of each subject was projected onto the mean skeleton to create a subject-specific skeleton. These subject-specific skeletons were inputted in the voxel-wise statistics to test for group differences. The other DTI, DKI and NODDI metrics were likewise projected onto the mean FA skeleton by applying the same non-linear registration used for projecting FA onto the MNI152 template.

The statistical voxel-wise analysis was performed with a permutation-based inference approach of 5000 permutations on the skeletonized images for each metric using the randomize command. Age and gender were used as covariates. Comparisons were performed independently for all metrics (FA, MD, AD, RD, MK, AK, RK, ODI, NDI) using an ANOVA test

including all subjects according to the pre-surgical lateralization of their seizures. For each metric, results were corrected for multiple comparisons (family-wise error, FWE) using the threshold-free cluster enhancement (TFCE) algorithm, and the significance level was set at  $p=0.05$ . Four pairs of groups were compared:

1. **HC versus all-TLE patients**
2. **HC versus L-TLE**
3. **HC versus R-TLE**
4. **L-TLE versus R-TLE**

### 3.3.2 Results

#### HC vs all-TLE:

A first comparison was performed between HCs and all-TLE patients to give a global description of WM alterations induced by TLE. Alterations were found throughout the brain in all diffusion metrics, except for AD and AK, as reported in the first column of Table 3.3.

Brain region	HC vs all-TLE		HC vs L-TLE		HC vs R-TLE		L-TLE vs R-TLE	
Hemisphere	Left	Right	Left	Right	Left	Right	Left	Right
Frontal Lobe	FA, MD, RD	FA, MD, RD	FA, MD, RD	FA, RD	FA, RD	FA, RD	-	-
	MK, RK	MK, RK	MK, RK	MK, RK	MK, RK	MK, RK	-	-
	ODI, NDI	ODI, NDI	NDI	NDI	ODI	ODI	-	-
Parietal Lobe	FA, RD	FA, RD	FA, MD, RD	FA, RD	-	-	-	-
	MK, RK	MK, RK	MK, RK	-	RK	RK	-	-
	ODI	ODI, NDI	NDI	NDI	ODI	ODI	-	-
Occipital Lobe	FA, RD	FA, RD	FA, RD	FA, RD	FA	FA	-	-
	MK, RK	MK, RK	MK, RK	-	RK	RK	-	-
	ODI	ODI	NDI	NDI	ODI	ODI	-	-
Temporal Lobe	FA, RD	FA, RD	FA, MD, RD	FA, RD	FA	FA, RD	FA, MD, RD	-
	MK, RK	MK, RK	MK, RK	-	RK	MK, RK	-	-
	ODI, NDI	ODI, NDI	NDI	-	ODI	ODI	-	-
Diencephalon	FA, RD		FA, MD, RD		FA		FA, RD	
	MK, RK		-		RK		-	
	ODI		ODI, NDI		ODI		-	
Brainstem	FA, RD		FA, RD		-		FA	
	RK		-		RK		-	
	ODI		ODI		ODI		-	
Cerebellum	FA	FA	FA, RD	FA, RD	AD	AD	MD, AD, RD	MD
	-	-	-	-	-	-	-	-
	ODI	ODI	-	ODI	ODI	ODI	-	-

Table 3.3: Metrics revealing significant alterations for each anatomical region in all TLE patients. Significant differences of all-TLE (first column), left TLE (L-TLE, second column), right TLE (R-TLE, third column) with respect to healthy control (HC) and L-TLE compared to R-TLE (fourth column). FA: Fractional Anisotropy; MD: Mean Diffusivity; AD: Axial Diffusivity; RD: Radial Diffusivity; MK: Mean Kurtosis; AK: Axial Kurtosis; RK: Radial Kurtosis; ODI: Orientation Dispersion Index; NDI: Neurite Density Index.

HC vs L-TLE:

TBSS results (second column of Table 3.3) on DTI-derived metrics revealed significant widespread bilateral FA reduction and RD increase in cerebral and cerebellar WM in L-TLE (defined clinically and pre-operatively) compared to HCs, with the exclusion of the right temporal lobe. Increased MD was predominantly found in the left cerebral hemisphere and involved diencephalon, temporal, parietal and frontal lobes (Figure 3.1a).

DKI maps revealed decreased MK and RK in widespread brain regions, with the exclusion of the cerebellum, brainstem and a large portion of the right temporal lobe (Figure 3.1b).

NODDI maps showed widespread increased ODI in diencephalon, brainstem and right cerebellum. Changes in the temporal lobe were detected bilaterally, but were more pronounced in the left hemisphere, in the inferior longitudinal and uncinate fasciculi. Regions with decreased NDI involved many regions of the brain, predominantly in the left hemisphere, except for brainstem and left hippocampus (Figure 3.1c).

HC vs R-TLE:

R-TLE patients (defined clinically and pre-operatively) showed (third column of Table 3.3) bilateral decreased FA in temporal, frontal and occipital lobes and diencephalon compared to HCs. Decreased AD affected the cerebellar peduncles and white matter bilaterally. Increased RD was mainly found in the right temporal and frontal lobes, plus the corpus callosum (Figure 3.2a).

Alterations in the right temporal lobe and bilaterally in the frontal lobe were revealed by decreased MK, while RK showed widespread decrease through the brain (Figure 3.2b).

Increased ODI was widespread in the brain, but no NDI alterations were detected (Figure 3.2c).

L-TLE vs R-TLE:

Compared to R-TLE patients, those with L-TLE presented (fourth column of Table 3.3) lower FA in the left temporal lobe, in the diencephalon and bilaterally along the corticospinal tracts. A higher MD was found in the left temporal lobe and rostrally along the superior longitudinal fasciculus, and bilaterally in the cerebellum. In addition, higher RD was found in the left

hemisphere, affecting both cerebrum and cerebellum, with particular involvement of the left corticospinal tract and superior longitudinal fasciculus (Figure 3.3A). Lower NDI was found ipsilateral to the pathology (Figure 3.3B).

R-TLE compared to L-TLE patients showed a lower AD in the left cerebellum.

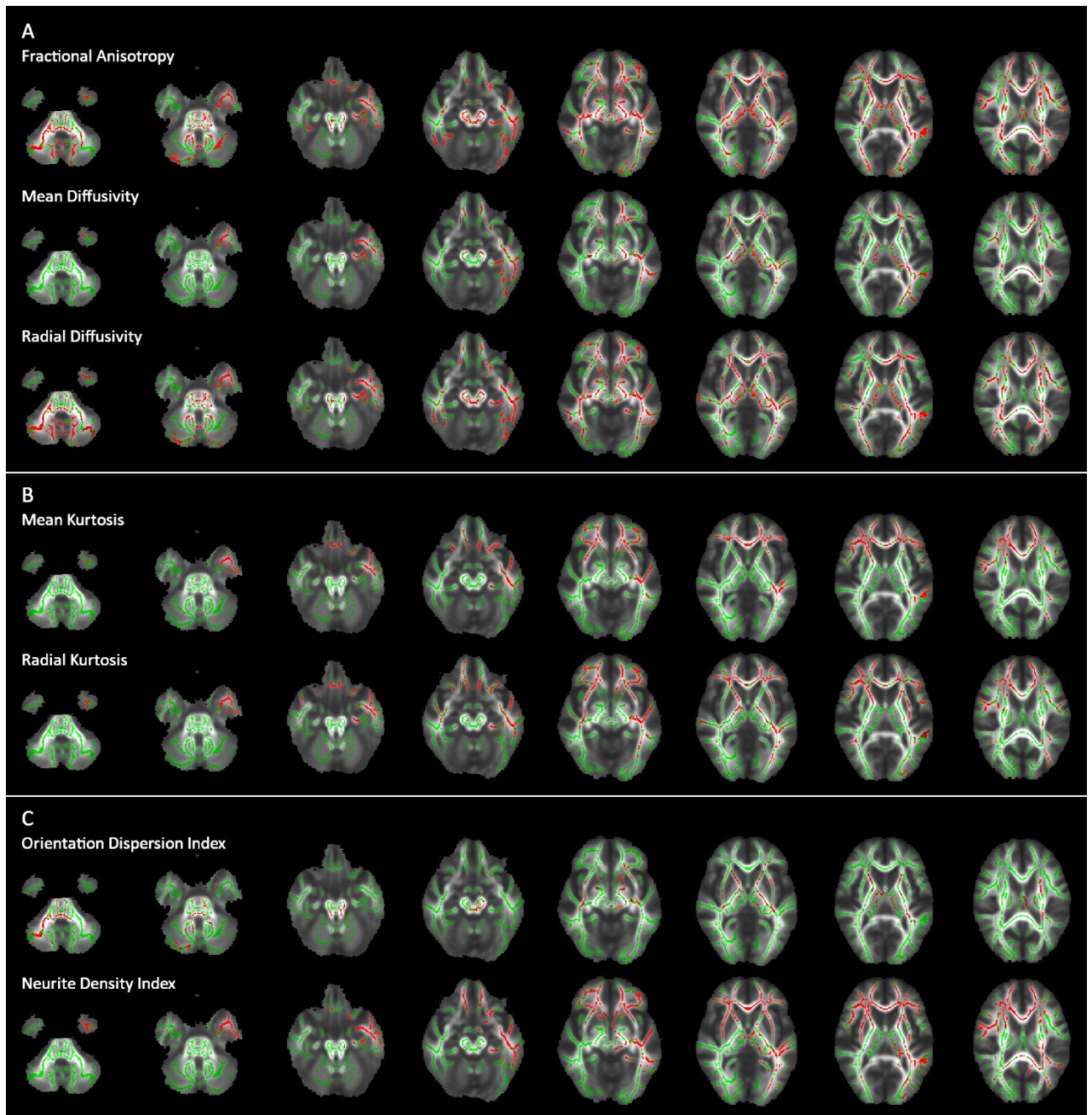


Figure 3.1: Alterations in left TLE patients (L-TLE) compared to healthy control from the TBSS analysis: (A) DTI, (B) DKI, (C) NODDI. L-TLE significantly different voxels are shown in red ( $p < 0.05$ ) overlaid on the mean white matter skeleton in green. Images are overlaid on the mean FA in MNI152 space, in axial radiological view.

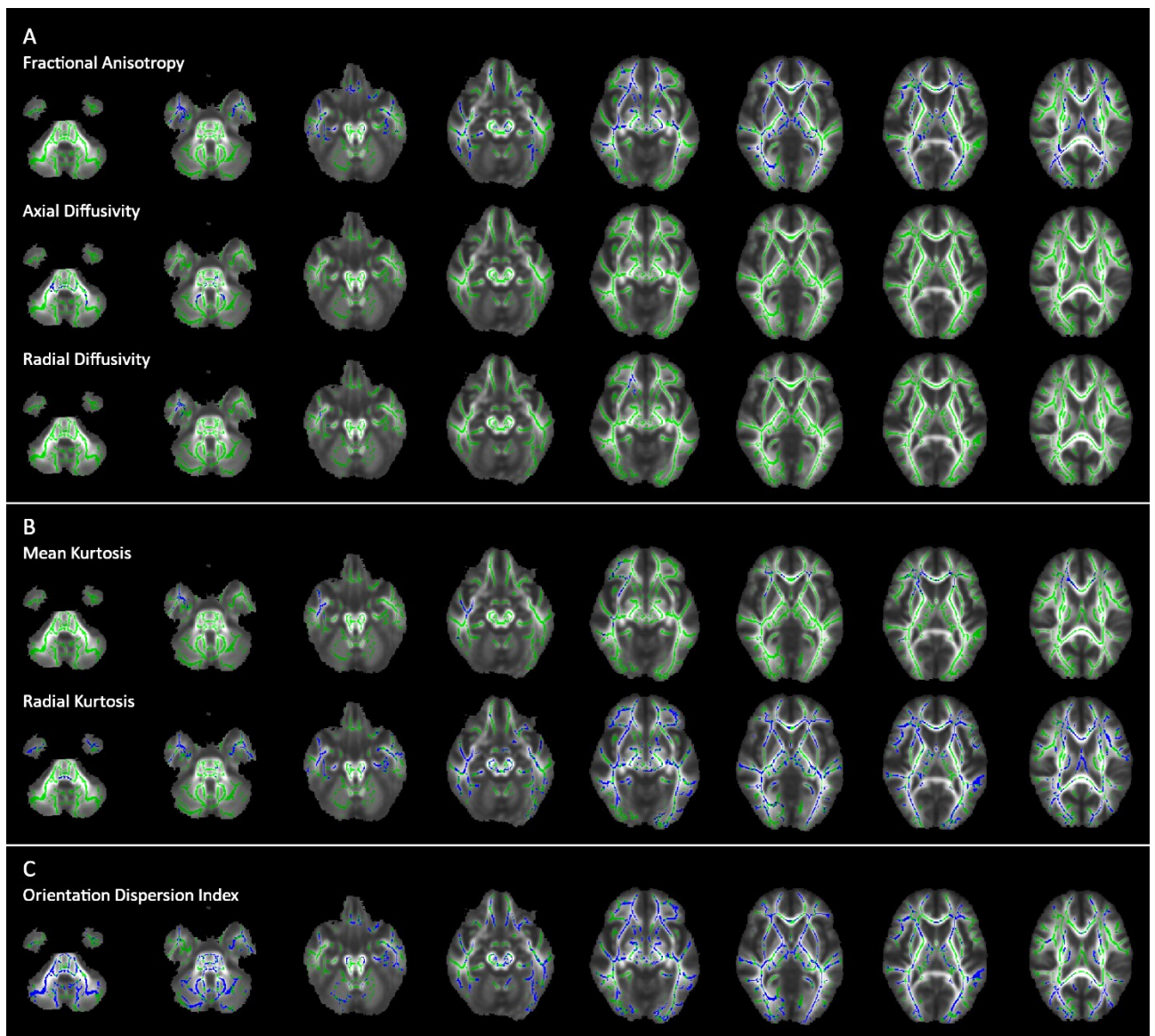


Figure 3.2: Alterations in right TLE patients (R-TLE) compared to healthy control from the TBSS analysis: (A) DTI, (B) DKI, (C) NODDI. R-TLE significantly different voxels are shown in blue ( $p < 0.05$ ) and the mean white matter skeleton in green. Images are overlaid on the mean FA in MNI152 space, in axial radiological view.

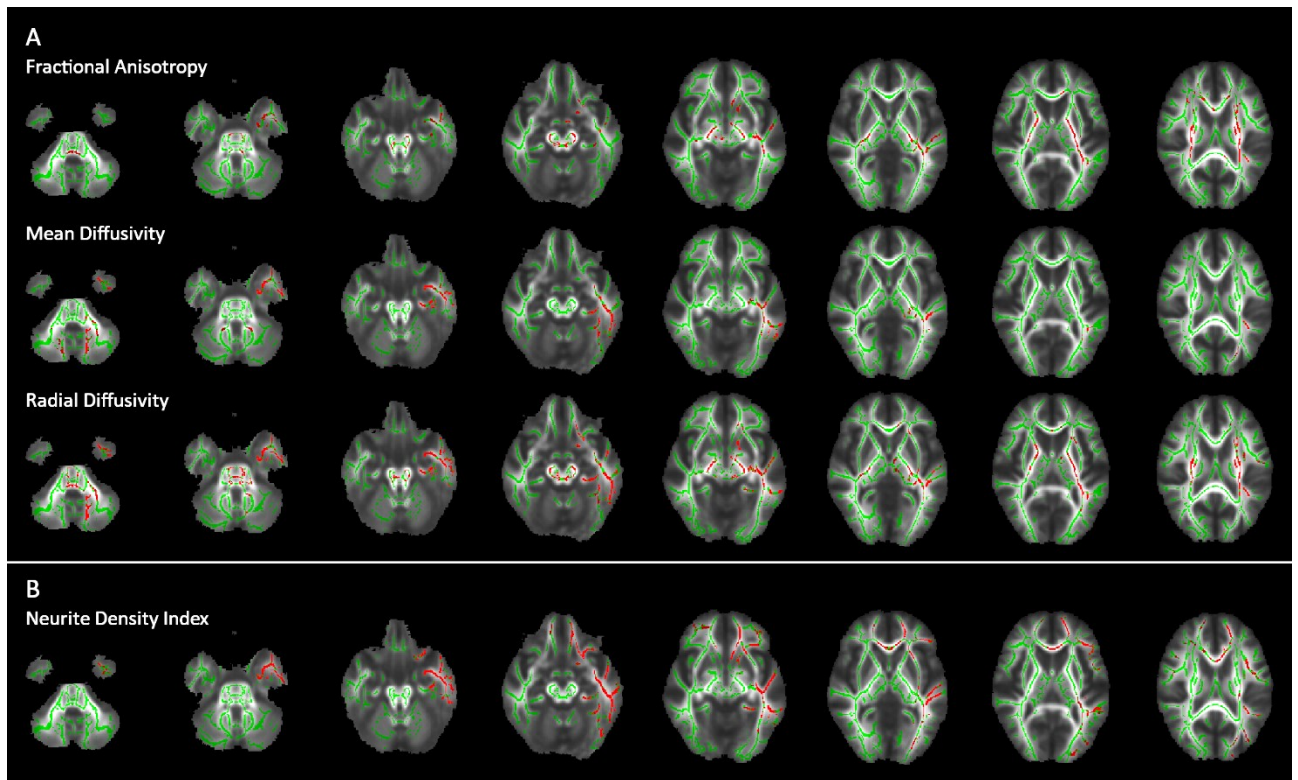


Figure 3: Alterations between L-TLE and R-TLE patient groups from the TBSS analysis: (A) DTI, (B) NODDI. L-TLE significantly different voxels are shown in red ( $p < 0.05$ ) and the mean white matter skeleton in green. Images are overlaid on the mean FA in MNI152 space, in axial radiological view.

## 3.4 Study II: Histological group analysis

### 3.4.1 Temporal lobe analysis - methods

Focal analysis of the left and right temporal lobe metrics was performed, given that these regions are considered most likely to be the source of TLE pathology. A mask of each temporal lobe was extracted from an atlas of the brain in MNI-space (Toro et al., 2009) and applied to the TBSS skeleton to identify white matter voxels belonging to the temporal lobes. Mean values of DTI, DKI and NODDI-derived metrics were then extracted for each subjects and statistically compared to assess microstructural alterations due to pathology. In addition, considering the differences that can occur among subject due to atrophy of the hippocampi, in order to minimise its influence in the analysis, the hippocampi were segmented from the volumetric (T1) scan using FIRST (FSL) and their volumes were calculated. Statistical tests were performed using SPSS21 (IBM, Armonk, New York). For all comparisons, two-sided  $p < 0.05$

was considered significant. Demographic, clinical, hippocampal volume and diffusion-derived parameters were tested for normality using a Shapiro-Wilk test. Age was compared between groups using a two-tailed Kruskal-Wallis test while gender was compared using a chi-squared test. A Mann Whitney U test was performed on clinical features (disease duration, age at onset and frequency of seizures) between groups of patients (L-TLE and R-TLE).

Statistical analysis was performed on the temporal lobe to compare metrics between specific groups as follows:

HC, R-TLE and L-TLE: Subjects were first grouped according to their pre-surgical clinical diagnosis, into HC, L-TLE and R-TLE groups in order to verify and quantify results described in the previous section 3.3.2. ANOVA was performed for hippocampal volume comparison between the three groups of subjects. A general linear model was then used to compare diffusion-derived metrics of the temporal lobe between pre-surgical defined groups, with age, gender, hippocampal volume (left volume for left temporal lobe analysis and right volume for right temporal lobe analysis), histopathological classification, and Engel classification (divided into completely seizure-free after surgery (Ia) and others (>Ia)) as covariates. Bonferroni correction was applied for multiple comparisons.

Histologic subgroups: Based on the pathology findings in the surgically treated patients, general linear models were built to compare diffusion-derived metrics of the temporal lobes between: 1) hippocampal sclerosis (HS) vs cryptogenic (Crypto) patients; 2) seizure-free vs other patients. A further sub-analysis was performed on the Crypto seizure-free patients vs other Crypto patients, as this was found to be the histological group with a higher proportion of not seizure-free.

## 3.4.2 Results

### HC, R-TLE and L-TLE:

Compared to HC, left hippocampal volume was lower in L-TLE patients, and right hippocampal volume was lower in R-TLE patients.

Figure 3.4A shows significant differences in DW metrics between groups. Comparison to the R-TLE group highlighted higher MD, AD and RD, along with lower ODI and NDI in the left temporal lobe of the L-TLE group.

No significant differences were found in Temporal lobe ROI when comparing HC to L-TLE or R-TLE.

Histological subgroup:

Compared to HCs, HS patients showed decreased FA and NDI, increased MD, AD and RD in the left temporal lobe, while Crypto patients showed only MD and RD reduction in the left temporal lobe (Figure 3.4B).

No differences were found either between seizure-free patients and not seizure-free, or between seizure-free patients with or without a Crypto classification.

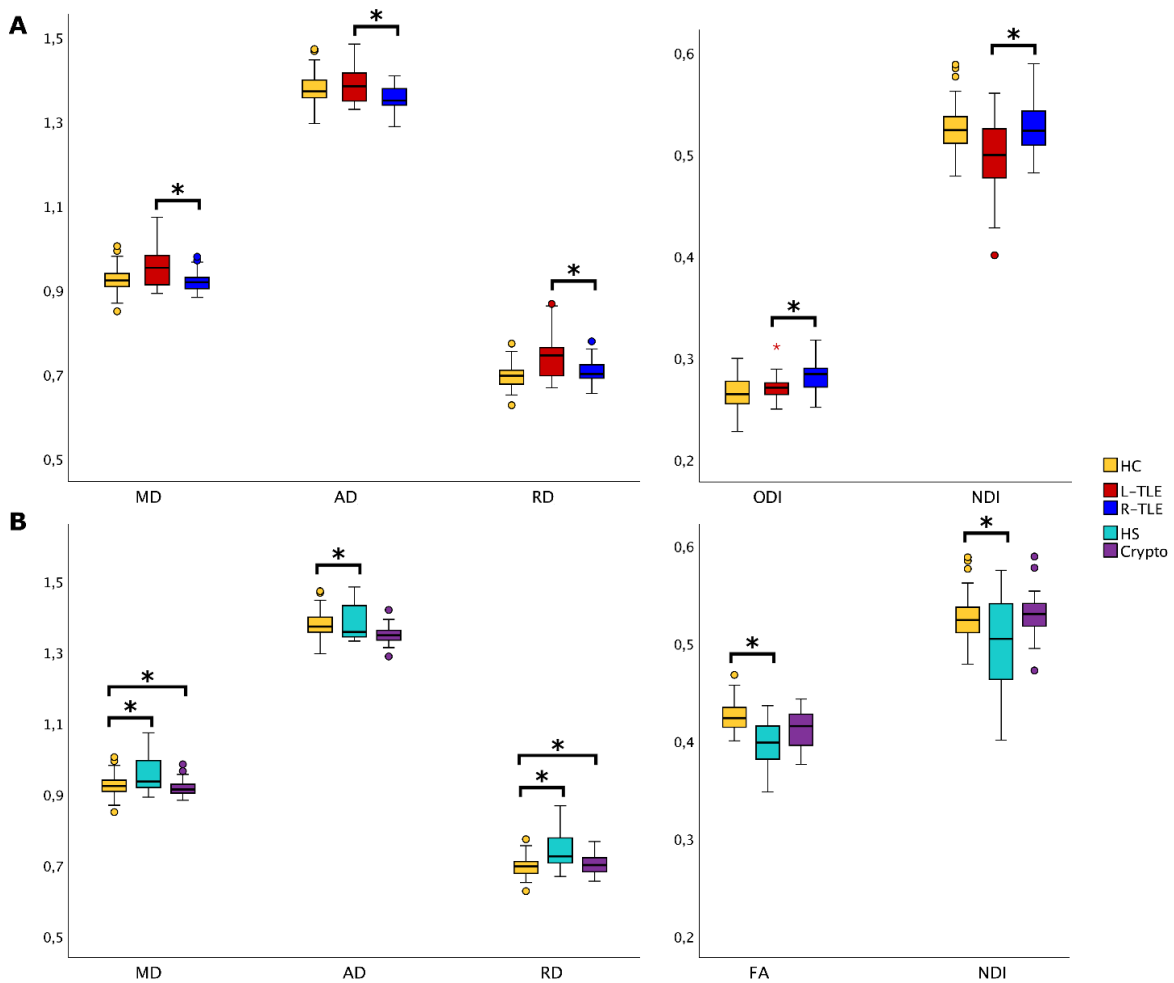


Figure 3.4: Boxplot of the DW-parameters in left temporal lobe ROI. Significant differences ( $p < 0.05$ ) between groups are marked with an asterisk. A) Boxplots in clinically defined groups. B) Boxplots in healthy controls and histologic groups.

HC: healthy controls; L-TLE: left TLE; R-TLE: right TLE; FA: Fractional Anisotropy; MD: Mean Diffusivity; AD: Axial Diffusivity; RD: Radial Diffusivity; ODI: Orientation Dispersion Index; NDI: Neurite Density Index.

## 3.6 Discussion

The present work provides a novel characterization of TLE pathology. The main finding is that clinically defined L-TLE and R-TLE present specific and not mirrored patterns of white matter microstructural alterations. This was seen in the analyses of both whole-brain and local temporal lobe WM properties. These patterns, present in clinically defined patient groups, could help support pre-surgical assessment even if histology may reveal a more heterogeneous aetiology.

### 3.6.1 Study I: Pre-surgery whole-brain analysis

Irrespective of side of localization, most diffusion-derived indices revealed alterations in TLE patients when compared with HCs. These widespread alterations represent a “mean effect” of the pathology, which are present in combination with the specific and focal alterations typical of left and right presentations, demonstrated by our further analyses. To avoid erroneous interpretations when using MRI to complement clinical assessment, it is therefore necessary separate different conditions that could reflect disease lateralization. Here we focused on investigating differences that occur according to the side of the epileptogenic zone.

In line with other studies (Li et al., 2014; Sanjari Moghaddam et al., 2019), our TBSS analysis revealed that the side of the epileptogenic zone determines consistent and specific microstructural changes. In particular, the present findings revealed that patients clinically classified as L-TLE involved a more extended network of bilateral alterations than R-TLE, as well as greater ipsilateral involvement, in both temporal and extratemporal areas (Xu et al., 2018). This is somewhat in contrast to a recent work (Buksakowska et al., 2019) that showed that R-TLE patients were characterised by more widespread involvement of WM and by a

---

significantly smaller right hippocampal volume than L-TLE patients, which could drive such alterations. A direct comparison with our result is difficult because in both cases the L-TLE and R-TLE classification was based on clinical assessments and not on surgical outcomes. While here we proceeded with assessing histopathological and Engel classifications, in the cited work authors did not report such results for the groups.

DTI and DKI demonstrated that L-TLE patients were characterized by an extensive and generalized alteration of WM bundles with respect to HC while NODDI-derived metrics showed more punctual and specific microstructural alterations that suggest they might be more sensitive in detecting primary WM alterations related to TLE pathology. In particular, in L-TLE all DTI and DKI metrics revealed several bilateral regions of abnormalities and only MD was specifically increased in the left hemisphere. Such microstructural alterations, particularly FA, were widespread through the brain. Nevertheless, it is to note that NDI and ODI alterations were spatially complementary to each other, and their total spatial distribution overlapped with all regions showing reduced FA suggesting that FA alterations were in fact due to different biological substrates in different brain regions. Indeed, reduced NDI was seen in previous works in both epilepsy (Winston et al., 2020) and other neurological diseases (Collorone et al., 2020; J. Zhang et al., 2018), where widespread WM alterations were associated with reduced axonal density in cerebral regions; while increased ODI in brainstem and right cerebellum might indicate a change in microstructure morphology rather than cellular density (Rossini et al., 2017). It would be interesting to run a longitudinal study to assess whether ODI changes precede NDI changes or whether these are stable and possibly linked to an underlying pathological malformation.

Conversely, R-TLE patients showed more focal and side specific alterations for all diffusion metrics compared to HC, suggesting a more localised pathology than in L-TLE (Xu et al., 2018). The most lateralized pattern was demonstrated by MK that was altered only in the right hemisphere, and only ODI showed widespread bilateral alterations. It is important to note that these results could be driven by the greater number of Crypto patients in the R-TLE group (Table 3.2), which are those with negative MRI and an unknown histopathological substrate, which could have hidden some significant alterations. Although differences were found when advanced DKI and NODDI metrics of L-TLE and R-TLE patients were compared to those of HCs,

these metrics did not reach statistical significance when comparing L-TLE and R-TLE directly against each other. DTI metrics, though, did reveal some differences, including lower FA globally and higher MD and RD in the left temporal lobe of L-TLE compared to R-TLE; these latter being consistent with the side of the most severe pathology.

Interestingly, a study with simultaneous EEG-fMRI (Fahoum et al., 2012) has detected widespread functional alterations with the involvement of the cerebellum in different types of focal epilepsy. This is supported by our results that show cerebellar involvement in L-TLE and R-TLE patients, though the two groups appear to present with different microstructure alterations according to advanced DW measures. Indeed, while MD and RD showed specific alterations in the cerebellum, mainly in the left hemisphere, we found lower AD in the left cerebellum in R-TLE with respect to L-TLE patients.

While acknowledging that there are argument against the specificity of RD and AD to myelin and axon integrity respectively (Wheeler-Kingshott & Cercignani, 2009), it would be interesting to assess whether the observed change in AD supports the hypothesis of a predominant morphological alterations of axons in terms of their mean axon diameter and myelination in R-TLE compared to L-TLE; this could then explain the increased ODI observed when comparing R-TLE to HC. Overall, these alterations are indicative of specific pathological changes of each subgroup of patients that could be used to develop clinical support systems for epilepsy diagnosis if confirmed in post-mortem studies (Ye et al., 2013).

The pathophysiological basis of these specific cerebellar changes needs to be investigated in post-mortem studies and confirmed by independent cohorts of similar patients' groups.

Overall, DTI and DKI metrics showed different patterns of alteration of WM across the brain between L-TLE and R-TLE with respect to HC. In general, we can assert that alterations are located mainly in the ipsilateral hemisphere of the epileptogenic zone and are more widespread in the L-TLE group. Moreover, NODDI provides good discriminative pathological metrics between L-TLE or R-TLE, with NDI alterations being found throughout the brain in L-TLE and ODI alteration in R-TLE. From a brain network point of view, it would be interesting to localise such changes in terms of short and long-range connectivity, given that from a visual

---

inspection of the results it seems that axonal bundles like the corpus callosum and inferior fronto-occipital fasciculus are particularly involved.

Differences in cerebral and cerebellar microstructural alterations in L-TLE and R-TLE could be justified by the fact that the brain is functionally lateralized and functional reorganization due to the pathology could be different. It is known that the left hemisphere is generally more associated with language and analytic functions, the right hemisphere is mainly associated with visuospatial and global functions, while the left hippocampus is involved in memory effect is, whereas navigation-related activity is prominent in the right hippocampus (Miller et al., 2018). Furthermore, it has been demonstrated that in L-TLE language lateralization is decreased, and this correlates with language deficits before and after temporal lobectomy (Rosazza et al., 2013). For these reasons we also investigated specifically the microstructural properties of temporal lobe white matter in histologically defined subgroups, as discussed below.

### 3.6.2 Study II: Histological group analysis

We performed targeted analysis of temporal lobe WM microstructure, integrating the information from histopathological specimens obtained at surgery and updated Engel classification (at least at 2 years from surgery) for all subjects included in the TBSS analysis, with the initial clinical classification. In addition to higher MD and RD, detected with the whole-brain TBSS analysis, we found that L-TLE patients presented lower ODI and NDI in the left temporal lobe compared to R-TLE patients. This confirms that clarifying the heterogeneous substrate of epilepsy helps to highlight differences between the L-TLE and R-TLE presentations. As this information can only be extracted from histological specimens, it is important to work towards “*in vivo* histology” biomarkers that could support clinical diagnosis for a better characterisation of epilepsy patients, eventually translating to a better patient management.

We also performed a histopathology-based group analysis to investigate microstructural abnormalities in relation to the underlying focal aetiology. Given the nature of the epilepsy presentations, and surgical specimens available, we focused the analysis on WM of the temporal lobes and compared microstructural metrics between HS and Crypto patient groups

as these were the most numerous in our cohort. Our analysis indicated that HS patients were characterised by microstructural white-matter alterations of the left temporal lobe, captured by all DTI metrics plus NDI. Crypto patients, instead, presented alterations only of MD and RD metrics from DTI. It may be possible to exploit these differences in microstructure metrics alterations as pre-surgical *in vivo* imaging indicators of disease aetiology. Moreover, considering that the majority of not complete seizure-free patients were Crypto, these differences could support the investigation of features linked to myelination and mean axon diameter, which if different between groups could help explain these findings (Rodríguez-Cruces & Concha, 2015).

Despite the fact that this cohort is very heterogeneous regarding age, disease duration, and histopathology, all patients shared a diagnosis of drug-refractory temporal lobe epilepsy; indeed, the majority of patients were successfully treated by temporal lobectomy (73% seizure-free, Engel Ia), with a significant portion of the remaining patients showing a consistent improvement (Table 5.2). This demonstrates that the epileptogenic area or the major cause of the pathology was confined within the resected temporal lobe area for the complete seizure-free patients. Considering that 27% of all patients were not completely seizure-free, of which 57% with cryptogenic epilepsy, it becomes evident the importance of finding biomarkers sensitive to the surgery outcome. Our region of interest (ROI) analysis of temporal lobe WM skeleton, did not yield such information, even when limited to Crypto patients. This negative result might be due to the small sample size of histologically consistent (e.g. HS or Crypto) seizure-free and not seizure-free patients or may indicate that for such search we should also extend our analysis to grey matter regions, where epileptogenic activity is located.

### 3.6.3 Limitation

The main limitation of this study is that patients were recruited based on clinical diagnosis and that histopathology revealed an heterogeneous cohort. Despite such heterogeneity, it is a clinically relevant population because it is based on clinical pre-operative details. Future studies could help to investigate further microstructure properties of tissue, including metrics sensitive to neuronal morphology and myelin that could help characterizing epilepsy

---

heterogeneity *in vivo* for a better pre-surgical patient management. Combining multiple parameters, with complementary information from clinical assessments, in a larger cohort of patients, using artificial intelligence approaches could provide a more comprehensive characterization of WM alteration. Moreover, larger studies of more homogeneous patients could help finding *in vivo* imaging biomarkers with predictive value of surgical outcomes. Finally, a further comment regards the possible neuropsychological implications that alterations beyond focal areas of seizures could have on patients response to surgery. It would be very interesting identifying metrics for assessing the microstructure parameters predicting the post-operative neuropsychological profile of individual patients. In order to understand the underlying physiological and pathological mechanisms of TLE, multimodal studies integrating imaging and data recording, e.g. from electroencephalography and functional imaging (PET and SPECT, MEG, EEG-fMRI), with cognitive and functional tests are needed. These will also improve the monitoring and prediction of the pathological course in patients.

### **3.7 Conclusion**

The present work revealed that there is significant and extended white matter alterations in epilepsy patients and that such alterations may depend on the lateralisation of the epileptic zone. In our cohort, L-TLE and R-TLE patients presented different patterns of alteration, characterized by specific microstructural changes involving different brain regions, including the cerebellum. Compared to HC, L-TLE patients were characterized by extensive and generalized alterations of WM bundles, while R-TLE patients showed more local WM alterations. The use of advanced microstructure metrics from DKI and NODDI, other than FA from DTI, can help discriminating WM alterations in subgroups of TLE pathology. Despite these alterations can identify specific patterns for L-TLE and R-TLE, almost all patients were seizure-free after surgery, which means that clinically relevant brain regions were localized near the epileptogenic zone. However, it remains to be determined whether such WM alterations beyond the resected area are going to influence recovery of specific functions. Overall, our study demonstrated that investigating WM alterations outside the temporal lobe is important as it might contribute to understand mechanisms underlying TLE and its etiopathogenesis.

## ***Chapter 4***

# **Tractography dissection of the human brain: challenges and perspectives**

## **4.1 Tractography**

Diffusion data are a precious way to investigate the morphology and health status of tissues, which subtends brain functionality. The necessity to investigate the structural connectivity of the WM is evident: damage to axonal connectivity results in being the substrate of different neurological and psychological pathologies.

The dependency of the diffusion-weighted image on the orientations of fibers in tissue can be used to reconstruct axonal tracts with post-processing methods that reconstruct streamlines representing WM structure and that are not identifiable with any other MRI technique. This 3D modeling technique is called tractography and it is at the basis of every modern study of neural network and structural connectivity. Streamlines represent an analogy of linear structures as fiber bundles. The globality of streamlines reconstructed, i.e. the tractography of the whole-brain, is called tractogram.

As part of my thesis I contributed to define what in my opinion was the best way to segment specific tracts and participated in an international effort to evaluate tractography reproducibility (Rolandi 2021 and Schilling 2021).

### **4.1.1 Diffusion tensor based tractography**

The simplest tractography approach is the one based on the diffusion tensor model (DT-tractography) which associates a diffusion ellipsoid to every voxel of an image. The assumption is that the principal axis of the diffusion ellipsoid is aligned with the axonal predominant direction in the voxel, obtaining a vectorial field that represents the local fiber

---

orientation. Thus, deterministic DT-tractography consists of a linear propagation algorithm that reconstructs the tridimensional trajectory bundle by propagating a line from a starting point, called seed, following the local vector orientation, until the termination criteria are met. A simple termination criterion is to set a lower anisotropy threshold (for example,  $FA=0.2$ ). The streamline propagation is terminated when it reaches a low anisotropy region, assuming that the edges of WM have been reached. Indeed, regions occupied by GM or CSF are characterized by a greater degree of isotropy.

### 4.1.2 Constrain Spherical Deconvolution based tractography

DT-tractography, however, results inadequate for tracking in voxels containing crossing-fibres ( $\geq 90\%$  of WM) delineating non-existent tracts (false positives), or not identifying existing tracts (false negatives) [Behrens T.E.J. et al, 2007]. To overcome this limitation, advanced acquisition (HARDI) and post-processing constrain spherical deconvolution (CSD and super-CSD) techniques have been introduced to improve tractography reconstructions. CSD provides fiber orientation distribution (FOD) that is robust to noise whilst preserving angular resolution and therefore improving the angular resolution of the results. Using CSD it is possible to better estimate fiber orientation and to resolve orientations that are separated by smaller angles than previously possible. Consequently, tractography algorithms based on CSD are able to track pathways running through crossing fiber regions (Tournier, 2007).

As stated in the previous section, a deterministic algorithm proceeds step by step, propagating the streamline along the local orientation more aligned to the current direction. The orientation is estimated from the fiber orientation distribution (FOD) by identifying the peaks and selecting from among these the one with the required orientation. However, this approach has a bias as the direction of the currently plotted peak locally merges, during propagation, with the direction of an adjacent peak. If this happens, the streamline undergoes a sudden deviation that if the constraint on the radius of curvature is too restrictive, it can lead to streamline termination. While early termination of the track can be avoided by allowing high angles of curvature between subsequent steps (default  $45^\circ$ ), this does not solve the underlying problem, which consists in the fact that the initially traced fiber population is

now merged with the locally dominant axonal population and is no longer followed individually.

Probabilistic tractography incorporates the concept of probability of a certain fiber direction into the tracking algorithm. Usually it tends to generate a large distribution of possible trajectories from each seed point. The chosen orientation for track propagation is drawn through random sampling of the FOD. This approach is trying to capture the dispersion of fibers within a voxel due to the underlying microstructure.

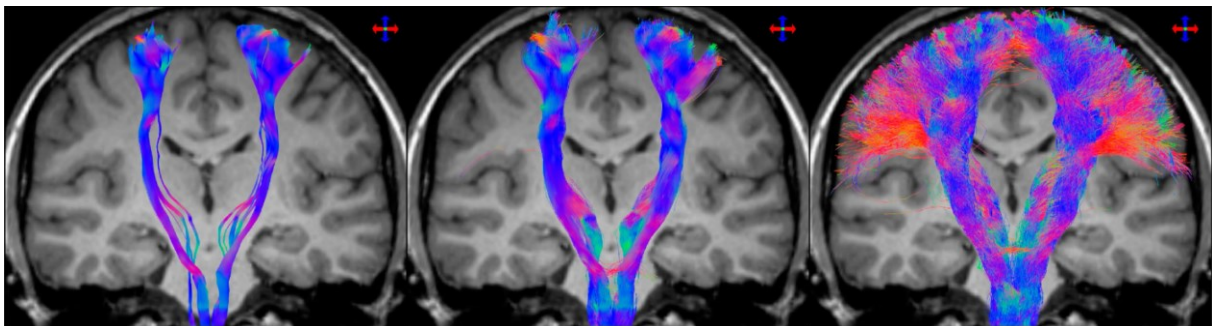


Figure 4.1: Cortico-spinal tract reconstructed with Diffusion Tensor based tractography (DT-tractography combined with a deterministic algorithm (left), DT-tractography combined with a probabilistic algorithm (middle), and constrained spherical deconvolution based tractography combined with a probabilistic algorithm (right). Reproduced from Calamante (2019).

## 4.2 Tractography dissection variability

The use of tractography for WM bundle segmentation has widely become the method of choice to identify WM fiber pathways *in vivo* in the human brain. However, considering the variability in bundle segmentation protocols and techniques, reconstructions of the same WM axonal pathways may provide different outcomes, directly affecting tractography results, quantification, and interpretation. Through an open call that involved 42 independent teams of researchers doing fiber tractography, Schilling K. et al (2021) aimed to evaluate and quantify the variability that arises from different protocols for bundle segmentation.

Six sets of whole-brain CSD-based tractograms (both deterministic and probabilistic) were provided to all collaborator teams, derived from 3 subjects with scan-rescan data acquired within the Human Connectome Project test-retest database (Glasser et al., 2016). Each

---

collaborator team could choose the tractogram to be used, between the two generated with the two commonly used tractography methods. Then, all teams were requested to send protocol details and results for bundle segmentation of 14 white matter bundles, which were chosen to represent a variety of white matter pathways commonly studied in literature: Superior Longitudinal Fasciculus (SLF), Arcuate Fasciculus (AF), Optic Radiation (OR), Corticospinal Tract (CST), Cingulum (CG), Uncinate Fasciculus (UF), Corpus Callosum (CC), Middle Longitudinal Fasciculus (MdLF), Inferior Fronto-Occipital Fasciculus (IFOF), Inferior Longitudinal Fasciculus (ILF), Fornix (FX), Anterior Commissure (AC), Posterior Commissure (PC), and Parieto-Occipital Pontine Tract (POPT).

## 4.3 Methods

### 4.3.1 Data

A total of three subjects (HCP IDs: 144226, 103818, 783462) that had scan-rescan diffusion MRI scans were chosen, resulting in six high-quality datasets, free of any significant artifacts. Collaborators were not informed that the six datasets represented only three subjects in order to not bias intra-protocol analysis. Distortion, motion correction and estimation of non-linear transformations to the MNI space were performed using the HCP pre-processing pipeline (Glasser et al., 2016). Whole-brain tractograms were generated using the DIPY-based Tractoflow processing pipeline (Theaud et al., 2020, Garyfallidis et al., 2014), producing both deterministic and probabilistic sets of streamlines to give to participants. Non-diffusion weighted ( $b_0$ ) images, Fractional Anisotropy (FA) maps (Jenkinson et al., 2012), directionally-encoded color maps (Jenkinson et al., 2012), T1 weighted images, and masks for the cerebrospinal fluid, gray matter, and WM (Jenkinson et al., 2012) were also provided.

For every team's submission, it was asked to send a definition of the selected WM bundles, a description of the pipeline to dissect these pathways, all code and/or temporary files in order to facilitate reproducibility of methods, and the streamline files of all segmented WM bundles.

### 4.3.2 Pathway-specific analysis

For all pathways, we focused on quantifying volume-based and streamline-based similarities and differences in the dissected bundles across protocols by assessing volume overlap and streamline overlap. Volume overlap was displayed as the volume of voxels in which 25%, 50%, and 75% of all protocols agreed that a given voxel was occupied by the pathway under investigation. Similarly, we viewed the individual streamlines in which 25%, 50%, and 75% of all protocols agreed that this streamline was representative of a given pathway. The results of these qualitative evaluations were shown as volume-renderings or streamlines visualizations directly.

Next, quantitative analysis was performed by assessing three voxel-based measures, either based on volume or streamline density, and one streamline-based measure (Rheault et al., 2020). The voxel-based measures are the Dice overlap coefficient, density correlation coefficient, and bundle adjacency, while the streamline-based one is the streamline Dice overlap (Figure 4). *Dice overlap* measures the overall volume similarity between two binarized bundles (i.e., all voxels that contain a streamline), by taking twice the intersection of two bundles divided by the union of both bundles. A value of 1 indicates perfect overlap, a value of 0 indicates no overlap. The *density correlation coefficient* is a measure of the Pearson's correlation coefficient obtained from the streamline density maps. This provides insight into not only overlap, but also agreement in streamline density. *Bundle adjacency* is a volume-based metric that describes the average distance of disagreement between two bundles. This was calculated by taking all non-overlapping voxels from one bundle, and calculating the nearest distance to the second bundle (and repeating from the second to the first bundle) and taking the average of these distances. By defining this metric, we are using a convenient symmetric distance between two binary volumes, which is a modification of the Hausdorff distance. For example, a value of 3 mm indicates that when the bundles disagree, they are an average of 3 mm apart. Finally, *streamline Dice* is the streamline-equivalent of Dice overlap. Streamline Dice was calculated by taking the total amount of streamlines common to both protocols (i.e., intersection) divided by the total number of unique streamlines in both bundles (i.e., union). Again, a value of 1 indicates that all streamlines are exactly the same, a value of

---

0 indicates no overlap in streamlines. Note that this final measure can be calculated only for datasets that are derived from the same original set of streamlines.

### 4.3.3 Bundle dissection variability across protocols

The measures introduced above were used to quantify variability across protocols (inter-protocol), variability within protocols (intra-protocol), and variability across subjects (inter-subject), with separate analyses for deterministic and probabilistic results. Below, we describe these three levels of variability assuming there were “N” submissions for a given pathway. For inter-protocol variability, each bundle was compared to its counterpart as produced by each of the other N-1 protocols, then all the results for each specific bundle were averaged for representing the average similarity/dissimilarity of that protocol with all others. This was done for all N submissions, for all 3 subjects, resulting in Nx3 data-points for each pathway. For intra-protocol variability, we aimed to compare the same protocol performed on the same subject. For each of the N submissions, we calculated the similarity/dissimilarity measures with respect to the same submission on the repeated scan. This was repeated for all subjects, resulting in again Nx3 data-points for each pathway. A “precise” measure of intra-protocol variability would have been possible if the same set of streamlines had been provided twice for each subject. Instead, the study used scan/re-scan data to measure not only intra-protocol variability, but the variability of everything up to, and including protocol. Thus, this measure includes acquisition variability (i.e., noise and possible artifacts), registration (to a common space), reconstruction, and generation of whole-brain streamlines. For inter-subject variability, we sought to characterize how similar/dissimilar a bundle is across subjects within a single protocol. All streamlines were normalized to MNI space using non-linear registration (antsRegistrationSyn) (Avants et al., 2008) of the T1 image to the MNI ICBM 152 asymmetric template (Fonov et al., 2011). For each of N protocols, the agreement measures were calculated from subject 1 to subject 2, from subject 2 to subject 3, and from subject 1 to subject 3, again resulting in Nx3 data-points for each pathway.

Finally, to visually assess differences across bundles and across protocols, we utilized the Uniform Manifold Approximate and Projection (UMAP) (McInnes and Healy, 2007) technique (<https://github.com/lmcinnes/umap>; release 0.4.1), which is particularly suited for visualizing

clusters or groups of high-dimensional data and their relative proximities. UMAP input was the 3D density maps of all bundles for all submission, while the output was projection of all bundles onto the 2D space. We note that any dimensionality reduction technique and subsequent visualization could have been used, for example t-SNE (Hinton and Roweis, 2002), for qualitative analysis of tractograms grouped across bundles and protocols. Hyperparameters and algorithm initialization are known to influence results for these nonlinear dimension reduction techniques (Kobak and Linderman, 2021), but for our purposes (qualitative visualization of local and global clusters without an explicit user-defined scalar measure of agreement/disagreement) we have implemented this with all default parameters of distances, metrics, and components.

## 4.4 Tract segmentation - my contribution

Here, it is uniquely reported the protocol adopted from our team, where the requested pathways were extracted following an anatomically based manual procedure starting from the probabilistic whole-brain tractogram (file: *Tracking-probabilistic.tck*). Specific regions of interest (ROIs) for each pathway were manually drawn on the T1 image in the MNI space (1 mm<sup>3</sup>). Each ROI was drawn as volume, consisting in consecutive 2D ROIs positioned on two or three sequential “slices”, except where otherwise specified, and was used to define inclusion (AND-ROIs and OR-ROIs) or exclusion (NOT-ROIs) regions for the selection of relevant streamlines. In addition to these ROIs, a grey matter-white matter (GM/WM) interface mask was used as an AND-ROI for the extraction of each tract in order to impose an anatomical constraint and to reduce the number of false positives. FNIRT (Smith 2010) registration was used to align subject’s T1 image to the MNI template and then the inverted registration was applied to all ROIs to warp them to each subject’s space.

Tract extraction from the whole-brain tractogram was performed using MRtrix3. The same software was also used to generate a color-coded track density image (TDI) based on the FOD principal direction of diffusivity from the whole-brain tractogram of each subject: the purpose of this map was to help the localization of relevant pathways and structures to visually assess the specificity of the selected streamlines. In detail, TDI maps were used to iteratively improve the final extraction of tracts: these maps were used to visually verify whether the tracts were

---

reconstructed as expected from literature, and in cases where improvement could be sought, TDI maps were used to help achieve a better positioning of the ROIs. This procedure was repeated until the extracted tracts were considered in line with literature descriptions of the investigated tract and homogeneous between all subjects.

The next paragraphs report the anatomical description of each dissected tract and ROIs positioning for bundle extraction. In Appendices are shown rendering of tracts with rgb color direction.

### 1. Superior Longitudinal Fasciculus (SLF)

From Galantucci S., et al. 2011:

"Five components have been described, which are likely to subservise. Three superior components consisting of anterior–posterior fibers connect the superior parietal lobule, the angular gyrus and the supramarginal gyrus to ipsilateral frontal and opercular areas. An inferior component consists of fibers that connect the superior and middle temporal gyri to ipsilateral frontal areas and is commonly called the arcuate fasciculus or SLF-IV. Finally, a fifth temporoparietal component (SLF-tp), connects the inferior parietal lobe with the posterior temporal lobe, and has been described in several previous studies although there remains some controversy about the nomenclature and the functional significance of this tract."

Three white matter AND-ROIs were drawn to reconstruct the SLF. From the rostral to caudal direction, two coronal AND-ROIs were placed in 1) the precentral gyrus and 2) posterior to the postcentral gyrus. Fibers oriented in the anterior-posterior direction and lateral to the cranio-caudally oriented white matter of the corona radiata were included in the AND-ROIs definition. A third axial AND-ROI was placed in the middle temporal gyrus, lateral to the fourth ventricle.

NOT-ROIs were placed in the medial sagittal plane, axial plane of the internal capsule, axial plane of the temporal stem and all the thalamus.

### 2. Arcuate Fasciculus (AF)

This is an association tract that is well-understood to connect Wernicke's area to Broca's area. Arch-shaped, it curves from the anterior-posterior direction in the frontoparietal cortex

ventrally into the temporal cortex (Catani and Mesulam, 2008). Because the AF is a dorsal longitudinal system of tracts, it is occasionally considered to be part of the SLF system of tracts (Dick and Tremblay, 2012, Thiebaut de Schotten et al., 2012) and considered synonymous or used interchangeably in the literature (Dick and Tremblay, 2012). For this controversial in definition, we considered it as a bundle of SLF and decided to not extract it as a bundle aside.

### 3. Optic Radiation (OR)

From Sure et al:

“The optic tract terminates in the lateral geniculate body, which contains six cellular layers. Most of the optic tract fibers end here, forming synapses with lateral geniculate neurons. These, in turn, emit fibers that run in the hindmost portion of the internal capsule and then form a broad band that courses around the temporal and occipital horns of the lateral ventricle, the so-called optic radiation. The fibers of the optic radiation terminate in the visual cortex, which is located on the medial surface of the occipital lobe, within, above, and below the calcarine fissure.”

Two white matter AND-ROIs were drawn to reconstruct the OR. The first AND-ROI was defined as the combination of a coronal caudal square and a sagittal medial square with respect to the lateral geniculate nucleus. A second coronal AND-ROI was placed in the occipital lobe.

NOT-ROIs were placed in the medial sagittal plane, coronal plane between hippocampus and amygdala covering the temporal lobe, axial plane of the temporal stem and the thalamus.

### 4. Corticospinal Tract (CST)

From Sure et al:

“They cross farther down (usually at the level of the segment that they supply) through the anterior commissure of the spinal cord. At cervical and thoracic levels, there are probably also a few fibers that remain uncrossed and innervate ipsilateral motor neurons in the anterior horn, so that the nuchal and truncal musculature receives a bilateral cortical innervation. The majority of pyramidal tract fibers cross in the temporal stem decussation of the pyramids, then descend the spinal cord in the contralateral lateral funiculus as the lateral corticospinal

---

tract. This tract shrinks in cross-sectional area as it travels down the cord, because some of its fibers terminate in each segment along the way.”

Three white matter AND-ROIs were drawn to reconstruct the CST. From the ventral to dorsal direction, two axial AND-ROIs, identified with the blue color on the TDI map hence indicating fibers aligned with the superior-inferior direction, were placed in 1) the caudal part of the pons and 2) the internal capsule. A third AND-ROI was placed to cover white matter voxels included in the precentral gyrus.

A NOT-ROI was placed in the medial sagittal plane.

### 5. Cingulum (CG)

From Yupeng Wu et al., 2016:

“The cingulum bundle (CB) is a 5–7 mm in diameter fiber bundle that is located above the CC and under the cingulate cortex (Schmahmann and Pandya, 2006). It originates within the white matter of the temporal pole, runs posterior and superior into the parietal lobe, then turns, forming a “ring-like belt” around the CC, into the frontal lobe, terminates anterior and inferior to the genu of the CC in the orbital-frontal cortex (Agrawal et al., 2011).”

Three AND-ROIs were drawn to extract all the five subcomponents of the cingulum. Each AND-ROI was composed of 2 OR-ROIs, one oriented in the coronal plane and placed dorsally to the central section of the CC, and one oriented axially and placed along the hippocampal portion of the CG.

NOT-ROIs were placed in the medial sagittal plane, axial plane of the internal capsule, axial plane of the temporal stem and the thalamus.

### 6. Uncinate fasciculus (UF)

From B. Leng et al., 2016:

“The uncinate fasciculus (UF) is a hook-shaped long-range association tract that provides a reciprocal corticocortical link between the frontal and temporal lobes. It passes through the temporal stem and connects the anterior part of the temporal lobe with the orbitofrontal cortex and the polar frontal cortex”

An AND-ROI was positioned in the coronal plane, at the height of the genu of the CC, covering the inferior part of the frontal lobe. A second AND-ROI was positioned axially in proximity to the temporal stem in order to cover all the temporal pole.

NOT-ROIs were placed in the medial sagittal plane and medial coronal plane.

#### 7. Corpus Callosum (CC)

The CC is the largest, and arguably most easily recognizable, WM structure of the brain. This structure is not a single tract but rather a commissure, composed of axons coursing in the left-right orientation at the midline, and interconnecting the cerebral cortex of the two hemispheres. Considering the high number of different subdivisions of the CC that have been proposed (Hofer and Frahm, 2006), we decided to not extract CC as a single bundle neither performed an extraction of its possible sub-bundles.

#### 8. Middle Longitudinal Fasciculus (MLF)

From Makris N., et al., 2008:

“...is located within the superior temporal gyrus coursing from the temporal pole to the caudal end of STG and extends further dorsally and caudally inside the inferior parietal lobule...”

Three coronal AND-ROIs that included white matter of the superior temporal gyrus were drawn to reconstruct the MLF, as previously described by Makris et al., 2008. From the rostral to caudal direction, the first AND-ROI was placed in the temporal lobe posterior to the frontotemporal transition, near the insula. The second AND-ROI was constituted of 10 contiguous coronal slices posterior to the first AND-ROI, and the third AND-ROI was constituted of 10 contiguous coronal slices posterior to the second one.

NOT-ROIs were placed in the medial sagittal plane, first AND-ROI of the SLF, axial plane of the internal capsule and axial plane of the retrolenticular part of the internal capsule.

#### 9. Inferior Fronto-occipital Fasciculus (IFOF)

From Catani et al., 2008

“...is a ventral associative bundle that connects the ventral occipital lobe and the orbitofrontal cortex. In his occipital course the inferior fronto-occipital fasciculus runs parallel to the inferior

---

longitudinal fasciculus. On approaching the anterior temporal lobe, the fibers of the inferior fronto-occipital fasciculus gather together and enter the external capsule dorsally to the fibers of the uncinate fasciculus.”

Three AND-ROIs were used to dissect the IFOF. The first AND-ROI was drawn in the ventral white matter of the occipital lobe on 14 contiguous axial slices. The inferior edge was defined as the slice containing white matter voxels of the lingual and fusiform gyrus, while the anterior border was selected posteriorly to the cingulum. The second axial AND-ROI was defined around the external capsule, while the third AND-ROI was placed coronally in the frontal orbital cortex.

NOT-ROIs were placed in the medial sagittal plane, coronal plane transversally to the middle part of the CG, axial plane in correspondence to the hippocampal portion of the CG and axial and coronal planes to delimitate the thalamus.

#### 10. Inferior longitudinal Fasciculus (ILF)

From Catani et al., 2008 and Galantucci et al , 2011:

“...is a ventral associative bundle with long and short fibers connecting the occipital and temporal lobes. The long fibers are medial to the short fibers and connect visual areas to the amygdala and hippocampus.”

Two AND-ROIs were used to reconstruct the ILF. The first coronal AND-ROI (Galantucci) was defined to include temporal white matter rostral to the anterior surface of the cerebral peduncles. The second axial AND-ROI (Catani) was defined in the occipital lobe, as previously described for the first AND-ROI of the IFOF.

NOT-ROIs were placed in the medial sagittal plane, first AND-ROI of the SLF, axial plane of the internal capsule, axial plane of the retrolenticular part of the internal capsule and axial and coronal planes to delimitate the thalamus.

#### 11. Fornix (FX)

From Sung H. J., 2017:

“The fornix is one of the principal fiber tracts providing the major afferent and efferent

systems of the hippocampal formation. The precommissural fornix is mainly connected to the cholinergic nuclei in the basal forebrain and septal region from the hippocampal formation, the postcommissural fornix, on the other hand, is mainly concerned with transfer of information on episodic memory between the hippocampal formation and mammillary body”

Three AND-ROIs were drawn starting from the left hippocampus and moving towards the mammillary bodies. The first AND-ROI was placed in the axial plane, in correspondence of the most caudal part of the crux of the FX, before entering the hippocampi. The second AND-ROI was identified by the intersection of two planes (axial and coronal) located at the level of the splenium of the CC. The third AND-ROI was placed in the axial plane transversally to the direction of the FX and before the bifurcation where the FX divides itself into two columns that lead to the mammillary bodies.

NOT-ROIs were located in the medial sagittal plane covering the CC and extending to include the section of the CG above it as well as the section between the genu and the optic chiasm; axial plane in correspondence of the hippocampal portion of the CG; Sagittal plane on the AC and externally to the left columns of the FX; Coronal plane between hippocampus and amygdala.

#### 12. Anterior Commissure (AC)

From Güngör, A., et al., 2017:

“The anterior commissure consists of a body, anterior and posterior crura, and the occipital and temporal extensions of the posterior crus. The body of the anterior commissure crosses the midline in the anterior wall of the third ventricle and bifurcates into anterior and posterior crura. The anterior crus passes forward to the medial orbitofrontal area and the posterior crus runs superolaterally to reach the temporal lobe, where it gives extensions to the temporal pole and occipital lobe. The occipital extension merges into the sagittal stratum after passing deep to the inferior limiting sulcus. The anterior crus passes forward below the frontal horn. The temporal extension passes anterior to the temporal horn and the occipital extension runs lateral to the inferior two-thirds of the atrium.”

Three AND-ROIs were drawn to extract the AC: the first one was placed sagittally in correspondence of the brain midline, where the AC is easier identifiable on the TDI map; the

---

other two were placed symmetrically in correspondence of the AC, externally to the columns of the FX.

NOT-ROIs were located in the medial sagittal plane, avoiding to include the midline AND-ROI described above.

### 13. Posterior Commissure (PC)

From N. G. Ozdemir, 2015:

“... the posterior commissure is located in the posterior part of the third ventricle, composing the roof, floor, posterior wall, and both lateral walls.”

Three AND-ROIs were drawn to select the PC tract, all in the sagittal plane: the first one in correspondence to the PC and the brain midline; the other two were placed symmetrically in correspondence to the PC and externally to the spinothalamic tract.

One single NOT-ROI was located in the sagittal plane in correspondence of the brain midline covering the full FOV, ensuring to avoid the midline AND-ROI described above.

### 14. Parieto-Occipital Pontine Tract (POPT)

Considering the impossibility to find a clear definition of the “Parieto-Occipital Pontine Tract” we excluded it from our bundles extraction.

## **4.5 Results**

Fiftyseven sets of protocols were submitted, of which 28 submissions used the deterministic streamlines and 29 used probabilistic ones. A total of 3138 bundle tractograms were submitted. Because collaborators did not have to submit all the 14 described bundles, dissected pathways showed varying representations across submissions ranging from as low as 16 protocols for the PC, up to 50 protocols for the CST (Figure 4.2).

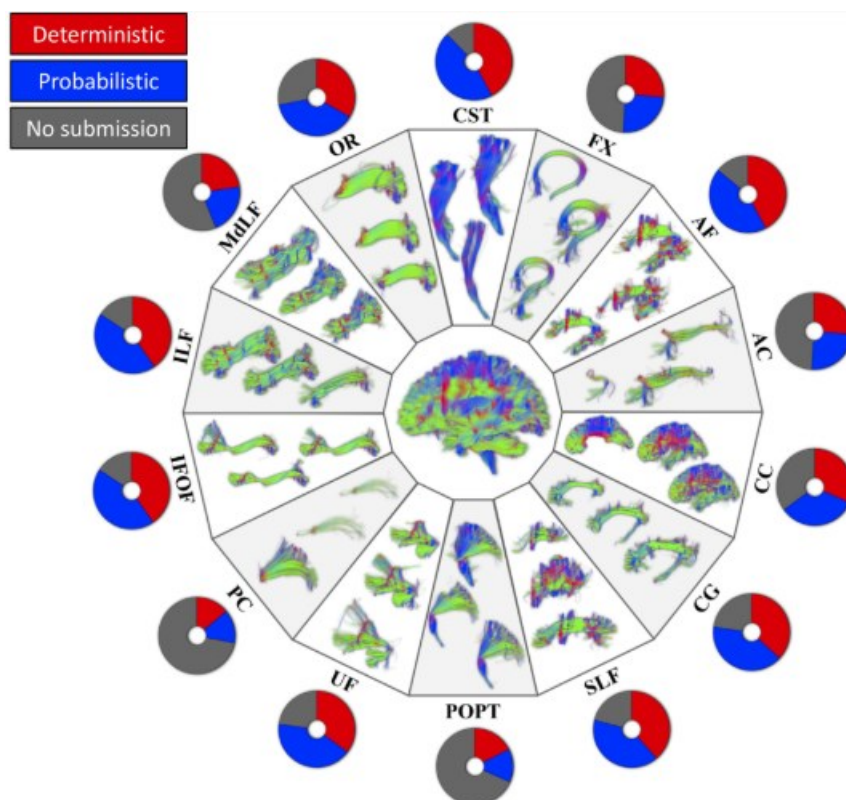


Figure 4.2: Summary of submissions. In total, 42 teams submitted 57 sets of bundle dissections, of which 28 utilized the provided deterministic streamlines, while 29 utilized probabilistic ones. Map icons are colored based on the set of streamlines utilized (deterministic=red, probabilistic=blue, no submitted=gray). Example submissions are shown for 14 pathways (bottom) along with a pie chart indicating the number of submissions for each bundle. Reproduced from Schilling et al (2021)

### 4.5.1 Qualitative results

Example visualizations of a segmentation from a single subject, randomly selected from those submitted by the various teams, are shown for exemplar projection, association, and commissural pathways (CST, AF, CC) in Figure 4.3. All these tracts are visualized both as streamlines (top of each row) and also as 3D streamline density maps (bottom of each row). The first observation that we can make looking at this figure is that there are many ways to segment the same white matter pathway resulting in qualitatively different representations. These examples clearly demonstrate variations in size, shape, and connectivity patterns of selected streamlines. In contrast, different protocols result in similar patterns of high streamline density in white matter with the most aligned axonal bundles and midbrain, with similar overall shape and central location. These observations apply to all dissected pathways,

---

however the commissural AC and PC contained very few streamlines, with little-to-no agreement across protocols.

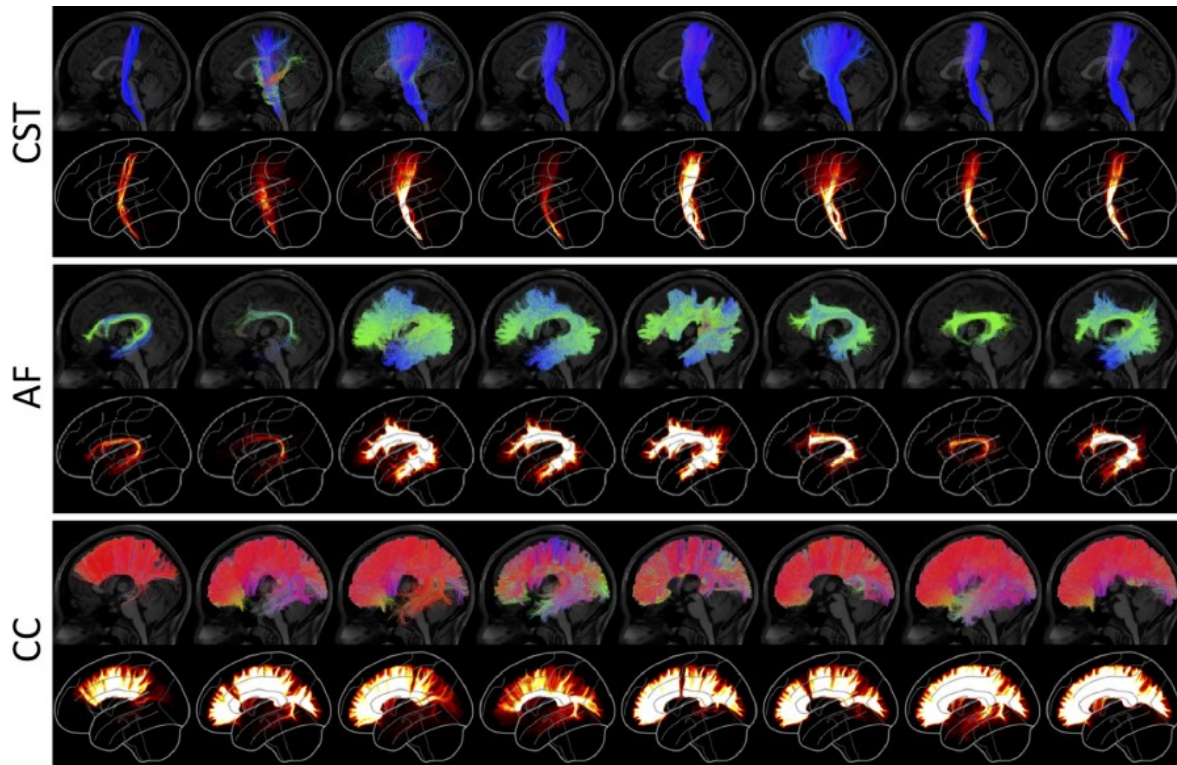


Figure 4.3: Variation in protocols for bundle segmentation of example pathways (CST, AF, and CC) on the same subject from the same set of whole-brain probabilistic streamlines. Eight randomly selected bundle segmentation approaches for each pathway are shown as segmented streamlines and rendered as 3D streamline density maps. Variations in size, shape, density, and connectivity are qualitatively apparent. Random selections generated independently for each pathway. Streamlines are colored by orientation and all density maps are windowed to the same range where the brightest color represents the highest streamline density (from K.G. Schilling, F. Rheault, L. Petit et al 2021).

## 4.5.2 Pathway-specific results

To understand the variability that exists across protocols for a given pathway, we assessed volume-based and streamline-based overlaps between the protocols and obtained boxplots of agreement measures that quantify inter-protocol, intra-protocol, and inter-subject variation. The volume overlap is displayed as the volume of voxels in which a given percent of protocols agree that the voxel was occupied by a given pathway, while the streamline overlap is displayed as the individual streamlines in which a given percent of protocols agree that the specific streamline is representative of a given pathway. For quantitative analysis, we used

several measures to describe similarity and dissimilarity of streamlines, streamline density, and pathway volume (Figure 4). In details, four indexes were calculated (1) volume Dice overlap that describes the overall volume similarity, (2) density correlation that describes insight into similarity of streamline density, (3) bundle adjacency that describes the average distance of disagreement between two bundles, and (4) streamline Dice that describes the overlap of streamlines common between protocols (which can only be calculated because bundles come from the same original set of streamlines).

We calculated geometric measures of pathways including number of streamlines, mean length, and volume, as well as microstructural average measures of the entire pathway volume, such as mean fractional anisotropy (FA) and mean FA weighted by streamline density (wFA). For simplicity, we show results of the CST, AF, and CC.

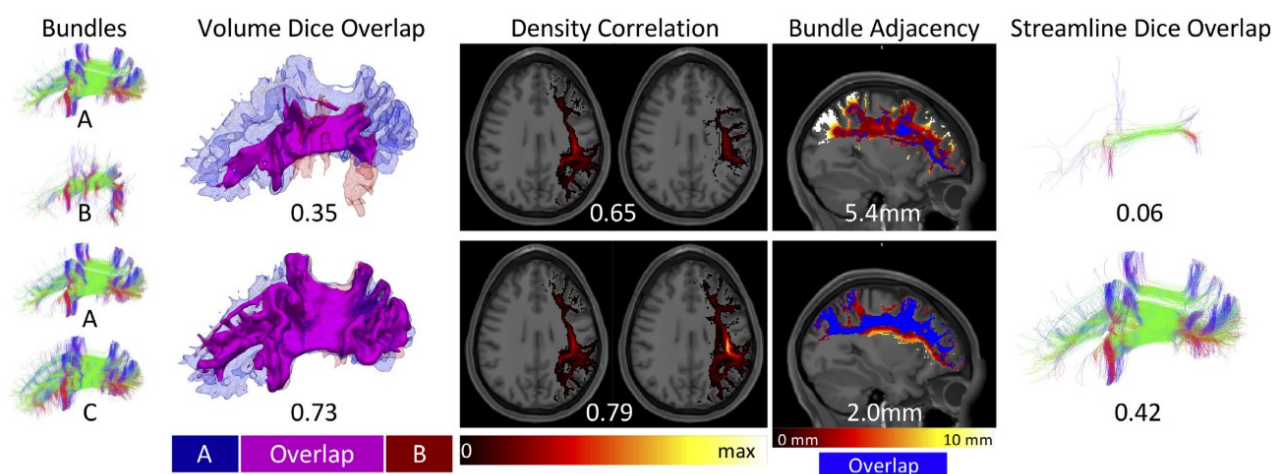


Figure 4.4: Similarity and dissimilarity metrics to assess reproducibility. SLF datasets are used as an example to illustrate a range of similarity values between bundles A and B (top) and between bundles A and C (bottom). Dice overlap is a volume-based measure calculated as twice the intersection of two bundles (magenta) divided by the union (red and blue). Density correlation is calculated as the correlation coefficient between the voxel-wise streamline densities (shown as a hot-cold colormap ranging from 0 to maximum streamline density) of the two bundles being compared. Bundle adjacency is calculated by taking the average distance of disagreement (not including overlapping voxels in blue) between bundles (distances shown as hot-cold colormap). Finally, streamline Dice is taken as the intersection of common streamlines divided by the union of all streamlines in a bundle and requires input bundles to be segmented from the same set of underlying streamlines (intersection shown in figure). Reproduced from Schilling et al (2021).

---

### 4.5.3 Inter-protocol variability

To understand which pathways exhibit the most agreement/disagreement across protocols, intra-protocol volume-based variation measures of Dice overlap, density correlation, bundle adjacency, and Dice streamlines are plotted in Figure 4.5.

There is a fairly large variation across pathways in the overall protocol agreement as measured by Dice volume overlap (Figure 4.5A). Volume-wise, the most reproducible tracts were the CC, the CST, and the IFOF. Reproducible results from the CC were expected due to its large size and unambiguous location of the CC proper, while the CST is arguably one of the most well-studied tracts. The IFOF, while one of the more controversial fasciculi (Forkel et al., 2014 , Mandonnet et al., 2018 , Altieri et al., 2019 , Sarubbo et al., 2019), likely results in higher overlap because it is a long anterior-posterior directed pathway spanning from the occipital to frontal lobe, passing through the temporal stem, a tight and small bottleneck region (Hau et al., 2016) and most protocols agree that nearly any streamline spanning this extent through a ventral route, will belong to this pathway. In all cases, the overlap across protocols is fairly low, with median values of the CC of 0.66, and 0.72 being the highest among all studied pathways. The least reproducible structures are those of the commissures, AC and PC, which are largely defined only by a single location along the midline with very little information on their routes or connections. The FX represented a unique case. Many groups submitted the left FX as expected, while others considered the left and right FX as a single structure due to its commissural component. Thus, while it is indeed a small structure, the quantitative value of overlap is overly critical based on qualitative observations.

In agreement with qualitative results, the density correlations (Figure 4.5B) are moderate to high for most pathways, meaning that areas of high streamline density and low streamline density are generally in agreement across protocols. Pathways such as the CC, IFOF, CG, CST, and UF have high agreement in streamline densities, whereas pathways with generally lower number of streamlines and hence lower densities (i.e., PC, and FX) show lower density correlations.

Similar results are observed for dissimilarity (Figure 4.5C). Again, commissural tracts (AC and PC) show very large distances of disagreement, along with the FX and in this case the MdLF.

For nearly all pathways, the range of disagreement across protocols is typically on the order of 4-6 mm. Looking at Dice overlap of the streamlines (Figure 4.5D), it is immediately visible that the overlap is very low in all cases, much lower than overlap of volume. For all pathways, a large majority of all comparisons yield streamline Dice coefficients less than 0.2, with many indicating no overlap at all. A trend observed in the streamline comparisons is that the overlap is generally greater for deterministic than probabilistic algorithms.

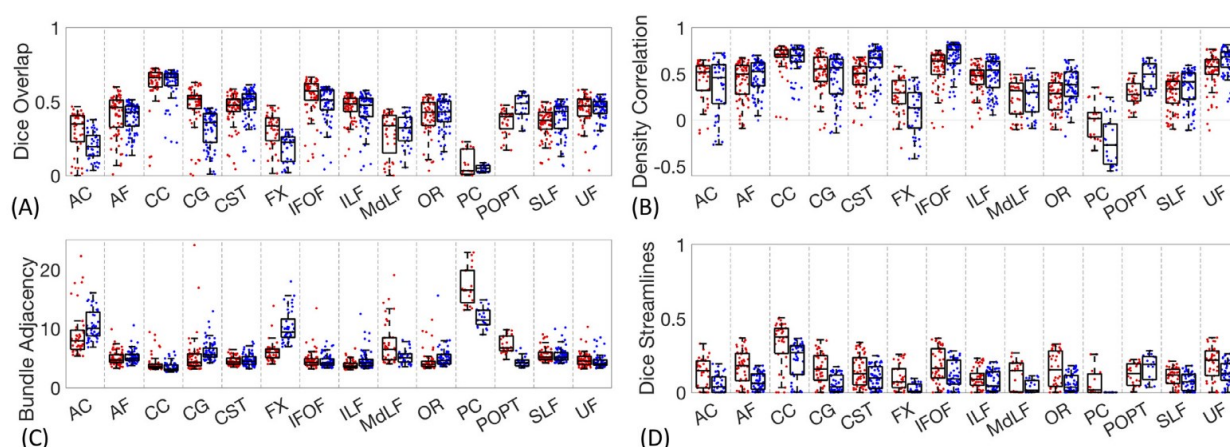


Figure 4.5: Inter-protocol variability. Dice overlap coefficients (A), density correlation (B), bundle adjacency (C), and Dice streamlines (D) for all studied pathways. Deterministic results are shown in red, while probabilistic in blue. Reproduced from Schilling et al (2021).

Figure 4.6 shows protocol variability for pathway-specific measures of mean FA, wFA, pathway volume, and pathway length across all protocols. In agreement with results on the CST, AF, and CC, the FA derived from different protocols varies by more than 8-12%, demonstrating an effect greater than that observed in the literature across study cohorts (Landman et al., 2011, Farrell et al., 2007, Landman et al., 2007). However, wFA varies much less across protocols (4-7%) and is of greater overall magnitude than the unweighted metric. The volume measurements show that different protocols can result in an order of magnitude difference in pathway volume, an effect observed for all pathways. Finally, pathways with more variation in average streamline length agree well with those with more variation in overlap measures. For example, AC, PC, and FX result in large differences in average length, while protocols on the IFOF consistently agree on the length of this structure.

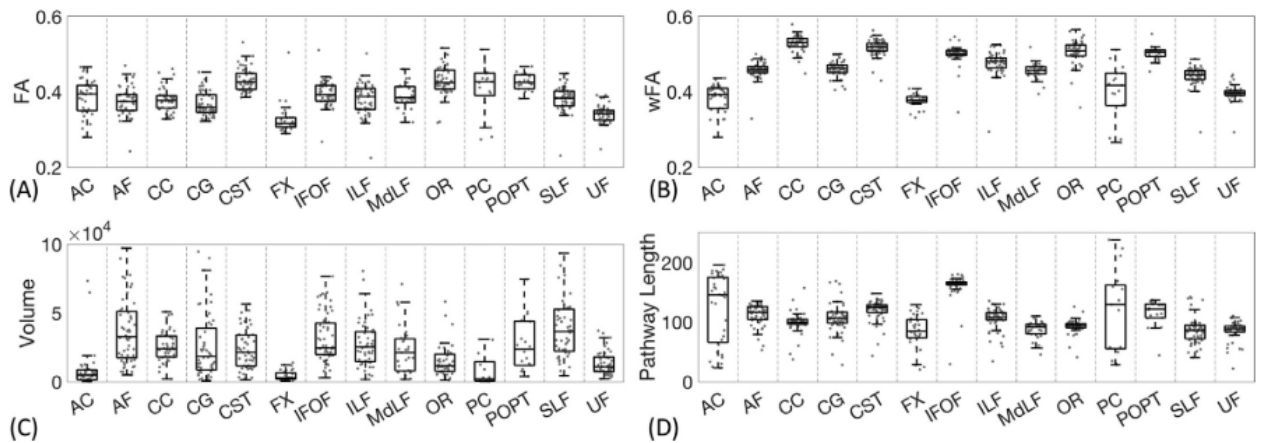


Figure 4.6: Inter-protocol variation in mean FA, weighted-FA, volume ( $\text{mm}^3$ ), and pathway length (mm) for all studied pathways. Note that CC volume is an order of magnitude larger than all other pathways and is shown on a  $10^3 \text{ mm}^3$  scale. Reproduced from Schilling et al (2021).

#### 4.5.4 Variability within and across pathways

To assess similarity and differences in submissions without a priori user-defined metrics of similarity, we utilized the Uniform Manifold Approximate and Projection (UMAP) (McInnes and Healy, 2007) technique to visualize all bundle segmentation techniques in a low-dimensional space. The UMAP is a general nonlinear dimensionality reduction method that is particularly well suited for visualizing high-dimensional datasets, in this case, on a 2D plane. Figure 4.7 shows all submissions, for all pathways, projected on a 2D plane (top left panel). While there are differences across protocols for a given pathway, all submissions for a given pathway generally cluster together and show similar low-order commonalities, for both probabilistic and deterministic approaches. However, overlap between different pathways does occur in some instances, for example between the SLF and AF (Figure 4.7A), POPT and CST (Figure 4.7B), and MLF, ILF, and OR (Figure 4.7C). This suggests similar low-order representation of some submissions in these pathways.

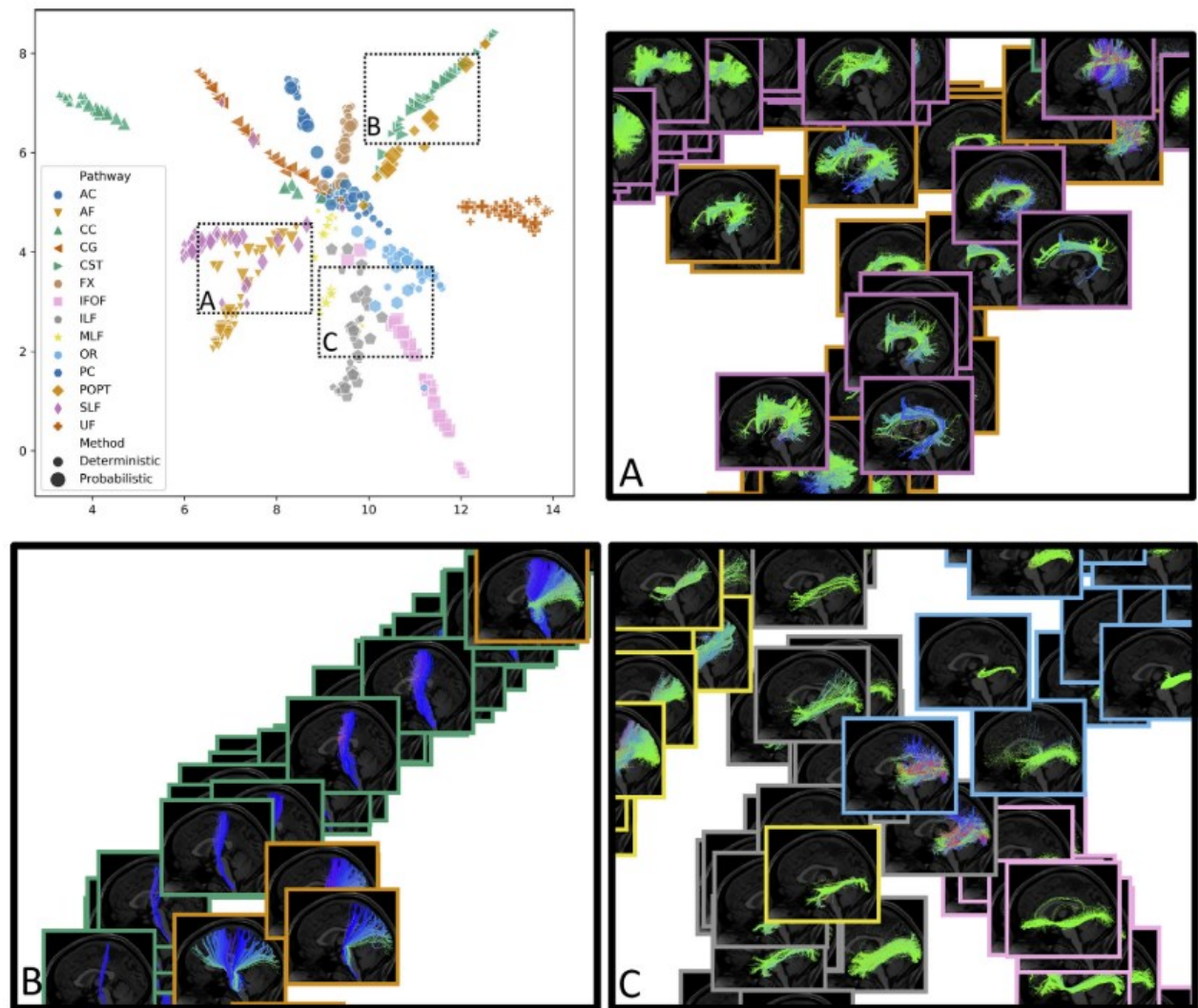


Figure 4.7: UMAP dimensionality reduction projected bundles onto an un-scaled 2D plane. In top left panel, object color and shape represent pathways, and object size designates deterministic/probabilistic tractogram. While variation exists within pathways and within deterministic/probabilistic streamlines, white matter pathways of the same axonal bundle generally cluster together in low dimensional space. Insets visualize data points as streamline renderings, and highlight areas where similarity and/or overlap is shown across different pathways. Reproduced from Schilling et al (2021).

## 4.6 Discussion

All the results reported here are the outcome of a massive international effort led by Kurt G. Shilling and I was the lead participant from the neuroimaging group of the University of Pavia

---

and worked on optimising the pipeline. The principal aim was obtain a bundle segmentation with highest anatomical fidelity using literature and anatomy knowledge as target for ROIs placement. Overall, the collective work identify and quantify differences and the significant heterogeneity of white matter structures specifically introduced by the use of different protocols for bundle segmentation with tractography. This variability may present difficulties interpreting differences in bundle segmentation results obtained by different labs, or meta-analyses extending and comparing findings from one study to other studies. Additionally, this variation in protocols can lead to variability in quantitative metrics derived along the tracts, which results greater than true biological variability across populations or subjects and may hinder translation of these techniques from the research laboratory to the clinic. We propose that a major source of this variation stems from a lack of consensus on the anatomical definition of pathways. Differences, misconceptions, and ambiguities in anatomical definitions and their interpretation may lead to different rules used in the dissection process. Indeed, is possible that misconceptions could actually lead to a wrong segmentation.

Our first main result is that the inter-protocol agreement is generally poor across protocols for many pathways, with limited agreement on the brain volume occupied by the pathway. With few exceptions, the average Dice coefficients from both deterministic and probabilistic streamlines were below 0.5, with many considerably lower. Because our analysis was based on the same set of streamlines, these results represent a best-case measure of inter-protocol agreement, and would almost certainly result in increased variability if participants performed their own reconstruction and streamline generation procedures. It would be interesting to see how these metrics changed if all groups were given not only the same streamlines but also the same instructions on how to define fidelity to anatomy, hence assessing a different level of subjective error.

Our second main result is that bundle segmentation protocols have better agreement in areas with high streamline densities. Measures of streamline density correlation coefficients across submissions are on average greater than 0.5, with few exceptions, which suggests that high density areas in tractograms generally correspond to high density areas of other tractograms, while low density areas correspond to low density areas. These areas of higher streamline

density correspond to the core or stem of most of the bundles, generally located in the deep white matter of the brain.

Third, we find that the variability across protocols is greater than the variability within protocols, and more importantly, similar to (or greater than) the variability across subjects.

The final main result is that the measured variability depends on the scale upon which the variability is analyzed. Protocols show little-to-no agreement in assigning individual streamlines to a pathway, whereas protocols show higher agreement in assessing spatial overlap of pathway, and even higher agreement when taking into account density of streamlines over a volume. This means that while selected streamlines may occupy the same volume, the streamlines that make up this volume are different. Thus, the effects of this variability are dependent upon how these bundles are ultimately utilized in practice, and there are a number of ways in which these bundles are used and applied.

This study has several limitations which constrain the generalizability of the results. First, there is a low number of subjects and low number of repeats. Next, we did not include a number of pathways with functional relevance in the literature, but chose a sample representative of the commonly studied projection, association, and commissural bundles, and, again, a compromise was made between the number of pathways requested and expected time and effort. Further, because we wanted to isolate the effect of bundle segmentation protocols, teams were forced to use the same generated tractogram. This may not be optimal for a given segmentation process where streamlines are generated using different parameters or propagation methods, and filtered or excluded in various ways. However, allowing the creation of different streamlines would only increase the variability seen across protocols. Future studies may investigate which protocols (and which features of those protocols) result in bundles that are more or less similar to other protocols, and more importantly, quantify how well different protocols result in bundles that match the desired anatomical definition.

---

## 4.7 Conclusion

We have identified variability in the protocols for bundle segmentation, which parallels variability in the literature of other techniques that have been used to elucidate the structure and function of the brain for the last 20 years.

We postulate that the problem stems from two sources (1) the anatomical definition of a white matter pathway and (2) the constraints used to dissect this pathway. The different descriptions of the white matter pathways given by teams highlight the problem of “definition”. Pathways may be defined by their shape, their endpoints, or by regions through which they pass. Descriptions and definition approaches may vary based on the pathway itself, by the system or functions under investigation, by the training and/or occupation of the researcher/clinician, or by the modality used to define the tract.

## ***Chapter 5***

# **Impact of cerebro-cerebellar and long association fibers in Temporal Lobe Epilepsy**

This chapter will describe the use and application of advanced tractography to reconstruct cerebro-cerebellar and long association fibers. The obtained bundles will be characterized with diffusion tensor imaging, diffusion kurtosis imaging and NODDI parameter extracted features. The aim of the work presented in this chapter is to investigate whether white matter alterations of specific tracts can be selectively related to dysfunction of declarative long term memory in epilepsy patients.

### **5.1 Background and motivation**

In chapter 3, we showed that white matter (WM) alterations patterns are specific for left and right Temporal Lobe Epilepsy (TLE) patients. Particularly, interesting alterations were found in the cerebellum, which is getting increasing attention in experimental models of epilepsy (Krook-Magnuson, 2014). In the last two decades its role in higher cognitive functions has been increasingly recognized, thus raising the interest of neuroscience and neuroimaging communities. Indeed, recent models hypothesize that the cerebellum has a crucial role in seizure resolution, suggesting that it could be a potential target for therapeutic intervention (Streng & Krook-Magnuson, 2020). Volumes of bilateral lobule Crus I, lobule VI, and right lobule IV of the cerebellum have demonstrated to be significantly associated with memory recall scores (Cui 2020). Further, some evidence reported that acute modulation of the cerebellum alters hippocampal function, also illustrating that the cerebellum can influence cognitive domains (Zeider 2020). Different studies proved there is a key role of the cerebellum in memory regulation (Ferrari et al., 2018; Gatti et al., 2020, 2021; Monaco et al., 2014; Zeidler et al., 2020). From a systematic review of structural and functional MRI data (Beez et al., 2021)

---

cognitive, emotional, and limbic functions have been found to be located in the posterior cerebellum; these posterior cerebellar areas project white matter fibers to the cerebral cortex through the middle cerebellar peduncle through the pontocerebellar tracts.

In order to investigate the involvement of specific tracts in cognitive function we considered classically psychological assessment, which has been widely used as a tool to evaluate proper memory functioning. However, it is important to remember that it is impossible to create measures of a single, specific type of memory.

The mesial temporal lobe plays a pivotal role in declarative episodic long-term memory (LTM). Indeed, in the study used for this analysis we used the Paired Associate Learning (PAL) task and the Short Stories Test (SST). PAL tasks enable analysis of how learning new semantically connected words may impact the encoding process. The examiner pronounced a list of word pairs, from which half were semantically related and half were semantically unrelated. In the retrieval phase subjects were given a cue, pronouncing the first word of the pair, and patients were asked to recall associated words. Such design enabled us to analyze the impact of semantic link between two words from a pair on the process of learning. On the other hand, SST tests relies on the immediate and delayed recall of heard stories. While it allows us to test recollection of heard words, an important presupposition is the ability of participants to properly comprehend language. Such implicit assumption should be always taken into account as this may be an important limitation of test explanatory power.

Here, we further investigated TLE patients in order to assess whether white matter alterations of specific tracts can be selectively correlated to left or right dysfunction of LTM (Salvato et al., 2016). We examined both the long association fibers passing through the temporal lobes, well known and studied as involved in memory functions, and less-examined tracts involved in the cerebro-cerebellar circuits. These tracts were reconstructed using advanced tractography (Smith et al., 2012) and characterized by the mean of microstructural metrics derived from Diffusion Tensor Imaging (DTI) (Alexander et al., 2007), Diffusion Kurtosis Imaging (DKI) (Jensen et al., 2005), and Neurite Orientation Dispersion and Density Imaging (NODDI) (Zhang et al., 2012).

## 5.2 Protocol

### 5.2.1 Subjects

This study used MRI data and neuropsychological assessment data from the 3TLE project (chapter 4). A subsample of 28 TLE patients ( $36.0 \pm 8.9$ y, 16 females) and 16 healthy controls (HC) ( $32.3 \pm 6.8$ y, 8 females) were considered. Seizures were lateralized according to medical history, neurological examination, interictal electroencephalography, and positron emission tomography. The epileptogenic zone was located in the left hemisphere for 13 patients ( $35.3 \pm 7.8$ y, 7 females) and in the right for 15 patients ( $36.7 \pm 10.0$ y, 9 females). Participants were given an extensive presurgical neuropsychological assessment from which paired associate learning (PAL) and short story tests (SST) were selected.

### 5.2.2 MRI acquisition

MRI data were acquired as described in chapter 3.2.2.

### 5.2.3 MRI processing

- Diffusion data were analyzed using a combination of commands from MRtrix3 and FSL software packages and 3DT1w data were post processed using FSL.
- Here each step of the analysis pipeline is described.
- Gibbs-ringing reduction and denoising of DW images were performed using MRtrix3, while eddy-currents and geometrical distortion correction, motion realignment, and brain extraction (Smith, 2002) were performed on the DW images using FSL.
- An affine transformation with 12 degree of freedom (FLIRT algorithm, FSL) was used in order to align the 3DT1w volumes to the diffusion data (Jenkinson et al., 2002b). No warping correction was needed because the two images were acquired on the same subject. From this point onward such space will be considered as the subject's native space.
- 3DT1w images were segmented into cortical gray, deep gray and white matter, as well as cerebrospinal fluid, and normalized to the MNI152 space.

- 
- DTI fitting was used to create maps of fractional anisotropy (FA), mean, axial and radial diffusivity (MD, AD and RD); DKI provided mean, axial and radial kurtosis (MK, AK and RK); NODDI provided maps of orientation dispersion index (ODI) and neurite density index (NDI) as described in Chapter 3.2.3.
  - Pre-processed data were used to derive diffusion metrics under several models. DESIGNER (<https://github.com/NYU-DiffusionMRI/DESIGNER>) (Ades-Aron et al., 2018) was used to fit the gaussian (DTI) and non-gaussian (DKI) part of the signal, more linked to the complexity of the microstructural environment (Steven et al., 2014), and to calculate maps of FA, mean, axial and radial diffusivities (MD, AD and RD), and mean, axial and radial kurtosis (MK, AK and RK). Three-compartment NODDI model (H. Zhang et al., 2012) provided ODI and NDI maps, which can explain the source of diffusion anisotropy, and was fitted to the signal using the Matlab toolbox ([https://www.nitrc.org/projects/noddi\\_toolbox](https://www.nitrc.org/projects/noddi_toolbox)).

## 5.2.4 Whole-brain tractography and TDI maps

Multi-shell-multi-tissue constrained spherical deconvolution (Jeurissen et al., 2014) and probabilistic streamline tractography algorithm (iFOD2) (Santyr et al., 2018) were used to perform a whole-brain anatomically constrained tractography (Smith, 2012) using MRtrix3. Streamlines were randomly seeded throughout the whole brain until 30 million tracks were selected (Tournier et al., 2012). From these streamlines a TDI map was computed as the total number of streamlines passing within each element of a user defined 1 mm resolution grid (Calamante et al., 2010).

## 5.2.5 Tract extraction and characterization

Specific regions of interest (ROIs) were defined in MNI152 space and aligned to the DW images of all subjects by inverting the T1w to MNI152 transformation, i.e., the normalization procedure (as reported in chapter 4.4). From the whole-brain tractogram, 12 tracts were extracted, 6 for each hemisphere:

1. superior longitudinal fasciculus (SLF) (Schilling, 2020) (Fig. 5.1)
2. inferior longitudinal fasciculus (ILF) (Schilling, 2020) (Fig. 5.1)
3. uncinate fasciculus (UF) (Schilling, 2020) (Fig. 5.1)

4. cingulum (CG) (Schilling, 2020) (Fig. 5.1)
5. cerebello-thalamo-cortical (CTC) (Palesi, 2015) (Fig. 5.2)
6. cerebro-ponto-cerebellar (CPC) (Palesi, 2017) (Fig. 5.2)

Tracts 1 to 4 were extracted placing ROIs as described in Chapter 4.4. Tracts 5 and 6 were extracted placing ROIs as described by Palesi et al. 2015 and 2017.

For each tract, the volume and mean value of all diffusion-derived metrics were obtained. Differences between the three groups (HC, Left-TLE and Right-TLE) were evaluated with an ANOVA test, and their correlations with neuropsychological scores were assessed with Pearson's correlation coefficient (SPSSv21, <https://www.ibm.com/it-it/analytics/spss-statistics-software>).

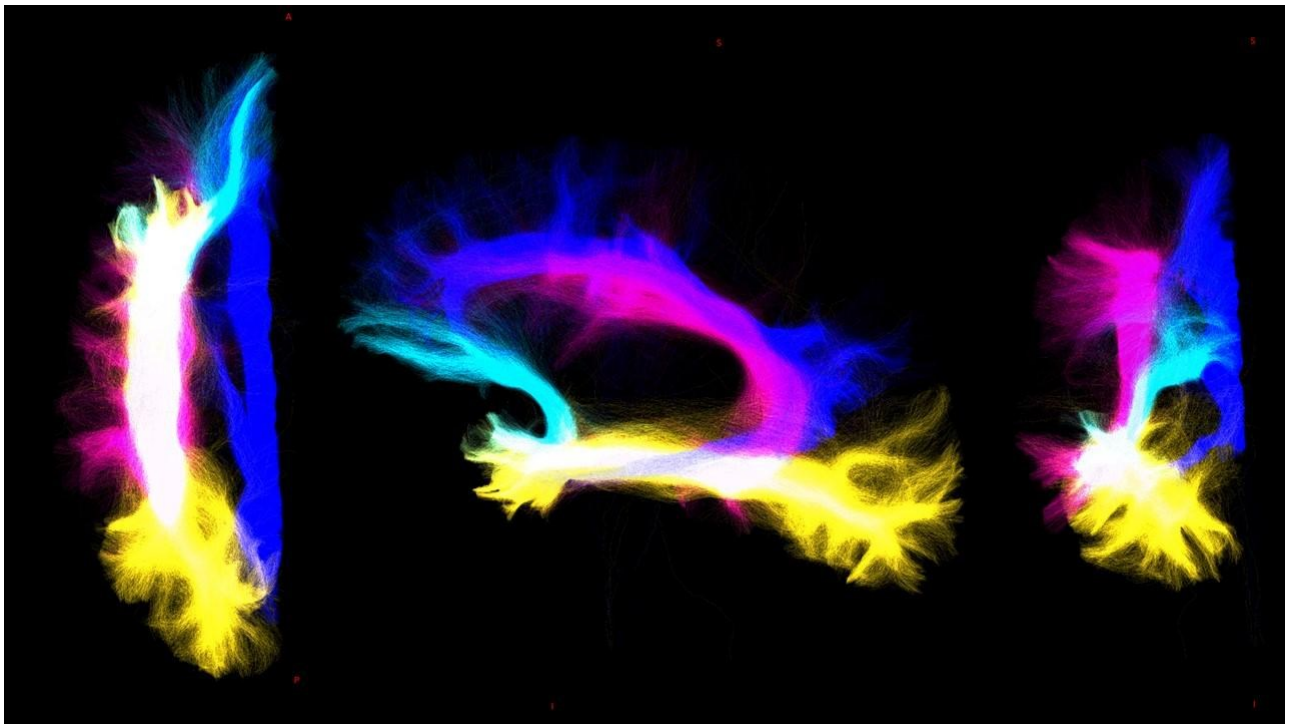


Figure 5.1: From left to right: axial, sagittal, and coronal view of tracts rendering of the cingulum (blue), superior longitudinal fasciculus (purple), inferior longitudinal fasciculus (yellow), and uncinate fasciculus (light blue). Areas with high density of streamline belonging to two or more bundles are displayed in white.

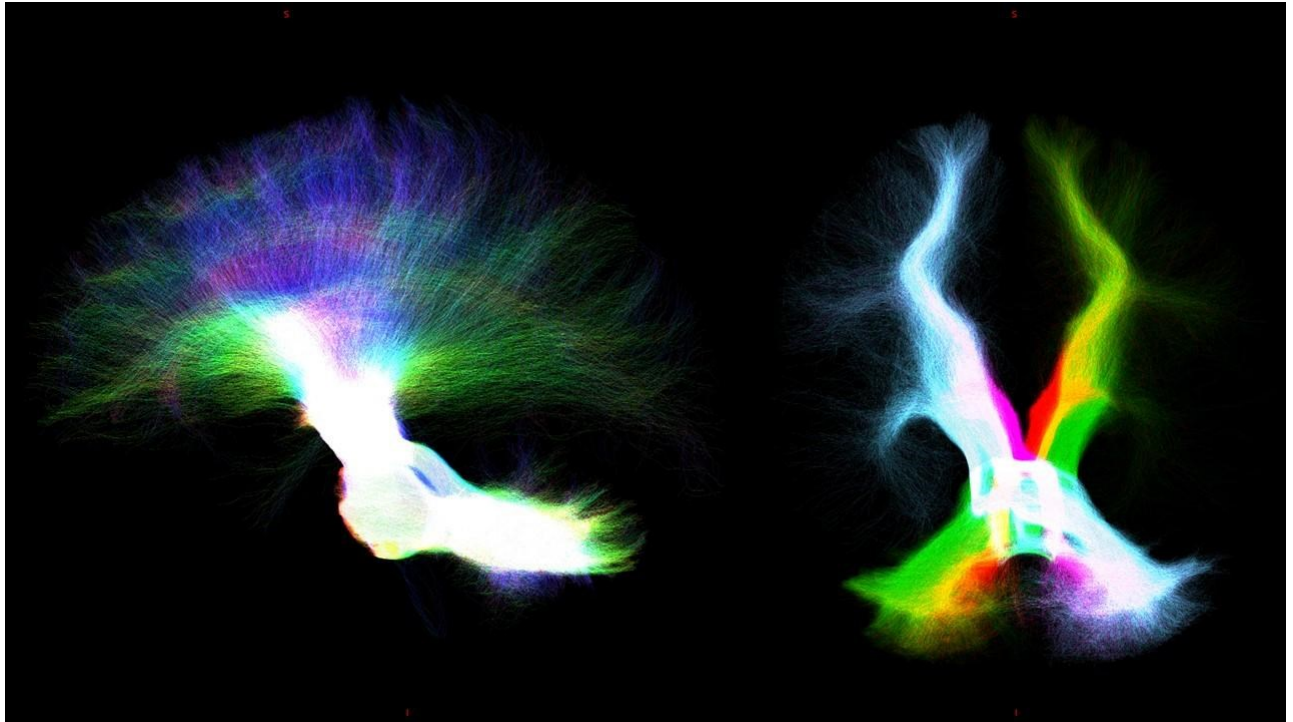


Figure 5.2: From left to right, sagittal (rgb color direction) and coronal view of tracts reconstruction of cerebello-thalamo-cortical (left purple and right red) and cerebro-ponto-cerebellar tract (left light blue and right green). Areas with high density of streamline belonging to two or more bundles are displayed in white (or yellow where the colors of the two overlapped bundles are red and green).

### 5.3 Results

DTI-derived metrics were not significantly altered in TLE patients, while MK and RK decreased compared to HC in all (bilateral) long association fibers and in the CG in both Left-TLE and Right-TLE. ODI increase was detected in Right-TLE, in the right ILF and left UF compared to HC. Furthermore, Right-TLE showed volume reduction of the CPC tract connecting the right cerebral cortex with the left cerebellum. The most affected tract was the UF, which showed bilateral impairment both in Left-TLE and Right-TLE (Figure 5.3).

Furthermore, ODI of left CG negatively correlated with PAL ( $p$ -value=0.020) and with SST ( $p$ -value=0.048) in Left-TLE, while ODI of right SLF negatively correlated with PAL ( $p$ -value=0.016) (Figure 5.4).

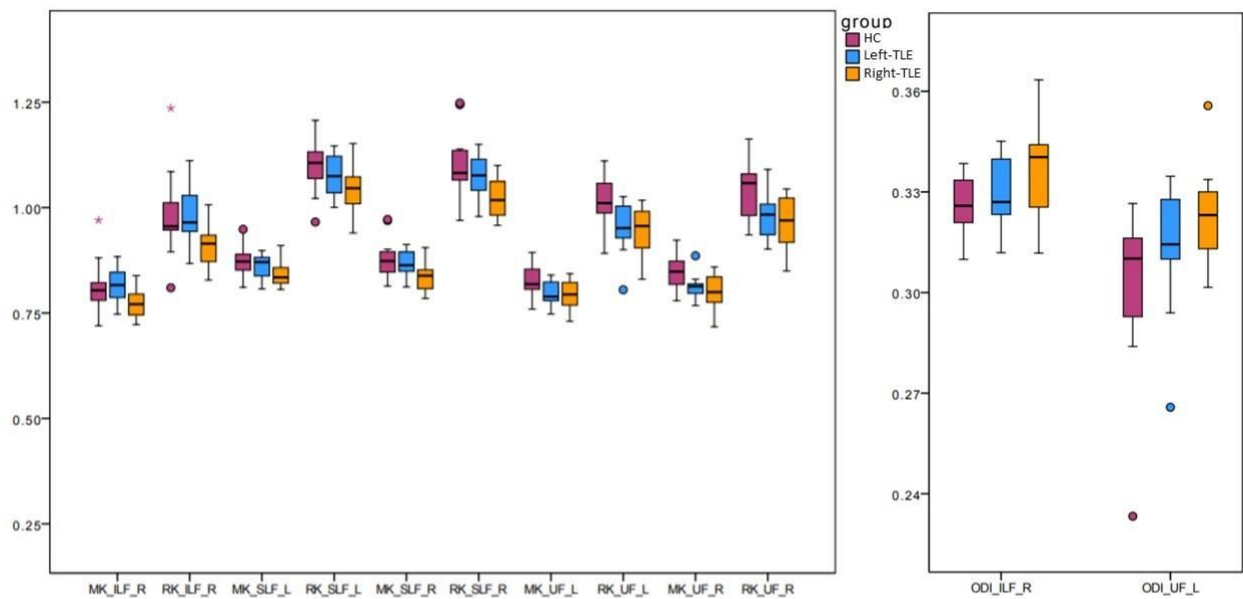


Figure 5.3: Boxplots of metrics comparison between groups (HC in purple, Left-TLE in blue and Right-TLE in orange).

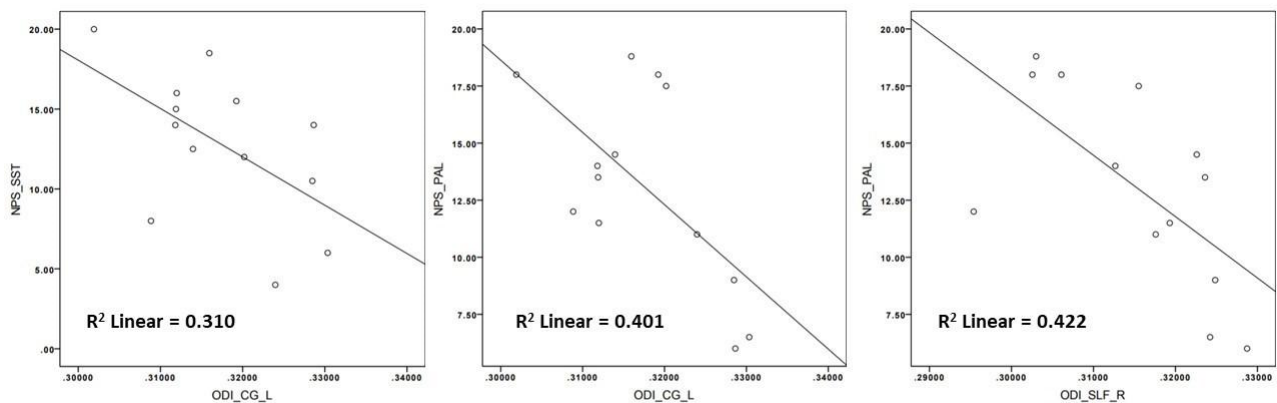


Figure 5.4: Correlation between neuropsychological score and metrics. SST: Short Story Telling; PAL: Pair Association Learning; ODI: orientation dispersion; CG: Cingulum Bundle; SLF: Superior Longitudinal Fasciculus.

## 5.4 Discussion

In this work, we investigated whether WM alterations of specific tracts can be selectively related to dysfunction of declarative long term memory in TLE patients. Right-TLE showed more alterations than Left-TLE. This finding is surprising because generally, and also in our previous work, left-TLE presented more widespread WM impairment. A possible explanation

---

could be the small sample size. Given that we considered specific long associative tracts covering a large portion of the temporal lobes known to be altered, this result is puzzling. It is also possible that having averaged microstructural properties over long-range tracts, possible localized alterations in the proximity of the epileptogenic area may have been obscured by more normal distal voxels. Similarly, previously observed WM alterations localized in the cerebellum may be diluted when properties are averaged along the entire tract from the cerebellum to the cortex. Indeed, we hypothesize that the UF is the most compromised tract because it is the shortest amongst the reconstructed tracts and the closest to the hippocampus, hence to the epileptogenic area.

The anticorrelation that emerged between neuropsychological scores and CG can be explained by the fact that a great portion of this tract terminates into the hippocampal gyrus, supporting its strong involvement in memory. Increased ODI corresponds to less coherent fiber orientation and low PAL corresponds to worse performance. Correlations of SLF ODI with PAL can be explained by the overall role of the right SLF with language functions.

These preliminary results encourage further investigations to assess WM alterations in relation to specific systems and circuits. Moreover, the relationship between microstructural alterations and neuropsychological scores should be investigated with linear regression models able to identify which specific metrics are responsible for neuropsychological tests variance. Finally, it would be very interesting to see whether any of these metrics is predictive of post-surgery outcome and neuropsychological scores acquired longitudinally.

# *Chapter 6*

## **Conclusion**

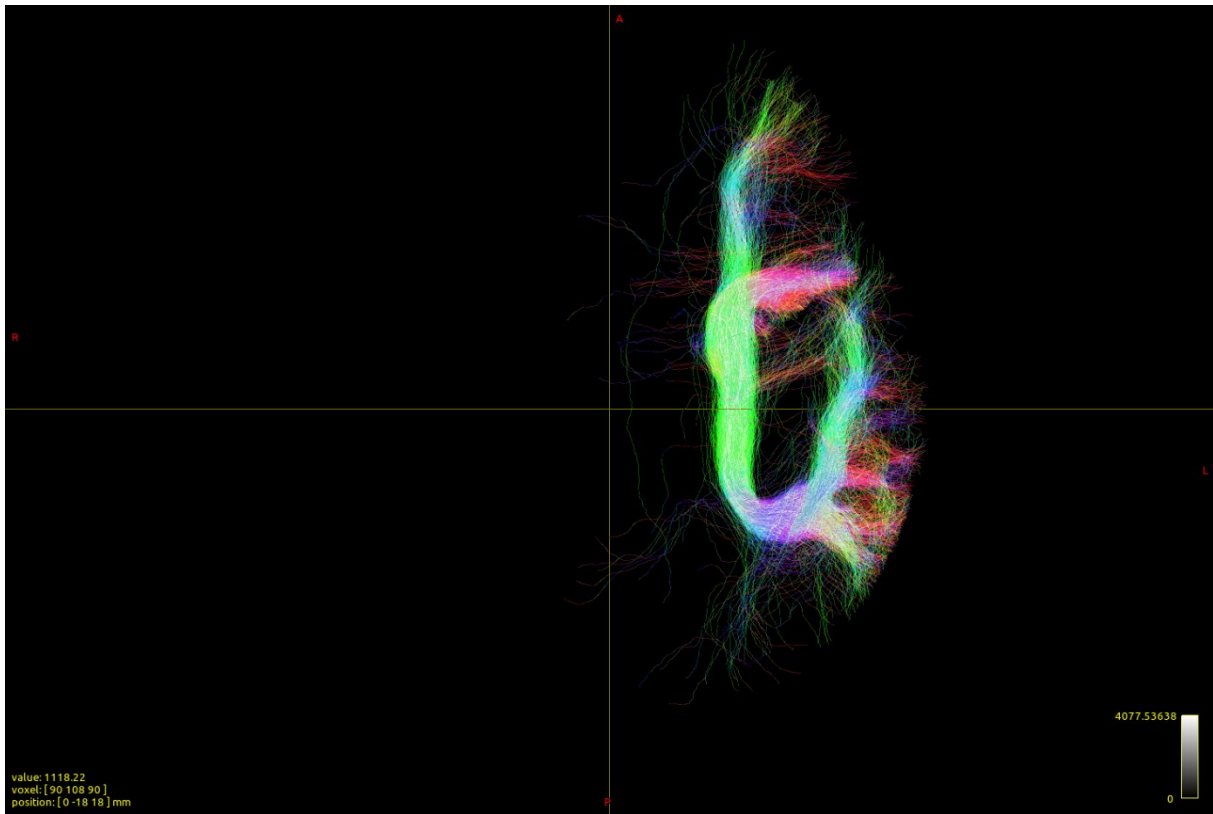
The core point of this thesis was the application of advanced DTI (tractography and microstructural parameters) in order to investigate WM structure in terms of alteration in pathology condition.

From the TBSS analysis emerge that L-TLE patients were characterized by extensive and generalized alterations of WM bundles, while R-TLE patients showed more local WM alterations. Furthermore, the use of advanced microstructure metrics from DKI and NODDI, other than FA from DTI, can help discriminating WM alterations in subgroups of TLE pathology.

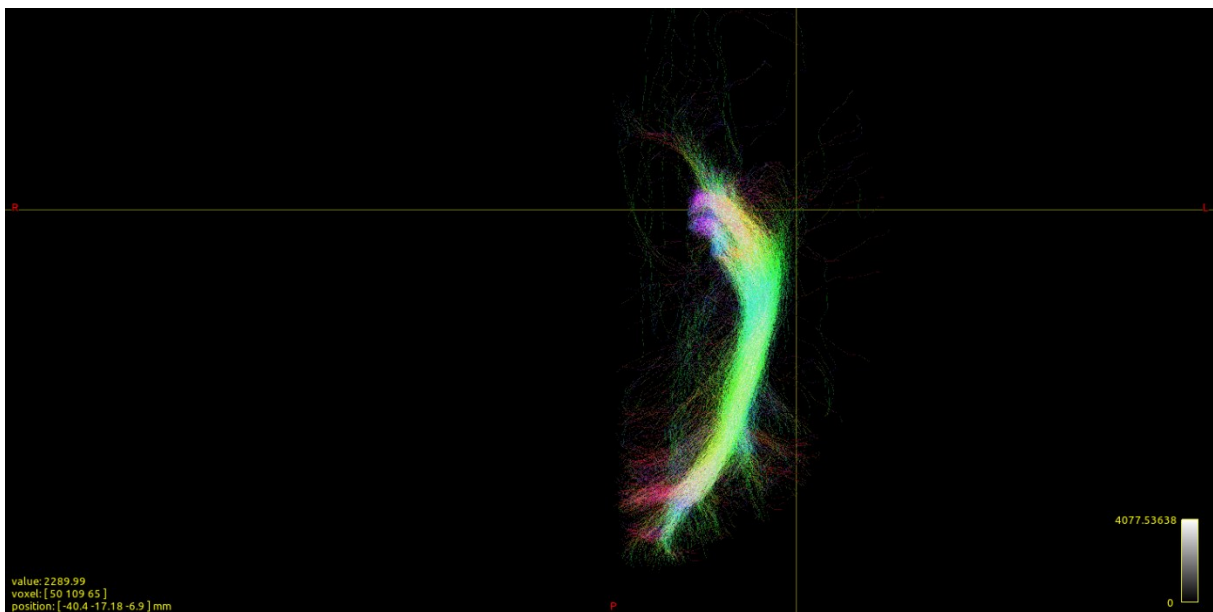
Advanced probabilistic tractography method was applied to investigate, in healthy human subjects, the variability in the protocols for bundle segmentation. We postulate that the problem arise from the anatomical definition of a white matter pathway and the constraints used to dissect this pathway.

Finally, we applied advanced tractography reconstruction and advanced diffusion metric in the study of TLE pathology. The study of correlation between microstructural alteration of specific bundle and neuropsychological test, could help to understand their implication in specific cognitive function.

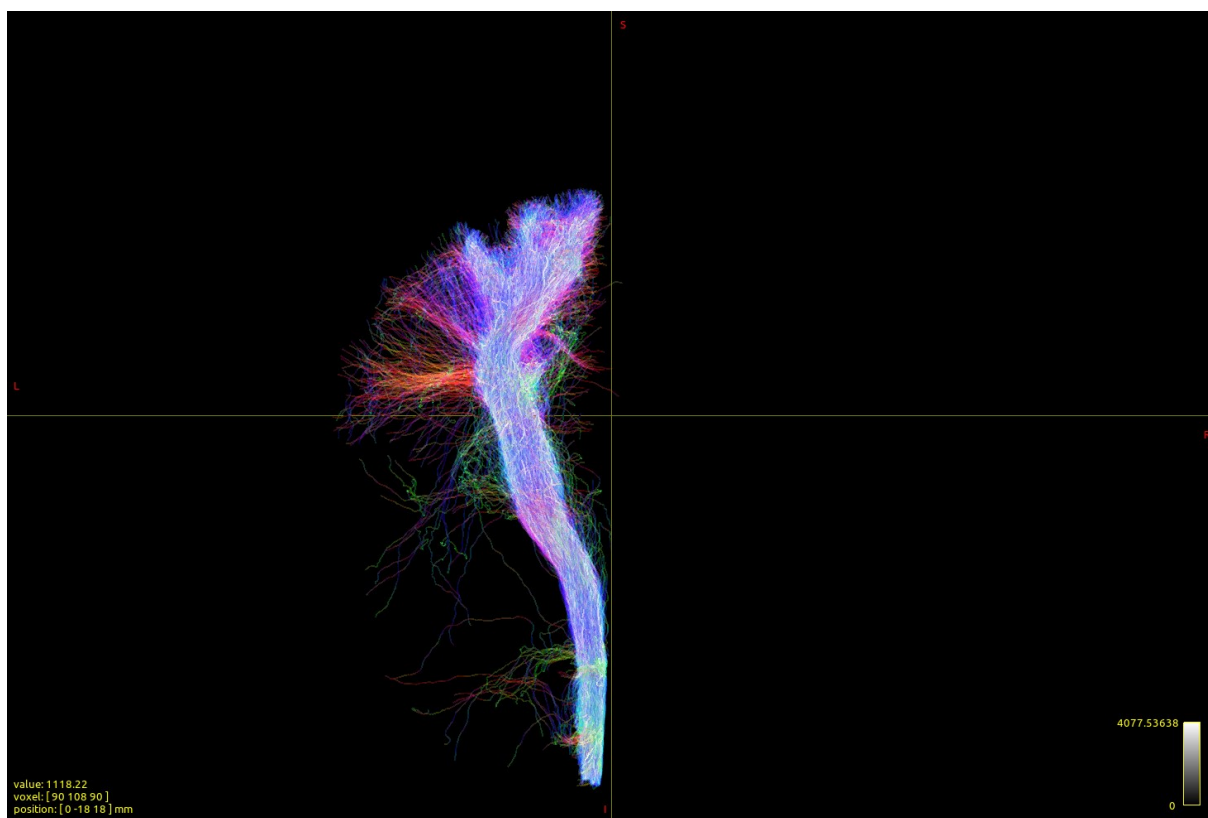
# Appendices



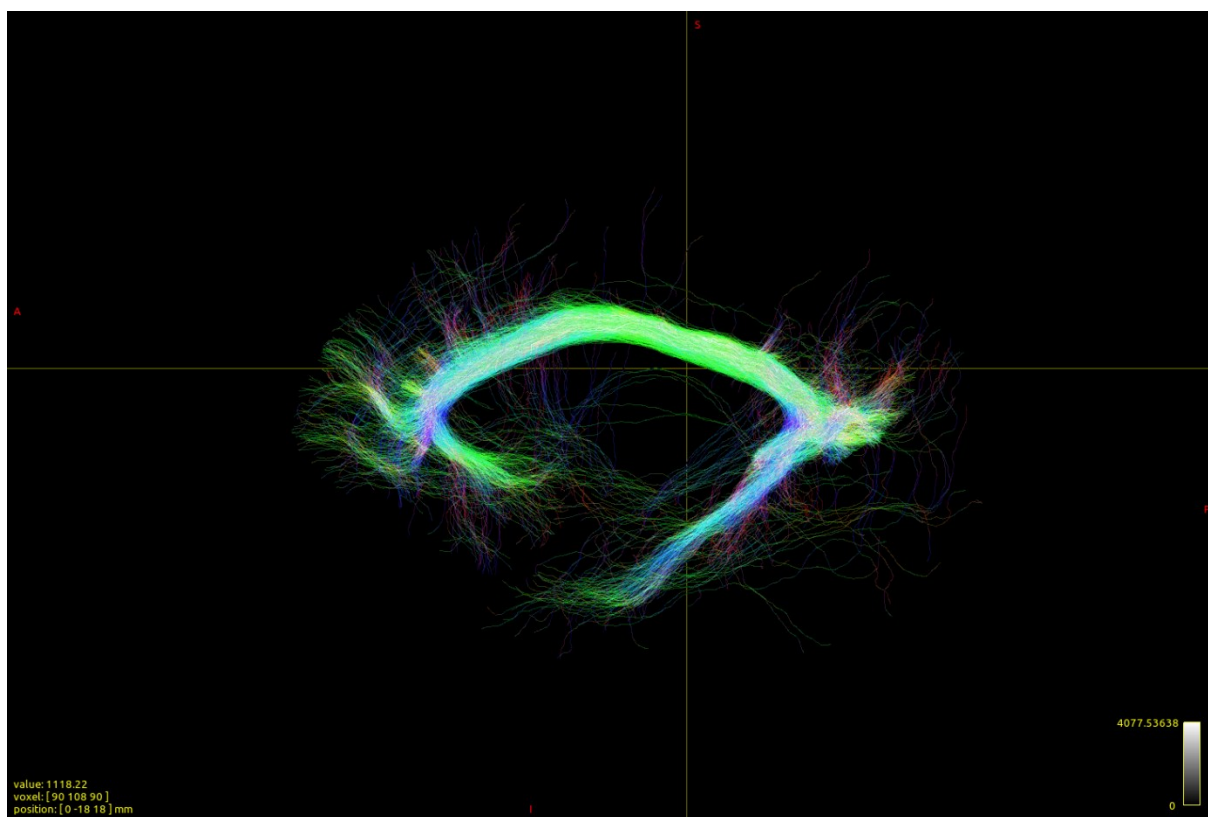
Superior Longitudinal Fasciculus (SLF) axial view.



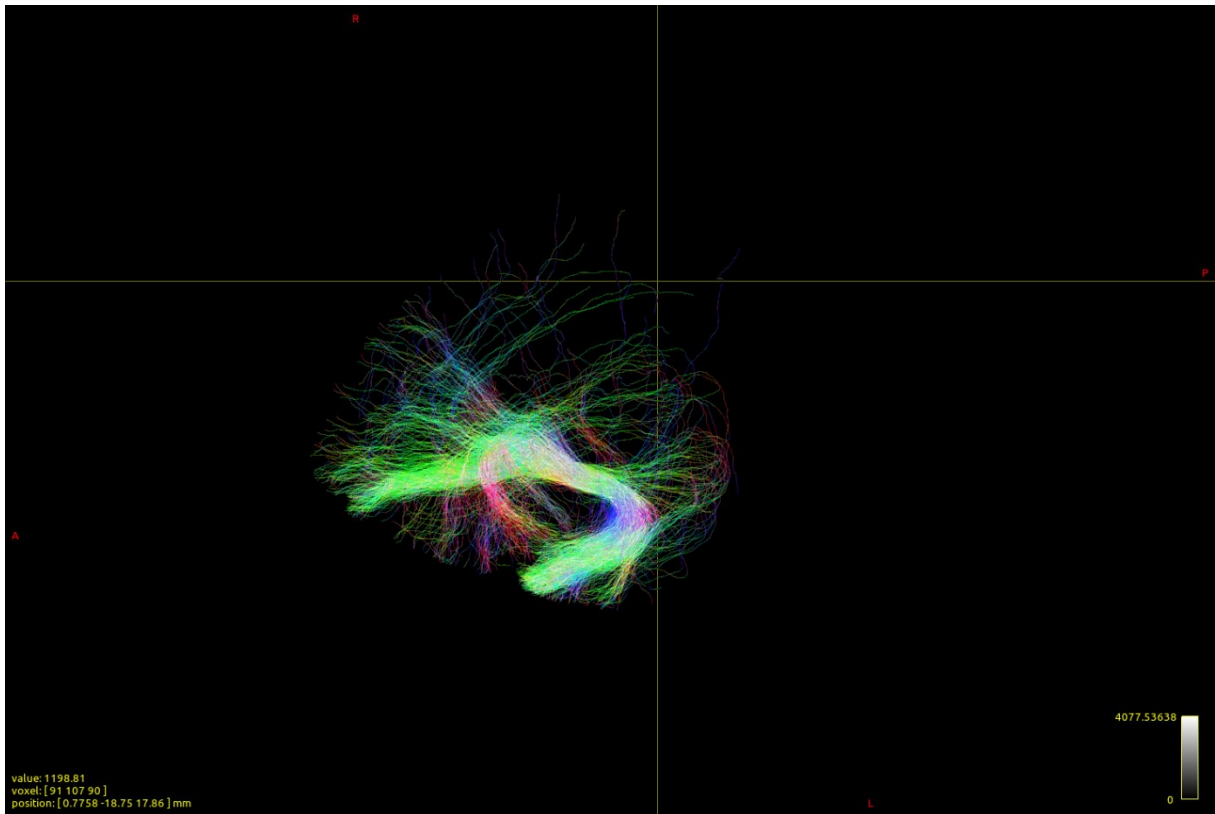
Optic Radiation (OR) axial view.



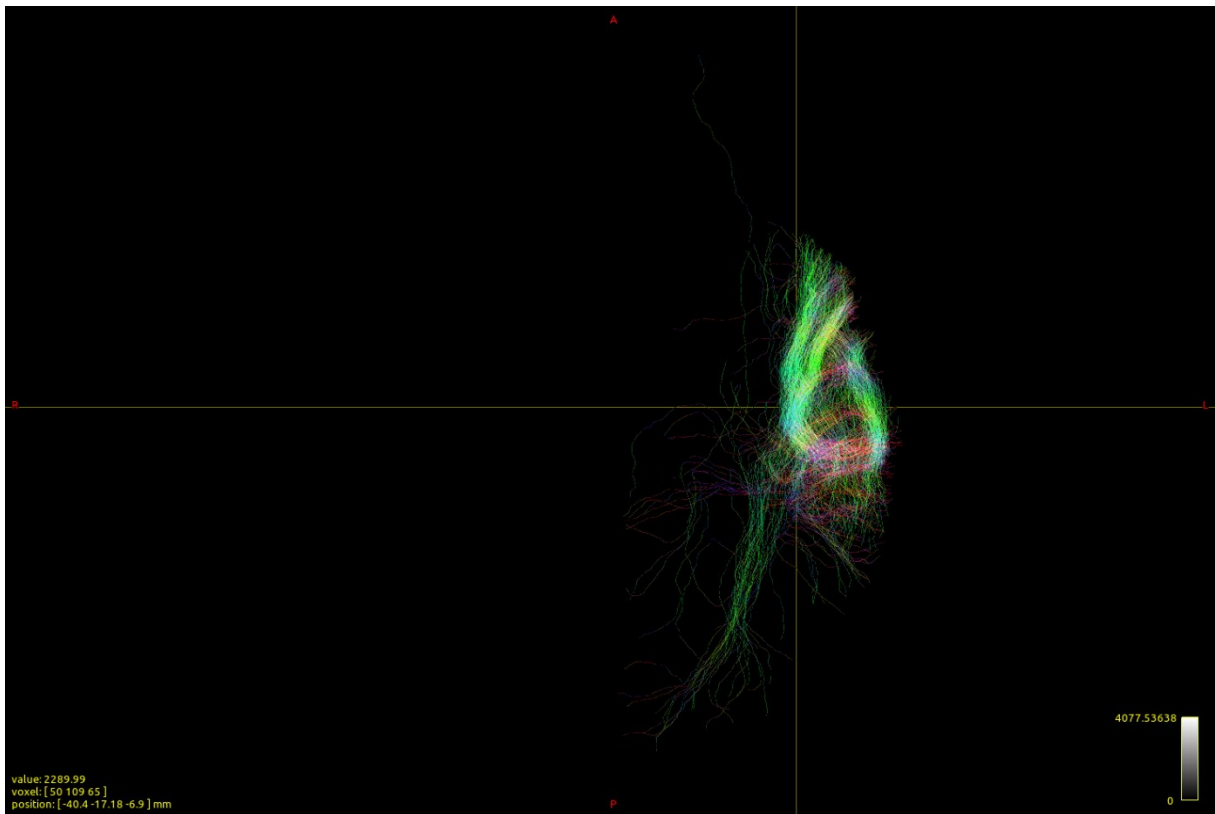
Corticospinal Tract (CST) coronal view.



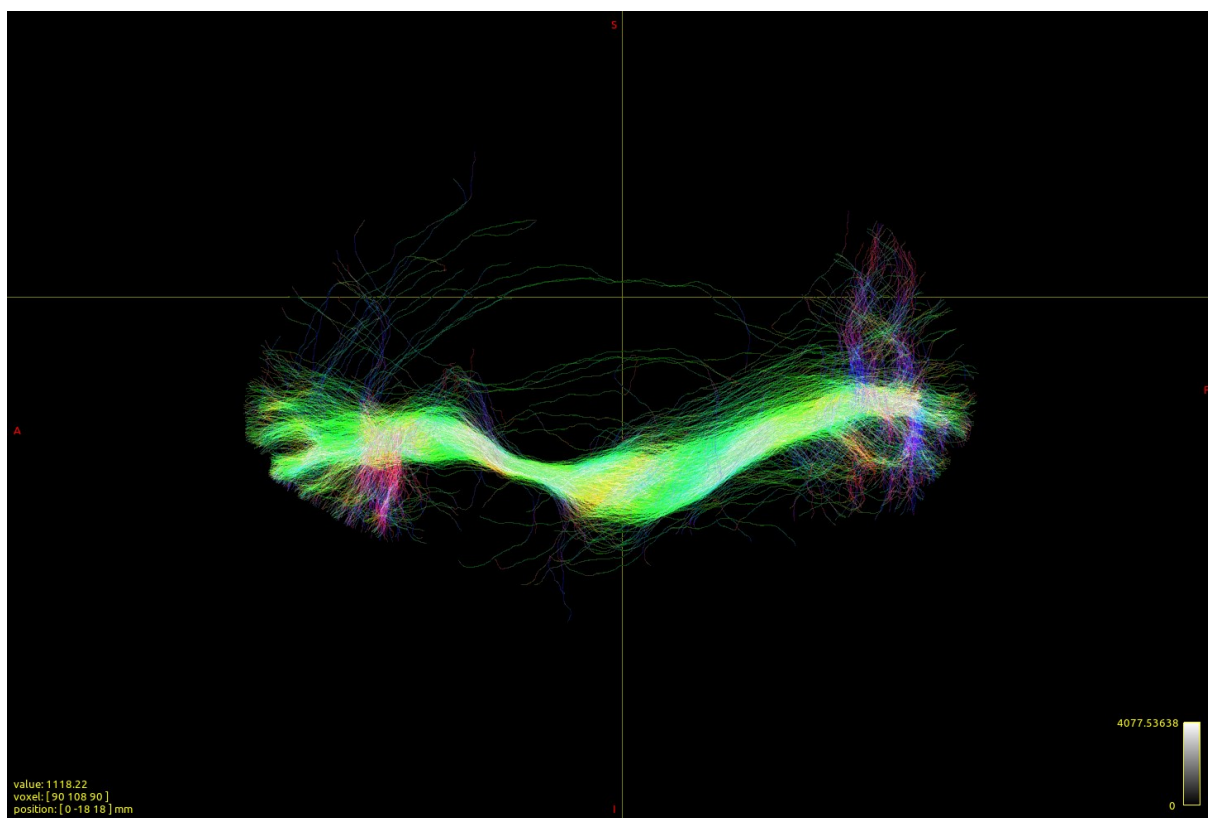
Cingulum (CG) sagittal view.



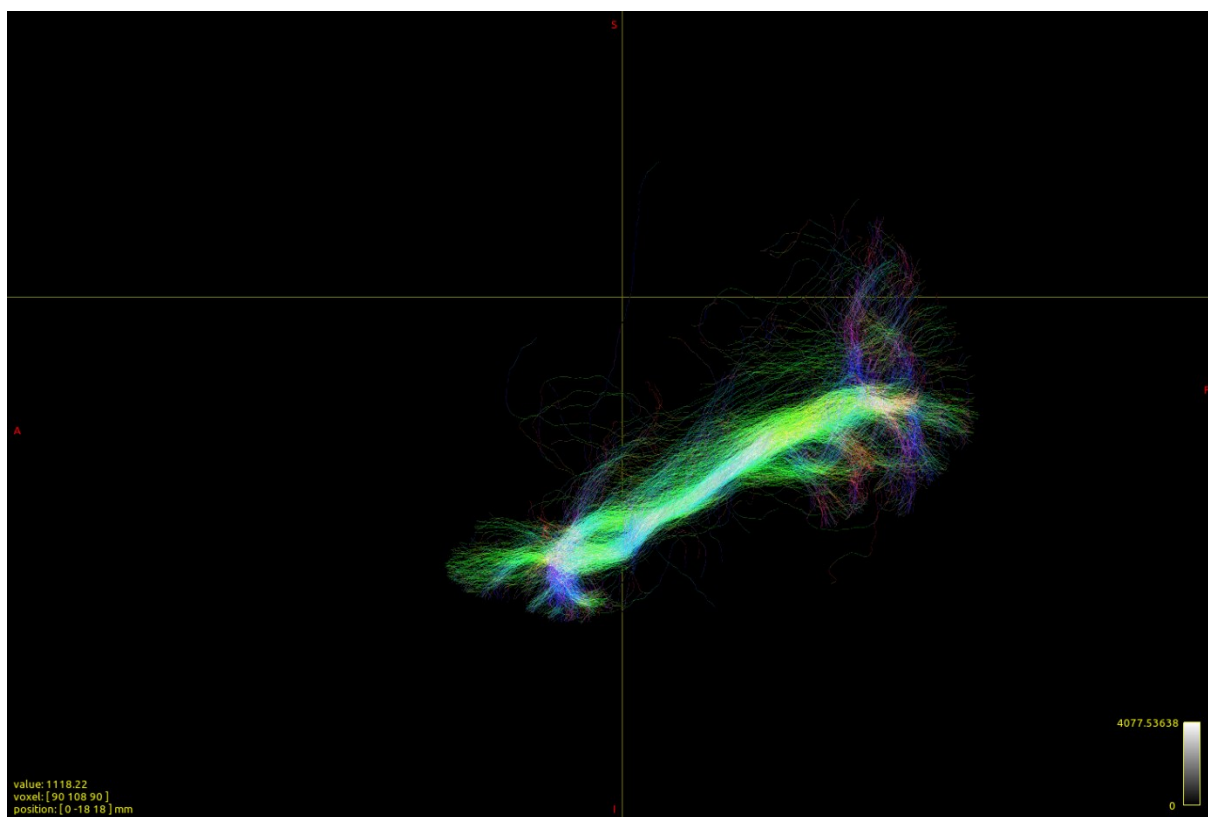
Uncinate Fasciculus (UF) sagittal view.



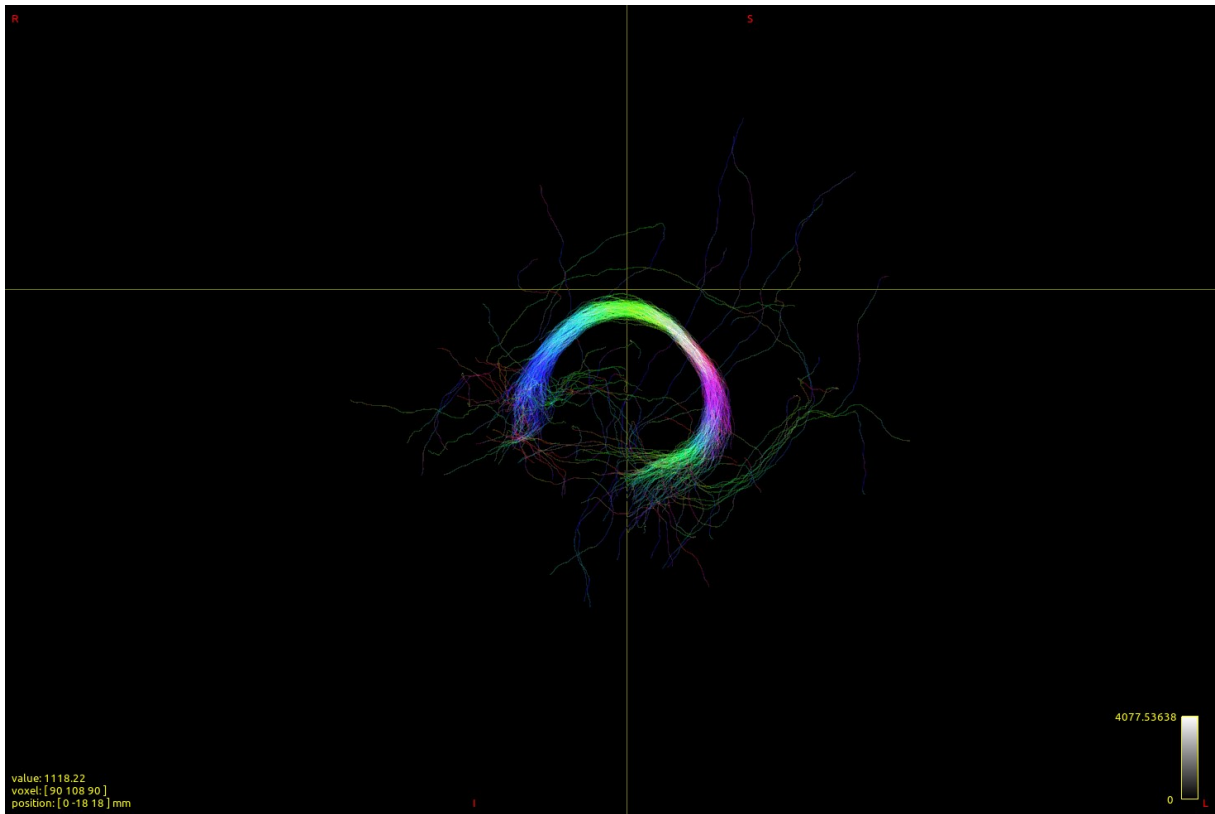
Middle Longitudinal Fasciculus (MLF) axial view.



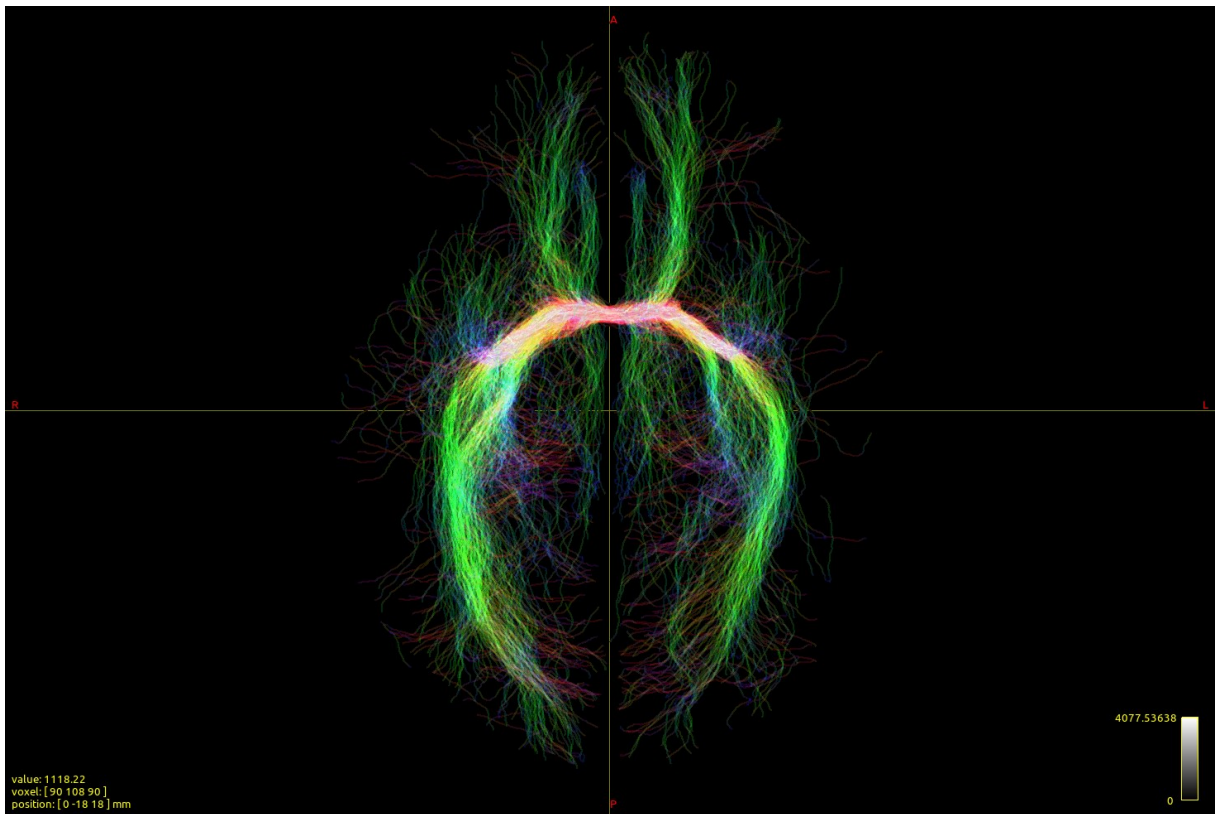
Inferior Fronto-Occipital Fasciculus (IFOF) sagittal view.



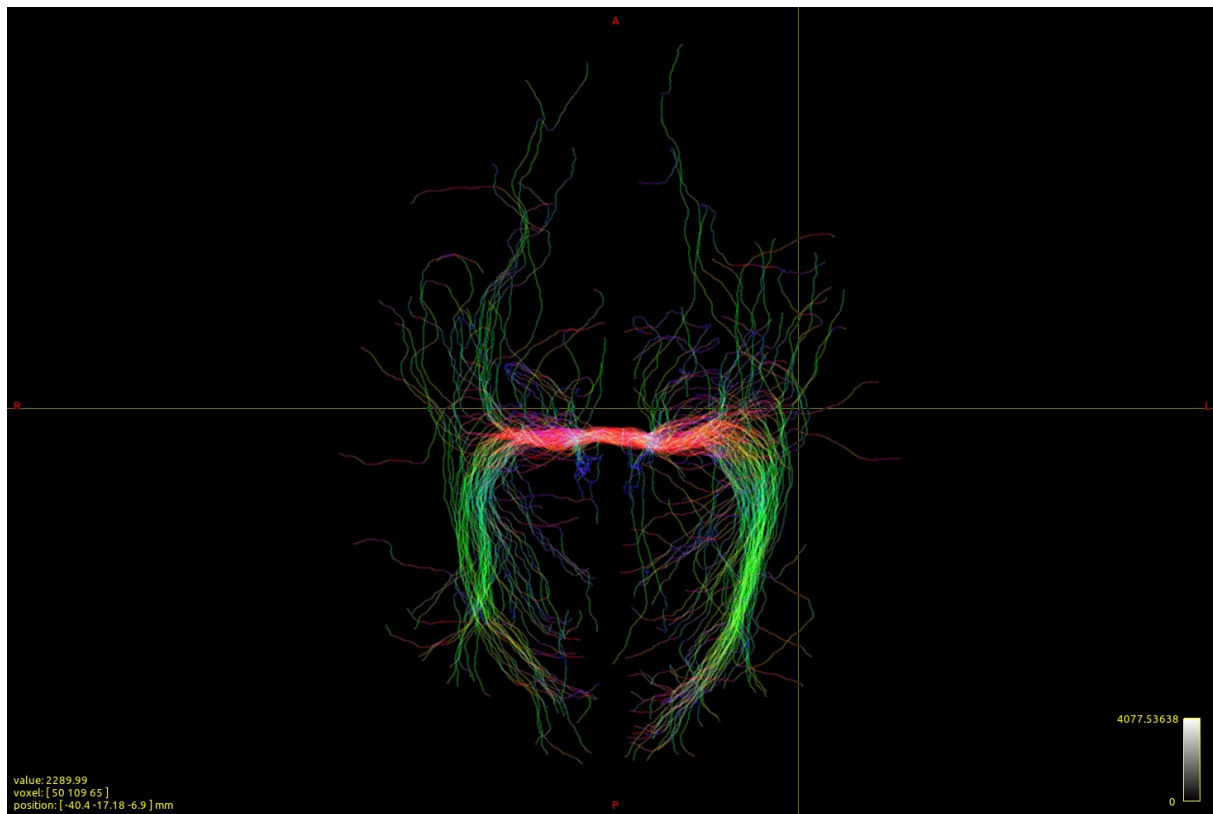
Inferior Longitudinal Fasciculus (ILF) sagittal view.



Fornix (FX) sagittal view.



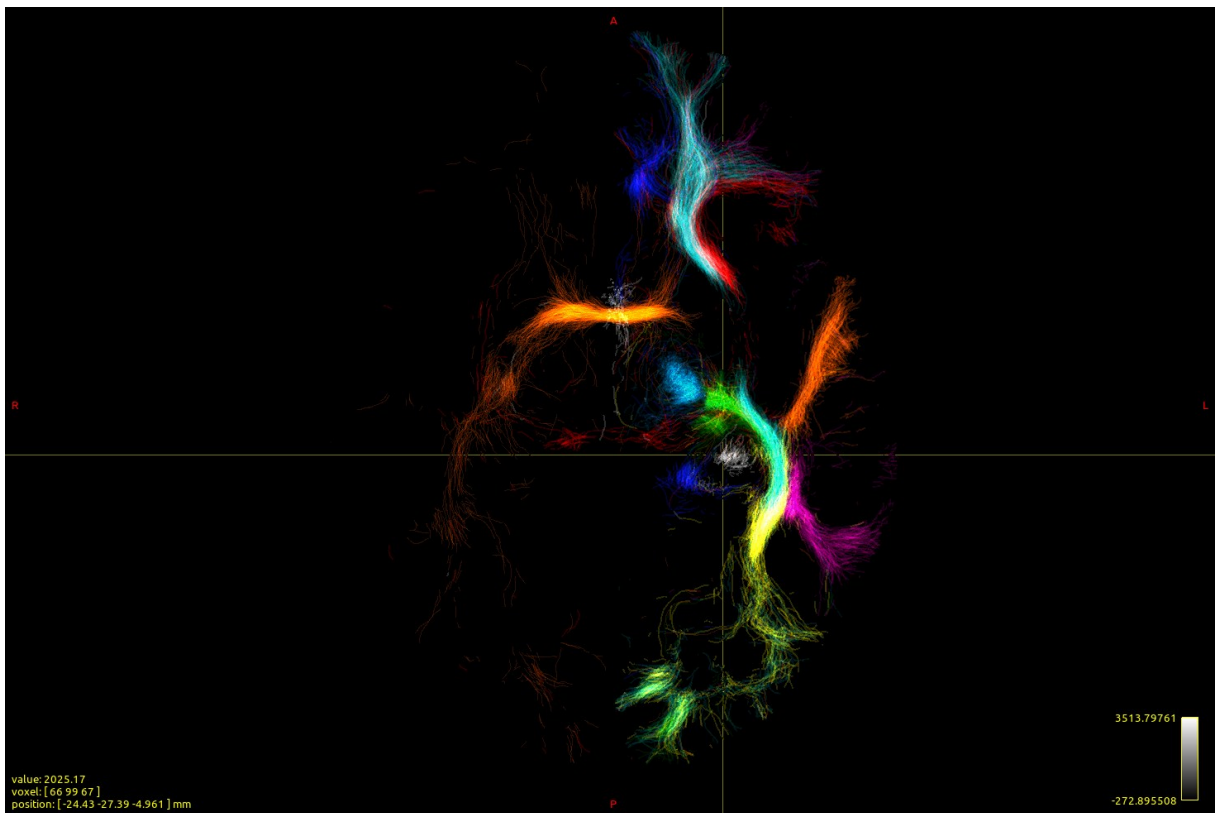
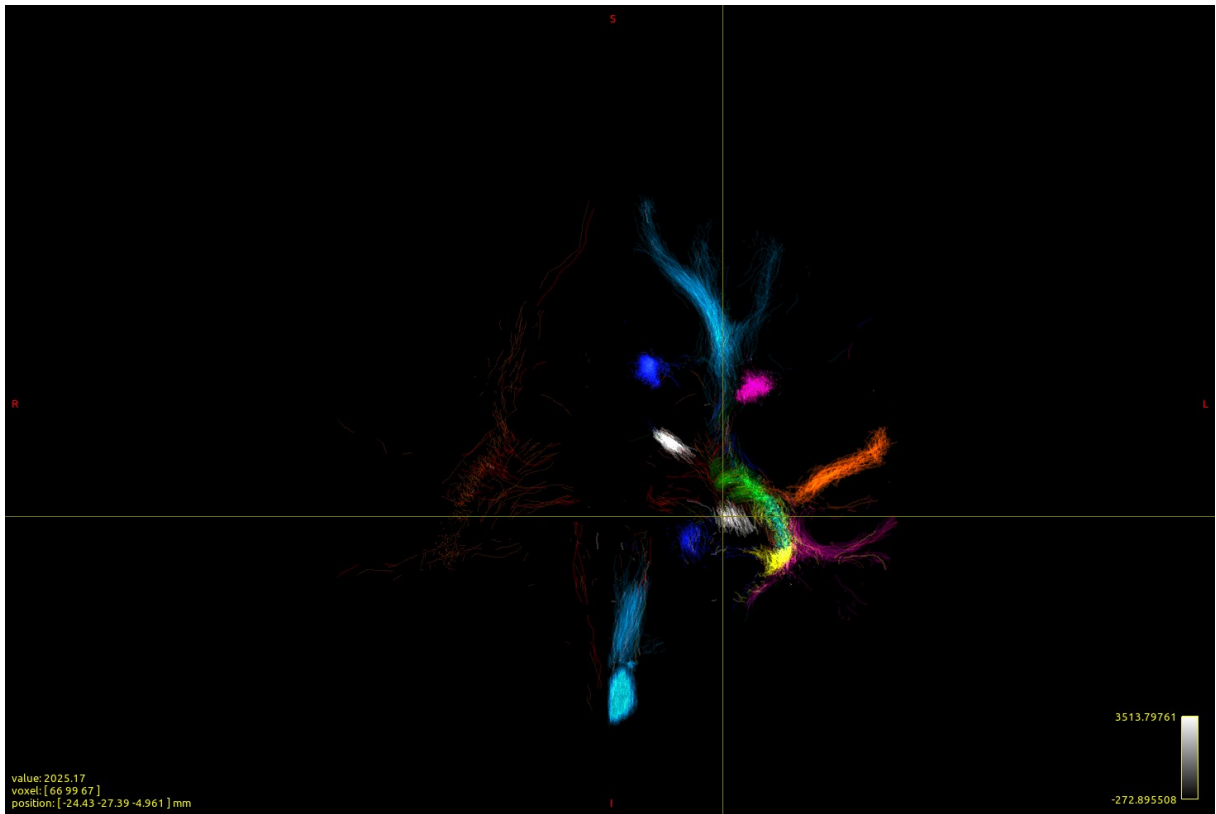
Anterior Commissure (AC) axial view.

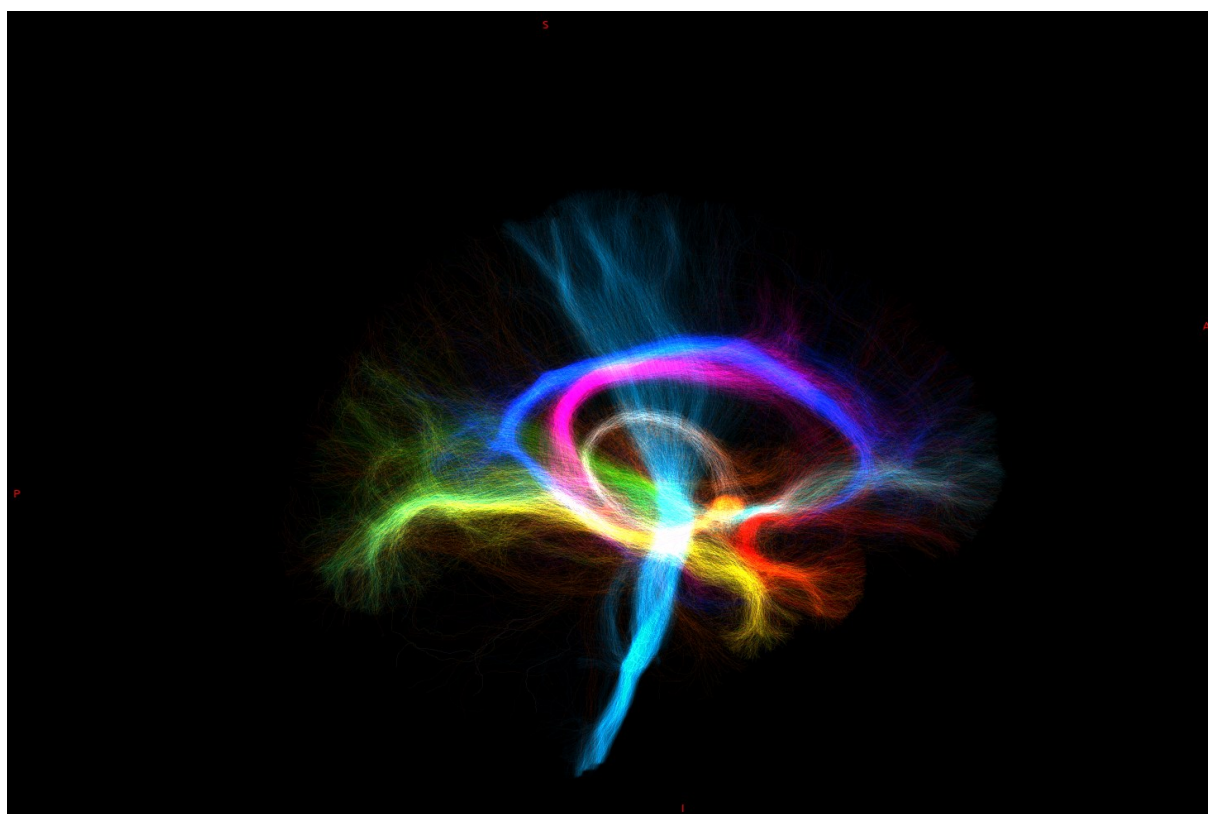
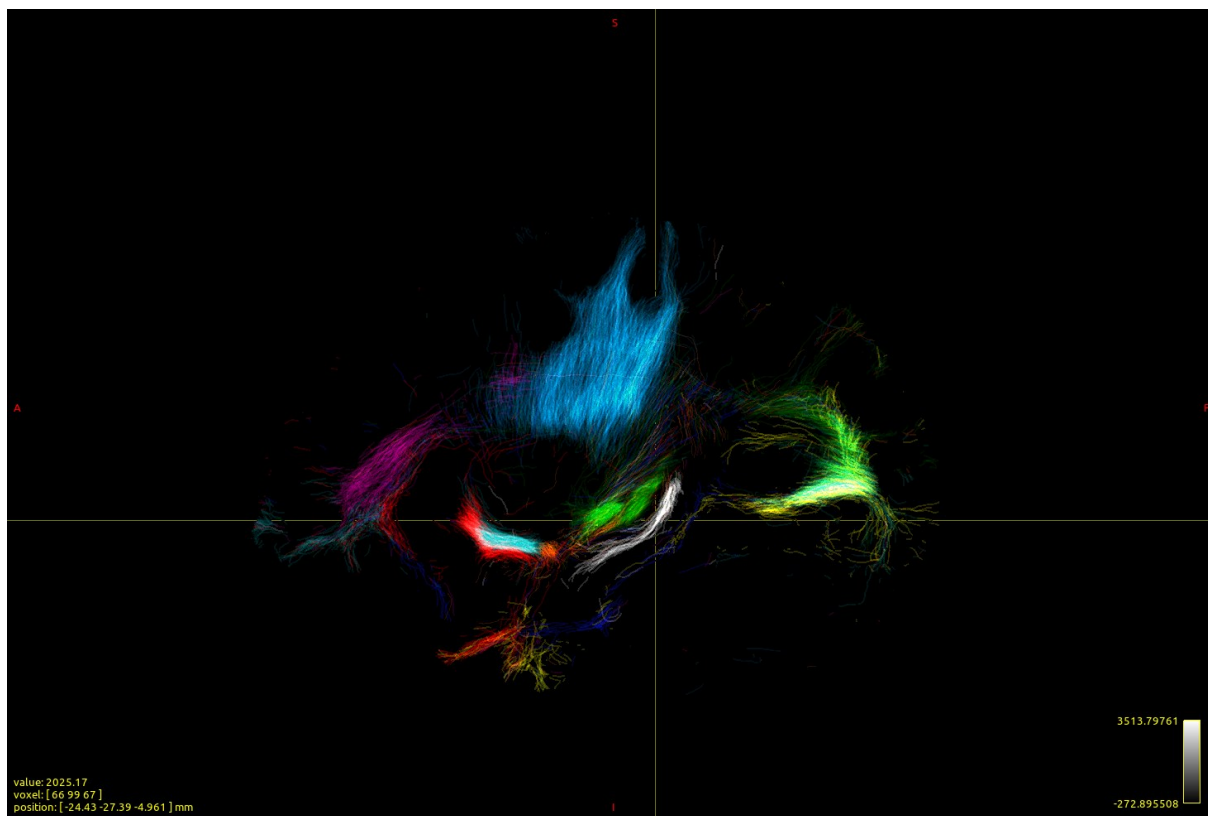


Posterior Commissure (PC) axial view.

In the following images are reported all above tract in sagittal, coronal and axial view, plus a 3D rendering.

Purple (SLF), Green (OR), Light blue (CST), Blue (CG), Red (UF), Orange (MLF), Cyan (IFOF), Yellow (ILF), white (FX), Orange AC, Red (PC).





---

## References

Ades-Aron, B., Veraart, J., Kochunov, P., McGuire, S., Sherman, P., Kellner, E., Novikov, D. S., & Fieremans, E. (2018). Evaluation of the accuracy and precision of the diffusion parameter ESTimation with Gibbs and Noise removal pipeline. *NeuroImage*, *183*(July), 532–543. <https://doi.org/10.1016/j.neuroimage.2018.07.066>

Ahmadi, M. E., Hagler, D. J., McDonald, C. R., Tecoma, E. S., Iragui, V. J., Dale, A. M., & Halgren, E. (2009). Side matters: Diffusion tensor imaging tractography in left and right temporal lobe epilepsy. *American Journal of Neuroradiology*, *30*(9), 1740–1747. <https://doi.org/10.3174/ajnr.A1650>

Alessio, A., Damasceno, B. P., Camargo, C. H. P., Kobayashi, E., Guerreiro, C. A. M., & Cendes, F. (2004). Differences in memory performance and other clinical characteristics in patients with mesial temporal lobe epilepsy with and without hippocampal atrophy. *Epilepsy and Behavior*, *5*(1), 22–27. <https://doi.org/10.1016/j.yebeh.2003.10.010>

Blair, R. D. G. (2012). Temporal Lobe Epilepsy Semiology. *Epilepsy Research and Treatment*, *2012*, 1–10. <https://doi.org/10.1155/2012/751510>

Blumcke, I., Spreafico, R., Haaker, G., Coras, R., Kobow, K., Bien, C. G., Pfäfflin, M., Elger, C., Widman, G., Schramm, J., Becker, A., Braun, K. P., Leijten, F., Baayen, J. C., Aronica, E., Chassoux, F., Hamer, H., Stefan, H., Rössler, K., ... Avanzini, G. (2017). Histopathological Findings in Brain Tissue Obtained during Epilepsy Surgery. *New England Journal of Medicine*, *377*(17), 1648–1656. <https://doi.org/10.1056/nejmoa1703784>

Buksakowska, I., Szabó, N., Martinkovič, L., Faragó, P., Király, A., Vrána, J., Kincses, Z. T., Meluzín, J., Šulc, V., Kynčl, M., Roček, M., Tichý, M., Charvát, F., Hořínek, D., & Marusič, P. (2019). Distinctive Patterns of Seizure-Related White Matter Alterations in Right and Left Temporal Lobe Epilepsy. *Frontiers in Neurology*, *10*(October), 1–10. <https://doi.org/10.3389/fneur.2019.00986>

Collorone, S., Cawley, N., Grussu, F., Prados, F., Tona, F., Calvi, A., Kanber, B., Schneider, T., Kipp, L., Zhang, H., Alexander, D. C., Thompson, A. J., Toosy, A., Wheeler-kingshott, C. A. M. G., & Ciccarelli, O. (2020). *Reduced neurite density in the brain and cervical spinal cord in*

*relapsing – remitting multiple sclerosis: A NODDI study.* 1647–1657.  
<https://doi.org/10.1177/1352458519885107>

Del Gaizo, J., Mofrad, N., Jensen, J. H., Clark, D., Glenn, R., Helpert, J., & Bonilha, L. (2017). Using machine learning to classify temporal lobe epilepsy based on diffusion MRI. *Brain and Behavior*, 7(10), e00801. <https://doi.org/10.1002/brb3.801>

Fahoum, F., Lopes, R., Pittau, F., Dubeau, F., & Gotman, J. (2012). Widespread epileptic networks in focal epilepsies: EEG-fMRI study. *Epilepsia*, 53(9), 1618–1627. <https://doi.org/10.1111/j.1528-1167.2012.03533.x>

Fisher, R. S., Acevedo, C., Arzimanoglou, A., Bogacz, A., Cross, J. H., Elger, C. E., Engel, J., Forsgren, L., French, J. A., Glynn, M., Hesdorffer, D. C., Lee, B. I., Mathern, G. W., Moshé, S. L., Perucca, E., Scheffer, I. E., Tomson, T., Watanabe, M., & Wiebe, S. (2014). ILAE Official Report: A practical clinical definition of epilepsy. *Epilepsia*, 55(4), 475–482. <https://doi.org/10.1111/epi.12550>

Garbelli, R., Milesi, G., Medici, V., Villani, F., Didato, G., Deleo, F., D'Incerti, L., Morbin, M., Mazzoleni, G., Giovagnoli, A. R., Parente, A., Zucca, I., Mastropietro, A., & Spreafico, R. (2012). Blurring in patients with temporal lobe epilepsy: Clinical, high-field imaging and ultrastructural study. *Brain*, 135(8), 2337–2349. <https://doi.org/10.1093/brain/aws149>

Guglielmetti, C., Veraart, J., Roelant, E., Mai, Z., Daans, J., Van Audekerke, J., Naeyaert, M., Vanhoutte, G., Delgado y Palacios, R., Praet, J., Fieremans, E., Ponsaerts, P., Sijbers, J., Van der Linden, A., & Verhoye, M. (2016). Diffusion kurtosis imaging probes cortical alterations and white matter pathology following cuprizone induced demyelination and spontaneous remyelination. *NeuroImage*, 125, 363–377. <https://doi.org/10.1016/j.neuroimage.2015.10.052>

Jallon, P., Loiseau, P., & Loiseau, J. (2001). Newly diagnosed unprovoked epileptic seizures: Presentation at diagnosis in CAROLE study. *Epilepsia*, 42(4), 464–475. <https://doi.org/10.1046/j.1528-1157.2001.31400.x>

- 
- Jayalakshmi, S., Vooturi, S., Vadapalli, R., Somayajula, S., Madigubba, S., & Panigrahi, M. (2016). Outcome of surgery for temporal lobe epilepsy in adults – A cohort study. *International Journal of Surgery*, *36*, 443–447. <https://doi.org/10.1016/J.IJSU.2015.05.006>
- Jenkinson, M., Beckmann, C. F., Behrens, T. E. J., Woolrich, M. W., & Smith, S. M. (2012). FSL. *NeuroImage*, *62*, 782–790. <https://doi.org/10.1016/j.neuroimage.2011.09.015>
- Jensen, J. H., Helpert, J. A., Ramani, A., Lu, H., & Kaczynski, K. (2005). Diffusional kurtosis imaging: The quantification of non-Gaussian water diffusion by means of magnetic resonance imaging. *Magnetic Resonance in Medicine*, *53*(6), 1432–1440. <https://doi.org/10.1002/mrm.20508>
- Kalilani, L., Sun, X., Pelgrims, B., Noack-Rink, M., & Villanueva, V. (2018). The epidemiology of drug-resistant epilepsy: A systematic review and meta-analysis. *Epilepsia*, *59*(12), 2179–2193. <https://doi.org/10.1111/epi.14596>
- Kwan, P., Arzimanoglou, A., Berg, A. T., Brodie, M. J., Hauser, W. A., Mathern, G., Moshé, S. L., Perucca, E., Wiebe, S., & French, J. (2010). Definition of drug resistant epilepsy: Consensus proposal by the ad hoc Task Force of the ILAE Commission on Therapeutic Strategies. *Epilepsia*, *51*(6), 1069–1077. <https://doi.org/10.1111/j.1528-1167.2009.02397.x>
- Lemkaddem, A., Daducci, A., Kunz, N., Lazeyras, F., Seeck, M., Thiran, J.-P., & Vulliémoz, S. (2014). Connectivity and tissue microstructural alterations in right and left temporal lobe epilepsy revealed by diffusion spectrum imaging. *NeuroImage: Clinical*, *5*, 349–358. <https://doi.org/10.1016/J.NICL.2014.07.013>
- Li, H., Xue, Z., Dulay, M. F., Verma, A., Karmonik, C., Grossman, R. G., & Wong, S. T. (2014). Fractional anisotropy asymmetry and the side of seizure origin for partial onset-temporal lobe epilepsy. *Computerized Medical Imaging and Graphics*, *38*(6), 481–489. <https://doi.org/10.1016/J.COMPMEDIMAG.2014.06.009>
- Liu, M., Bernhardt, B. C., Bernasconi, A., & Bernasconi, N. (2016). Gray matter structural compromise is equally distributed in left and right temporal lobe epilepsy. *Human Brain Mapping*, *37*(2), 515–524. <https://doi.org/10.1002/hbm.23046>

- Miller, J., Watrous, A. J., Tsitsiklis, M., Lee, S. A., Sheth, S. A., Schevon, C. A., Smith, E. H., Sperling, M. R., Sharan, A., Asadi-Pooya, A. A., Worrell, G. A., Meisenhelter, S., Inman, C. S., Davis, K. A., Lega, B., Wanda, P. A., Das, S. R., Stein, J. M., Gorniak, R., & Jacobs, J. (2018). Lateralized hippocampal oscillations underlie distinct aspects of human spatial memory and navigation. *Nature Communications*, *9*(1). <https://doi.org/10.1038/s41467-018-04847-9>
- Rodríguez-Cruces, R., & Concha, L. (2015). White matter in temporal lobe epilepsy: clinico-pathological correlates of water diffusion abnormalities. *Quantitative Imaging in Medicine and Surgery*, *5*(2), 264–278. <https://doi.org/10.3978/j.issn.2223-4292.2015.02.06>
- Rodríguez-Cruces, R., Velázquez-Pérez, L., Rodríguez-Leyva, I., Velasco, A. L., Trejo-Martínez, D., Barragán-Campos, H. M., Camacho-Téllez, V., & Concha, L. (2018). Association of white matter diffusion characteristics and cognitive deficits in temporal lobe epilepsy. *Epilepsy & Behavior*, *79*, 138–145. <https://doi.org/10.1016/j.YEBEH.2017.11.040>
- Rosazza, C., Ghielmetti, F., Minati, L., Vitali, P., Giovagnoli, A. R., Deleo, F., Didato, G., Parente, A., Marras, C., Bruzzzone, M. G., D'Incerti, L., Spreafico, R., & Villani, F. (2013). Preoperative language lateralization in temporal lobe epilepsy (TLE) predicts peri-ictal, pre- and post-operative language performance: An fMRI study. *NeuroImage: Clinical*, *3*, 73–83. <https://doi.org/10.1016/j.nicl.2013.07.001>
- Rossini, L., Garbelli, R., Gnatkovsky, V., Didato, G., Villani, F., Spreafico, R., Deleo, F., Lo Russo, G., Tringali, G., Gozzo, F., Tassi, L., & de Curtis, M. (2017). Seizure activity per se does not induce tissue damage markers in human neocortical focal epilepsy. *Annals of Neurology*, *82*(3), 331–341. <https://doi.org/10.1002/ana.25005>
- Salanova, V., Markand, O., & Worth, R. (2002). Temporal lobe epilepsy surgery: Outcome, complications, and late mortality rate in 215 patients. *Epilepsia*, *43*(2), 170–174. <https://doi.org/10.1046/j.1528-1157.2002.33800.x>
- Sanjari Moghaddam, H., Rahmani, F., Aarabi, M. H., Nazem-Zadeh, M.-R., Davoodi-Bojd, E., & Soltanian-Zadeh, H. (2019). White matter microstructural differences between right and left mesial temporal lobe epilepsy. *Acta Neurologica Belgica*, 1–9. <https://doi.org/10.1007/s13760-019-01074-x>

---

Scheffer, I. E., Berkovic, S., Capovilla, G., Connolly, M. B., Guilhoto, L., Hirsch, E., Jain, S., Mathern, G. W., & Solomon, L. (2018). *ILAE Classification of the Epilepsies Position Paper of the ILAE Commission for Classification and Terminology*. *58*(4), 512–521. <https://doi.org/10.1111/epi.13709>.ILAE

Sedda, A., Rivolta, D., Scarpa, P., Burt, M., Frigerio, E., Zanardi, G., Piazzini, A., Turner, K., Canevini, M. P., Francione, S., Lo Russo, G., & Bottini, G. (2013). Ambiguous emotion recognition in temporal lobe epilepsy: The role of expression intensity. *Cognitive, Affective, & Behavioral Neuroscience*, *13*(3), 452–463. <https://doi.org/10.3758/s13415-013-0153-y>

Smith, S. M., Jenkinson, M., Johansen-Berg, H., Rueckert, D., Nichols, T. E., Mackay, C. E., Watkins, K. E., Ciccarelli, O., Cader, M. Z., Matthews, P. M., & Behrens, T. E. J. (2006). Tract-based spatial statistics: Voxelwise analysis of multi-subject diffusion data. *NeuroImage*, *31*(4), 1487–1505. <https://doi.org/10.1016/j.neuroimage.2006.02.024>

Sone, D., Sato, N., Ota, M., Maikusa, N., Kimura, Y., & Matsuda, H. (2018). Abnormal neurite density and orientation dispersion in unilateral temporal lobe epilepsy detected by advanced diffusion imaging. *NeuroImage. Clinical*, *20*, 772–782. <https://doi.org/10.1016/j.nicl.2018.09.017>

Steven, A. J., Zhuo, J., & Melhem, E. R. (2014). Diffusion kurtosis imaging: An emerging technique for evaluating the microstructural environment of the brain. *American Journal of Roentgenology*, *202*(1), 26–33. <https://doi.org/10.2214/AJR.13.11365>

Toro, R., Chupin, M., Garnero, L., Leonard, G., Perron, M., Pike, B., Pitiot, A., Richer, L., Veillette, S., Pausova, Z., & Paus, T. (2009). Brain volumes and Val66Met polymorphism of the BDNF gene: Local or global effects? *Brain Structure and Function*, *213*(6), 501–509. <https://doi.org/10.1007/s00429-009-0203-y>

Tournier, J. D., Smith, R., Raffelt, D., Tabbara, R., Dhollander, T., Pietsch, M., Christiaens, D., Jeurissen, B., Yeh, C. H., & Connelly, A. (2019). MRtrix3: A fast, flexible and open software framework for medical image processing and visualisation. *NeuroImage*, *202*(January), 116137. <https://doi.org/10.1016/j.neuroimage.2019.116137>

- Wheeler-Kingshott, C. A. M., & Cercignani, M. (2009). About “axial” and “radial” diffusivities. *Magnetic Resonance in Medicine*, *61*(5), 1255–1260. <https://doi.org/10.1002/mrm.21965>
- Winston, G. P. (2015). The potential role of novel diffusion imaging techniques in the understanding and treatment of epilepsy. *Quantitative Imaging in Medicine and Surgery*, *5*(2), 279–27987. <https://doi.org/10.3978/j.issn.2223-4292.2015.02.03>
- Winston, G. P., Micallef, C., Symms, M. R., Alexander, D. C., Duncan, J. S., & Zhang, H. (2014). Advanced diffusion imaging sequences could aid assessing patients with focal cortical dysplasia and epilepsy. *Epilepsy Res*, *108*, 336–339. <https://doi.org/10.1016/j.epilepsyres.2013.11.004>
- Winston, G. P., Vos, S. B., Caldairou, B., Hong, S. J., Czech, M., Wood, T. C., Wastling, S. J., Barker, G. J., Bernhardt, B. C., Bernasconi, N., Duncan, J. S., & Bernasconi, A. (2020). Microstructural imaging in temporal lobe epilepsy: Diffusion imaging changes relate to reduced neurite density. *NeuroImage: Clinical*, *26*(September 2019), 102231. <https://doi.org/10.1016/j.nicl.2020.102231>
- Xiong, Y., Zhang, S., Shi, J., Fan, Y., Zhang, Q., & Zhu, W. (2019). Application of neurite orientation dispersion and density imaging to characterize brain microstructural abnormalities in type-2 diabetics with mild cognitive impairment. *Journal of Magnetic Resonance Imaging*, *50*(3), 889–898. <https://doi.org/10.1002/jmri.26687>
- Xu, S.-W., Xi, J.-H., Lin, C., Wang, X.-Y., Fu, L.-Y., Kralik, S. F., & Chen, Z.-Q. (2018). Cognitive decline and white matter changes in mesial temporal lobe epilepsy. *Medicine*, *97*(33), e11803. <https://doi.org/10.1097/MD.00000000000011803>
- Ye, Y., Xiong, J., Hu, J., Kong, M., Cheng, L., Chen, H., Li, T., & Jiang, L. (2013). Altered hippocampal myelinated fiber integrity in a lithium-pilocarpine model of temporal lobe epilepsy: A histopathological and stereological investigation. *Brain Research*, *1522*, 76–87. <https://doi.org/10.1016/j.brainres.2013.05.026>
- Yıldırım Capraz, I., Kurt, G., Akdemir, Ö., Hirfanoglu, T., Oner, Y., Sengezer, T., Atay Kapucu, L. O., Serdaroglu, A., & Bilir, E. (2015). Surgical outcome in patients with MRI-negative, PET-

---

positive temporal lobe epilepsy. *Seizure*, 29, 63–68.

<https://doi.org/10.1016/J.SEIZURE.2015.03.015>

You, Y., Bai, H., Wang, C., Chen, L. W., Liu, B., Zhang, H., & Gao, G. D. (2011). Myelin damage of hippocampus and cerebral cortex in rat pentylenetetrazol model. *Brain Research*, 1381, 208–216. <https://doi.org/10.1016/j.brainres.2011.01.011>

Zhang, H., Schneider, T., Wheeler-Kingshott, C. A., & Alexander, D. C. (2012). NODDI: Practical in vivo neurite orientation dispersion and density imaging of the human brain. *NeuroImage*, 61(4), 1000–1016. <https://doi.org/10.1016/j.neuroimage.2012.03.072>

Zhang, J., Gregory, S., Scahill, R. I., Durr, A., Thomas, D. L., Lehericy, S., Rees, G., Tabrizi, S. J., & Zhang, H. (2018). *In Vivo Characterization of White Matter Pathology in Premanifest Huntington ' s Disease*. 497–504. <https://doi.org/10.1002/ana.25309>

Alexander, A. L., Lee, J. E., Lazar, M., & Field, A. S. (2007). *Diffusion Tensor Imaging of the Brain*. 4(July), 316–329.

Beez, T., Munoz-Bendix, C., Steiger, H. J., & Hänggi, D. (2021). Functional tracts of the cerebellum—essentials for the neurosurgeon. *Neurosurgical Review*, 44(1), 273–278. <https://doi.org/10.1007/s10143-020-01242-1>

Ferrari, C., Cattaneo, Z., Oldrati, V., Casiraghi, L., Castelli, F., D'Angelo, E., & Vecchi, T. (2018). TMS over the Cerebellum Interferes with Short-term Memory of Visual Sequences. *Scientific Reports*, 8(1), 1–8. <https://doi.org/10.1038/s41598-018-25151-y>

Gatti, D., Van Vugt, F., & Vecchi, T. (2020). A causal role for the cerebellum in semantic integration: a transcranial magnetic stimulation study. *Scientific Reports*, 10(1), 1–12. <https://doi.org/10.1038/s41598-020-75287-z>

Gatti, D., Vecchi, T., & Mazzone, G. (2021). Cerebellum and semantic memory: A TMS study using the DRM paradigm. *Cortex*, 135, 78–91. <https://doi.org/10.1016/j.cortex.2020.11.017>

Jensen, J. H., Helpert, J. A., Ramani, A., Lu, H., & Kaczynski, K. (2005). Diffusional kurtosis imaging: The quantification of non-Gaussian water diffusion by means of magnetic resonance

imaging. *Magnetic Resonance in Medicine*, 53(6), 1432–1440.  
<https://doi.org/10.1002/mrm.20508>

Monaco, J., Casellato, C., Koch, G., & D’Angelo, E. (2014). Cerebellar theta burst stimulation dissociates memory components in eyeblink classical conditioning. *European Journal of Neuroscience*, 40(9), 3363–3370. <https://doi.org/10.1111/ejn.12700>

Santyr, B. G., Lau, J. C., Mirsattari, S. M., Burneo, J. G., de Ribaupierre, S., Steven, D. A., Parrent, A. G., MacDougall, K., & Khan, A. R. (2018). Novel Connectivity Map Normalization Procedure for Improved Quantitative Investigation of Structural Thalamic Connectivity in Temporal Lobe Epilepsy Patients. *Journal of Magnetic Resonance Imaging*.  
<https://doi.org/10.1002/jmri.26013>

Zeidler, Z., Hoffmann, K., & Krook-Magnuson, E. (2020). HippoBellum: Acute cerebellar modulation alters hippocampal dynamics and function. *Journal of Neuroscience*, 40(36), 6910–6926. <https://doi.org/10.1523/JNEUROSCI.0763-20.2020>

Krook-Magnuson, G. G. Szabo, C. Armstrong, M. Oijala, and I. Soltesz, “Cerebellar directed optogenetic intervention inhibits spontaneous hippocampal seizures in a mouse model of temporal lobe epilepsy,” *eNeuro*, vol. 1, no. 1, 2014, doi: 10.1523/ENEURO.0005-14.2014.

L. Kros, O. H. J. Eelkman Rooda, C. I. De Zeeuw, and F. E. Hoebeek, “Controlling Cerebellar Output to Treat Refractory Epilepsy,” *Trends Neurosci.*, vol.38, no. 12, pp. 787–799, 2015, doi: 10.1016/j.tins.2015.10.002.

M. L. Streng and E. Krook-Magnuson, “The cerebellum and epilepsy,” *Epilepsy Behav.*, vol. ArtInPress, p. 14, 2020, doi: 10.1016/j.yebeh.2020.106909.

G. Salvato et al., “Declarative long-term memory and the mesial temporal lobe: Insights from a 5-year postsurgery follow-up study on refractory temporal lobe epilepsy,” *Epilepsy Behav.*, vol. 64, pp. 102–109, 2016, doi: 10.1016/j.yebeh.2016.08.029.

R. E. Smith, J. Tournier, F. Calamante, and A. Connelly, “Anatomically-constrained tractography: Improved diffusion MRI streamlines tractography through effective use of

---

anatomical information,” *Neuroimage*, vol. 62, no. 3, pp. 1924–1938, 2012, doi: 10.1016/j.neuroimage.2012.06.005.

A. L. Alexander, J. E. Lee, M. Lazar, and A. S. Field, “Diffusion Tensor Imaging of the Brain,” vol. 4, no. July, pp. 316–329, 2007.

J. H. Jensen, J. A. Helpert, A. Ramani, H. Lu, and K. Kaczynski, “Diffusional kurtosis imaging: The quantification of non-Gaussian water diffusion by means of magnetic resonance imaging,” *Magn. Reson. Med.*, vol. 53, no. 6, pp. 1432–1440, 2005, doi: 10.1002/mrm.20508.

H. Zhang, T. Schneider, C. A. Wheeler-Kingshott, and D. C. Alexander, “NODDI: Practical in vivo neurite orientation dispersion and density imaging of the human brain,” *Neuroimage*, vol. 61, no. 4, pp. 1000–1016, 2012, doi: 10.1016/j.neuroimage.2012.03.072.

B. Jeurissen, J. Tournier, T. Dhollander, A. Connelly, and J. Sijbers, “NeuroImage Multi-tissue constrained spherical deconvolution for improved analysis of multi-shell diffusion MRI data,” *Neuroimage*, vol. 103, pp. 411–426, 2014, doi: 10.1016/j.neuroimage.2014.07.061.

J.-D. Tournier, F. Calamante, and A. Connelly, “Improved probabilistic streamlines tractography by 2nd order integration over fibre orientation distributions,” *Proc Int Soc Magn Reson Med* 18, 2010. <https://www.semanticscholar.org/paper/Improved-probabilistic-streamlines-tractography-by-Tournier-Calamante>

F. Palesi et al., “Contralateral cerebello-thalamo-cortical pathways with prominent involvement of associative areas in humans in vivo,” *Brain Struct. Funct.*, vol. 220, no. 6, pp. 3369–3384, 2015, doi: 10.1007/s00429-014-0861-2.

F. Palesi et al., “Contralateral cortico-ponto-cerebellar pathways reconstruction in humans in vivo: Implications for reciprocal cerebro-cerebellar structural connectivity in motor and non-motor areas,” *Sci. Rep.*, vol. 7, no. 1, pp. 1–13, 2017, doi: 10.1038/s41598-017-13079-8.

K. G. Schilling, F. Rheault, L. Petit, C. B. Hansen, V. Nath, and F. Yeh, “Tractography dissection variability : what happens when 42 groups dissect 14 white matter bundles on the same dataset ?,” 2020.

# **Ringraziamenti**